Title
New Materials and Methods towards High-Energy Lithium Metal Batteries

Author
FANG, CHENGCHENG

Publication Date
2019

UNIVERSITY OF CALIFORNIA SAN DIEGO

New Materials and Methods towards High-Energy Lithium Metal Batteries

A dissertation submitted in partial satisfaction of the
requirements for the degree Doctor of Philosophy

in

Materials Science and Engineering

by

Chengcheng Fang

Committee in Charge:

Professor Ying Shirley Meng, Chair
Professor Zheng Chen
Professor David Fenning
Professor Ping Liu
Professor Oleg Shpyrko

2019

The Dissertation of Chengcheng Fang is approved, and it is acceptable in quality and form for publication on microfilm and electronically:

Chair

University of California San Diego

2019

DEDICATION

To my mom *Xiaoping Chen* and my dad *Qi Fang*.

EPIGRAPH

“We are all in the gutter, but some of us are looking at the stars.”

\- *Oscar Wilde*

TABLE OF CONTENTS

LIST OF FIGURES

LIST OF TABLES

ACKNOWLEDGEMENTS

First and foremost, I would like to thank my PhD advisor, Prof. Ying Shirley Meng. During the past four years, she devoted so much energy to guide me, and offered freedom, trust, support, and many wonderful opportunities towards the success of my study and career. She mentored me how to develop my technical skills, professionalism, confidence, as well as leadership. I believe these characters will benefit my life forever. Her passion towards excellence will always be a great inspiration for me.

I would like to give my special thanks to my committee numbers Prof. Zheng Chen, Prof. David Fenning, Prof. Ping Liu and Prof. Oleg Shpyrko for their efforts and guidance through the journey.

I would like to acknowledge my colleagues and co-authors in UCSD, Dr. Jinxing Li, Dr. Minghao Zhang, Dr. Haodong Liu, Mr. Thomas Wynn, Dr. Shen Wang, Prof. Ivan Schuller, Dr. Judith Alvarado, Dr. Jungwoo Z. Lee, Dr. Byoung-Sun Lee, Dr. Xuefeng Wang, Ms. Yihui Zhang, Mr. Bingyu Lu, Mr. Yangyuchen Yang, Mr. Min-Han Lee and Mr. Miguel Ceja, for all the collocative work and support. I am also grateful to all my lab mates in LESC who had helped and inspired me in many ways.

I would like to express my sincere thanks to all external collaborators. I would like to thank Prof. Jing Gu and Dr. Fan Yang from San Diego State University, Dr. Kang Xu and Dr. Marshall A. Schroeder from Army Research Lab, Dr. Mei Cai and Dr. Li Yang from General Motors, Dr. Jie Xiao from Pacific Northwestern National Laboratory for their generous support.

I would like to acknowledge the financial support from Office of Vehicle Technologies of the U.S. Department of Energy through the Advanced Battery Materials Research (BMR) Program (Battery500 Consortium) under Contract DE-EE0007764.

Last but not least, I would like to thank my parents and younger brother, for their everlasting love, patience and support. Their understanding is the best gift in my life.

Chapter 1, in part, is a reprint of the material "Key Issues Hindering a Practical Lithium Metal Battery" as it appears in the Trends in Chemistry, **Chengcheng Fang**, Xuefeng Wang, Ying Shirley Meng, 2019, 1, 152-158. The dissertation author was the primary investigator and author of this paper. The author wrote the paper.

Chapter 2, in full, is a reprint of the material "Mitigating oxygen release in anionic-redox-active cathode materials by cationic substitution through rational design" as it appears in the Journal of Materials Chemistry A, Thomas A. Wynn, **Chengcheng Fang**, Minghao Zhang, Haodong Liu, Daniel M. Davies, Xuefeng Wang, Derek Lau, Jungwoo Z. Lee, Bo-Yuan Huang, Kuan-Zong Fung, Chung-Ta Ni and Ying Shirley Meng, 2018, 6, 24651- 24659. The dissertation author was the co-primary investigator and author of this paper. All experiment parts and corresponding writing were performed by the author.

Chapter 3 and Chapter 4, in full, is a reprint of the material "Quantifying inactive lithium in lithium metal batteries" as it appears in the Nature, **Chengcheng Fang**, Jinxing Li, Minghao Zhang, Yihui Zhang, Fan Yang, Jungwoo Z. Lee, Min-Han Lee, Judith Alvarado, Marshall A. Schroeder, Yangyuchen Yang, Bingyu Lu, Nicholas Williams, Miguel Ceja, Li Yang, Mei Cai, Jing Gu, Kang Xu, Xuefeng Wang and Ying Shirley Meng, 2019, 572, 511-515. The dissertation author was the co-primary investigator and author of this paper. The author conducted all the experiment and data analysis except for the TEM data collection, and cowrote the paper.

Chapter 5, in full, is a reprint of the material “Key Issues Hindering a Practical Lithium Metal Battery” as it appears in the Trends in Chemistry, **Chengcheng Fang**, Xuefeng Wang, Ying Shirley Meng, 2019, 1, 152-158. The dissertation author was the primary investigator and author of this paper. The author wrote the paper.

VITA

2012	Bachelor of Engineering in Materials Science and Engineering, Zhejiang University, Hangzhou, China
2015	Master of Philosophy in Innovative Technologies Leadership, Hong Kong University of Science and Technology, Hong Kong
2019	Doctor of Philosophy in Materials Science and Engineering, University of California San Diego, La Jolla, U.S.

PUBLICATIONS

1. **C. Fang***, J. Li*, M. Zhang, Y. Zhang, F. Yang, J. Z. Lee, M.H. Lee, J. Alvarado, M.A. Schroeder, Y. Yang, B. Lu, N. Williams, M. Ceja, L. Yang, M. Cai, J. Gu, K. Xu, X. Wang and Y. S. Meng, “Quantifying inactive lithium in lithium metal batteries”, ***Nature***, 2019, 572, 511-515

2. **C. Fang,** X. Wang, Y.S. Meng, “Key Issues Hindering a Practical Lithium Metal Battery”, ***Trends in Chemistry***, 2019, 1, 152-158

3. T.A. Wynn*, **C. Fang***, M. Zhang, H. Liu, D.M. Davies, X. Wang, D. Lau, J.Z. Lee, K.Z. Fung and Y.S. Meng, “Mitigating oxygen release in anionic-redox-active cathode materials by cationic substitution through rational design”, ***Journal of Materials Chemistry A***, 2018, 6, 24651

4. S. M. Wood, **C. Fang**, E. J. Dufek, S. C. Nagpure, S. V. Sazhin, B. Liaw, Y. S. Meng, “Predicting calendar aging in lithium metal secondary batteries: the impacts of solid electrolyte interphase composition and stability”, ***Advanced Energy Materials***, 2018, 8, 1801427

5. L. Yin, G. Mattei, Z. Li, J. Zheng, W. Zhao, F. Omenya, **C. Fang**, W. Li, J. Li, Q. Xie, J. Zhang, M. S. Whittingham, Y. S. Meng, A. Manthiram, and P.G. Khalifah, “Extending the limits of powder diffraction data: diffraction parameter space, occupancy defects, and atomic form factors”, 2018, ***Review of Scientific Instruments***, 89 (9), 093002

6. Y. Shi, M. Zhang, **C. Fang** and Y.S. Meng, “Urea-based hydrothermal synthesis of $LiNi_{0.5}Co_{0.2}Mn_{0.3}O_2$ cathode material for Li-ion battery”, ***Journal of Power Sources***, 2018, 394, 114-121
7. M. Zhang, H. Liu, Z. Liu, **C. Fang** and Y.S. Meng, “Modified co-precipitation synthesis of meso-structure controlled Li-rich layered oxides for minimizing voltage degradation”, ***ACS Applied Energy Materials***, 2018, 1, 3369
8. A. Singer, S. Hy, M. Zhang, D. Cela**, C. Fang**, B. Qiu, Y. Xia, Z. Liu, A. Ulvestad, N. Hua, J. Wingert, H. Liu, M. Sprung, A.V. Zozulya, E. Maxey, R. Harder, Y.S. Meng, O.G. Shpyrko, “Nucleation of dislocations and their dynamics in layered oxides cathode materials during battery charging”, ***Nature Energy***, 2018, 3, 641-674
9. M.D. Radin, S. Hy, M. Sina, **C. Fang**, H. Liu, J. Vinckeviciute, M. Zhang, M. S. Whittingham, Y. S. Meng, A. Van der Ven, “Narrowing the gap between theoretical and practical capacities in Li-ion layered oxide cathode materials”, ***Advanced Energy Materials***, 2017, 7, 1602888
10. H. Liu, J. Huang, D. Qian, S. Hy, **C. Fang**, J. Luo and Y.S. Meng, “Enhancing the electrochemical performance of Lithium-excess layered oxide $Li_{1.13}Ni_{0.3}Mn_{0.57}O_2$ *via* a facile nanoscale surface modification“, ***Journal of The Electrochemical Society***, 2016, 163 (6), A971

ABSTRACT OF THE DISSERTATION

New Materials and Methods towards High-Energy Lithium Metal Batteries

by

Chengcheng Fang

Doctor of Philosophy in Materials Science and Engineering

University of California San Diego, 2019

Professor Ying Shirley Meng, Chair

The sluggish progress of battery technologies has drastically hindered the rapid development of electric vehicles and next-generation portable electronics. Improving the energy density requires breakthroughs in materials for both cathode and anode, and new characterization methods to accurately correlate the materials with their performances.

For cathodes, lithium (Li) rich layered oxides exhibit high reversible specific capacities over 300 mAh g^{-1}, attributing to the oxygen redox reaction. However, oxygen activity comes with instability in the form of oxygen loss, which is associated with irreversible voltage decay and capacity fading. Calculations suggest that incorporating 4d elements, such as Mo, enhances the structural stability by altering the local band structure and impeding oxygen vacancy formation. Driven by these findings, Mo is co-doped with Co into $Li[Li_{0.2}Ni_{0.2}Mn_{0.6}]O_2$, showing notably reduced voltage decay and capacity fading without sacrificing energy density and cycle life.

The Li metal anode is critical to break the energy-density bottleneck of current Li-ion chemistry. Inactive Li formation is the immediate cause of capacity loss and catastrophic failure of Li metal batteries. However, its composition has not yet been quantitatively studied due to the lack of effective diagnosis tools that can accurately differentiate Li^+ in solid electrolyte interphase (SEI) components and the electrically isolated unreacted metallic Li^0, which together comprise the inactive Li. By establishing a new analytical method, Titration Gas Chromatography (TGC), we accurately quantify the contribution from unreacted metallic Li^0 to the total amount of inactive Li. We identify the Li^0, rather than the (electro)chemically formed Li^+ in SEI, as the dominating cause for the inactive Li and capacity loss. Coupling the measurements of the unreacted metallic Li^0 global content to the observations of its local micro- and nano-structure by cryogenic electron microscopies, we also reveal the formation mechanism of inactive Li in different types of electrolytes, and determine the true underlying cause of low CE in Li metal deposition and stripping. We ultimately propose strategies for highly efficient Li deposition and stripping to enable Li metal anode for next generation high-energy batteries.

Chapter 1 Introduction: Next Generation High-Energy Lithium Metal Batteries

1.1 500 Wh/kg Lithium Metal Batteries

Rechargeable lithium ion batteries have markedly reshaped our lives – from electric vehicles to portable electronic and optoelectronic devices. Since the first introduction of rechargeable battery, lead-acid battery with an energy density of ~ 40 Wh/kg, in 1859, the rechargeable battery energy density only increases to ~ 300 Wh/kg by today's most cutting-edge lithium ion technologies (NCA-graphite battery) in the past 160 years. Comparing with the rapid development of semiconductor industry, which follows the Moore's law, batteries essentially have become the bottleneck of many electronic technologies that are required to be lighter, thinner and lasting longer. The ever-increasing demands on high energy urgently request the battery research and development to breakthrough current lithium ion chemistry and look for better alternatives. Winter *et al* [1] summarized the gravimetric energy densities of various battery chemistries, as shown in Figure 1.1. The current commercialized graphite anode materials almost reach its theoretical limits, but only deliver a cell level energy density of ~ 300 Wh/kg. Only lithium metal anodes could potentially give an energy density of more than 500 Wh/kg when coupling with high-Ni NMC layered oxides or sulfur as cathode materials.[2]

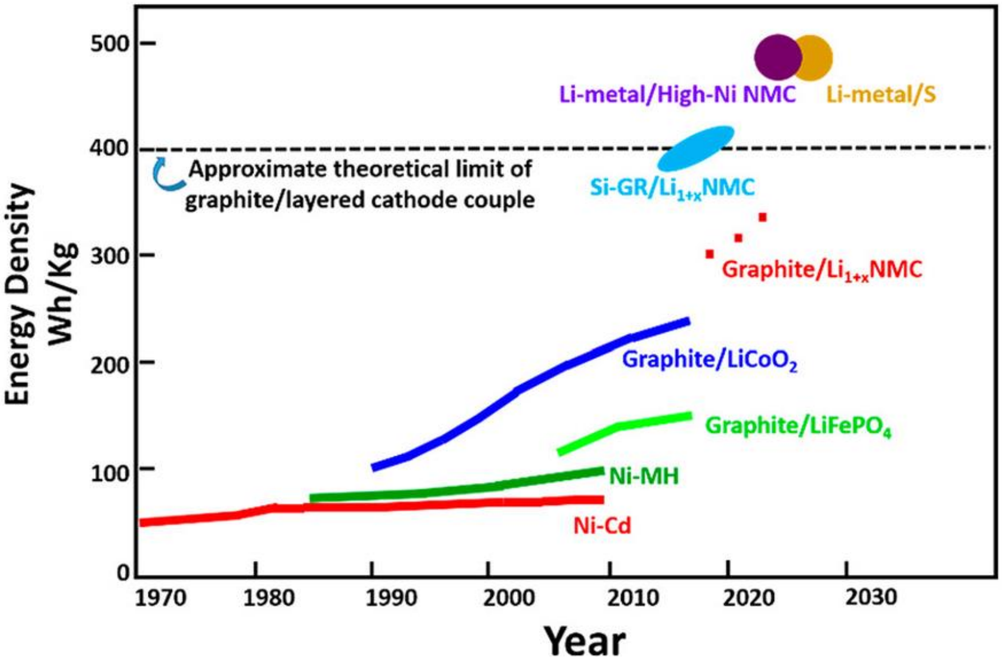

Figure 1.1 The development of gravimetric energy densities for various battery chemistries.[1]

Figure 1.2 shows the schematic illustration of the first commercial lithium ion battery, which employ $LiCoO_2$ as cathode, graphite as anode and liquid organic carbonate electrolyte. The other necessary lithium ion battery components include separators, current collectors (Cu for anode and Al for cathode), cell cases and so on. During charging/discharging, lithium ions shuttle between the cathode and anode through the electrolyte inside the battery, while electrons traverse the external circuit where they do work. The overall energy density of a battery is determined by two factors, the specific capacity provided by the active electrode materials and the total weight of all cell components. Based on the definition, Wh/kg, the higher the specific capacity and the lower the total weight of a cell, the higher energy density a cell can deliver. So the design principles for a high-energy battery include exploration of cathode and anode materials with intrinsic high specific capacity, and optimization of cell configurations to reduce the weight of inert components, even including the amount of electrolyte. Liu *et al* [3] shows a detailed example of how to design a commercially viable high energy cell by optimizing cell parameters (Figure 1.3). For the cathode, apart from the requirements on improving the specific capacity of cathode materials to 252 mAh g^{-1}, thick electrode design is critical. A balance among the active mass loading, porosity, and thickness should maximum the areal specific capacity, minimize the amount of electrolyte needed and maintain a homogeneous electronic/ionic conductivity within the whole electrode. For lithium metal anode, the requirement lies in the N/P ratio, which is directly correlated to the lithium metal battery cycle life.

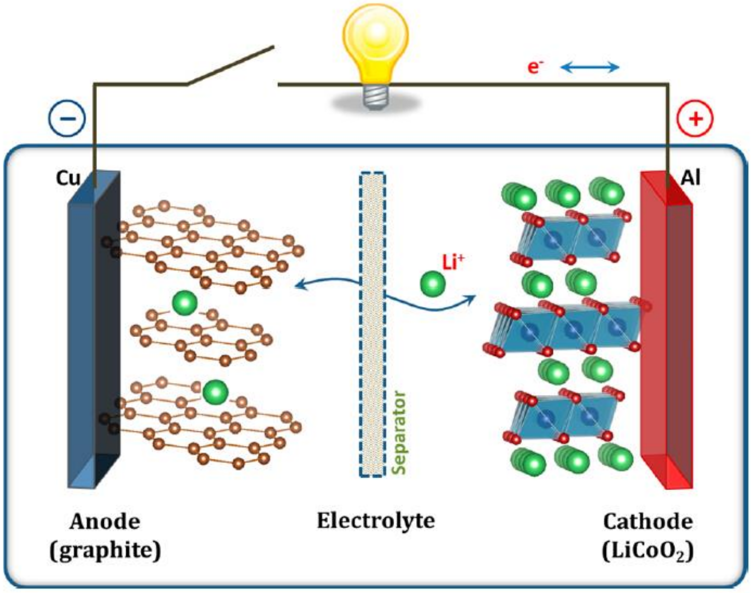

Figure 1.2 Schematic diagram of the first commercial lithium ion battery that employs graphite as anode and $LiCoO_2$ as cathode[4]

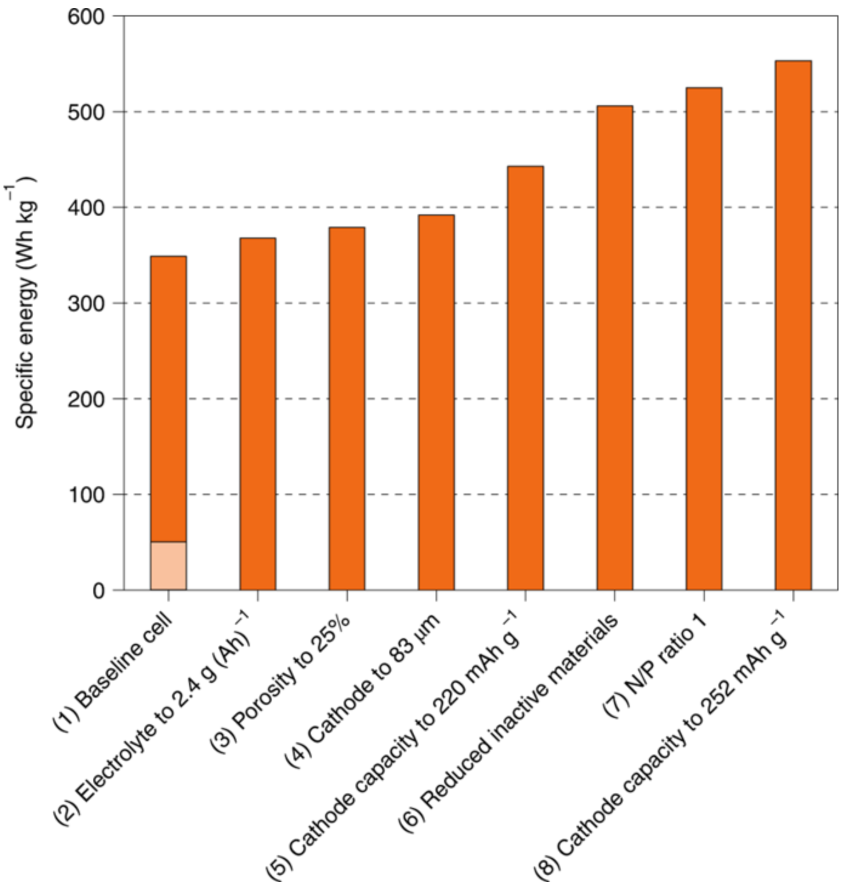

Figure 1.3 A calculation showing cell-level specific energy as a function of cell parameters. The baseline cell consists of NMC622 material with 196 mAh g^{-1} specific capacity (charge to 4.6 V), 35% of cathode porosity, 22.0 mg cm^{-2} of active mass loading and 70 µm of cathode thickness. The N/P ratio is 2.6. The electrolyte to capacity ratio is 3.0 g Ah^{-1}. The lightly shaded area in the baseline cell represents a specific energy much less than 50 Wh kg^{-1} based on the amount of the cathode, anode and electrolyte and other inactive materials reported in most literature studies for rechargeable coin cells.[3]

In many of published studies of battery materials, it is common to see the testing results are based on low areal capacity (< 1 mAh cm^{-2}), flooded electrolyte (100 µL in a coin cell), and infinite lithium source (> 500 µm lithium chips). Under these conditions, cells usually show very good cycling performances (Figure 1.4a). However, this is not a proper reflection of the scenarios in real-world batteries. There is a huge gap between these conditions in research and in reality, as summarized in Figure 1.4b. It is essential to evaluate battery optimizations under realistic conditions so that the R&D advances can be rapidly deployed into commercial applications.[5]

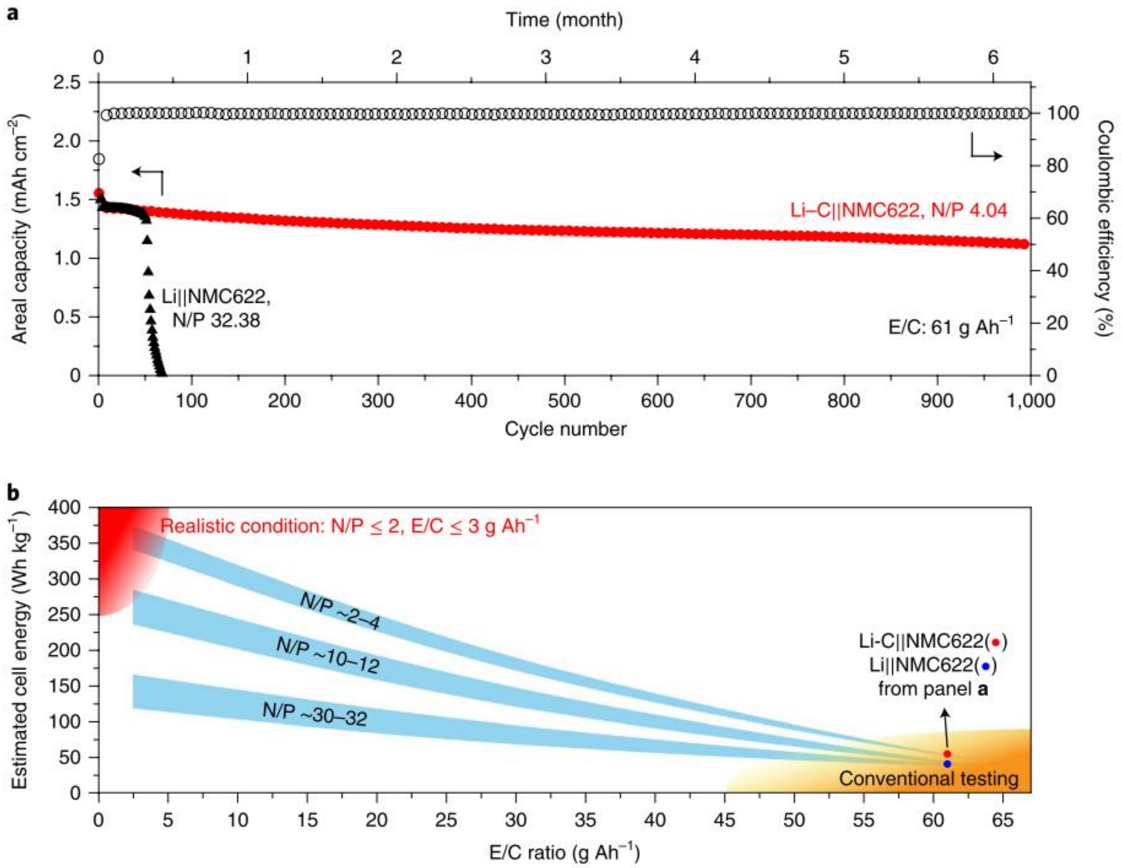

Figure 1.4 Estimated cell energy as a function of the N/P and E/C ratios, assuming that other cell parameters are same. The energy density was calculated at a single-cell level, and the mass includes the cathode, Al foil, electrolyte, separator and anode used in the cell, and an estimated package foil mass instead of the coin cell case. The low-area capacity cathode and thick Li metal anode gave a high N/P ratio, and the flooded electrolyte led to a high E/C ratio. Such high masses combined with a low-loading cathode reduce the specific energy of the battery. For example, for the Li||NMC622 cell in a, tested under conventional conditions, the N/P ratio was as high as 32.38, and the E/C ratio reached 61 g Ah^{-1} owing to the flooded electrolyte (100 μl); therefore, the presented energy density is only 46 Wh kg^{-1} , which is far below that expected from the high energy density of such a cell. To achieve a high cell-level energy under realistic conditions, the cell parameters must be constrained with the N/P ratio no more than 2 and the E/C ratio less than 3 g Ah^{-1} In addition, owing to the lightweight Li, the estimated energy densities of LMBs are relatively higher than those of Li ion batteries using a graphite anode.[5]

1.2 Layered Oxides Cathode Materials

In conventional lithium ion batteries, when graphite is adopted as the anode, as the capacity-determining component, cathode materials have been extensively studied to explore new compounds for longer cycle life and higher energy density. For commercially available $LiCoO_2$, only half of the lithium could be utilized in order to avoiding a major phase transition which leads to layer structure collapse, limiting the effective specific capacity of $LiCoO_2$ around 140 mAh g^{-1}. By partially substituting the Co with Ni and Mn/Al, forming $LiNi_xMn_yCo_{1-x-y}O_2$ (NMC)/ $LiNi_{0.85}Co_{0.1}Al_{0.05}O_2$ (NCA), the capacities could be significantly booted to ~ 200 mAh g^{-1}. Further exploring the lithium replacement in layered oxides, Li-rich layered oxides (LRLO), $xLi_2MnO_3·(1 − x)LiMO_2$ (M = Ni, Mn, and Co), was found by further introducing excess lithium to transition metal layers. Apart from the capacity contributed by transition metal redox, anion redox is enabled in this unique structure, leading to their high reversible discharge capacity over 300 mAh g^{-1}. The discharge voltage profiles and capacity comparison of different types of layered oxides are shown in Figure 1.5. The ultra-high specific capacity makes LRLO very attractive for next-generation high-energy batteries, however, its poor kinetics and large voltage decay upon cycling impede its implementation in practical batteries.

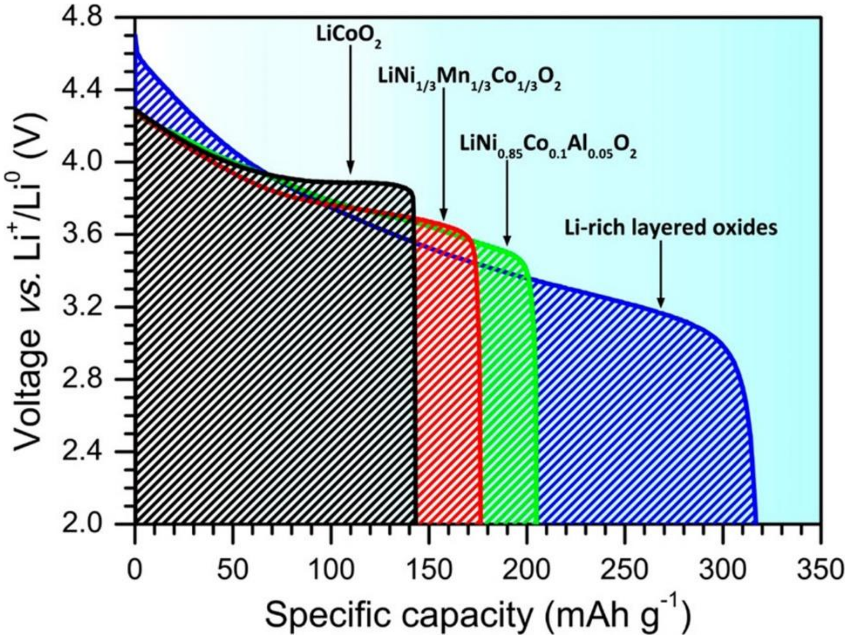

Figure 1.5 Discharge voltage profiles of different layered oxides cathode materials. [6]

1.3 Lithium Metal Anode

For a battery anode, lithium (Li) metal is considered the "Holy Grail" because of its extremely low density (0.534 g cm^{-3}), ultra-high theoretical capacity (3860 mAh g^{-1}), and exceptionally negative electrochemical potential (-3.04 V vs. standard hydrogen electrode) [7]. The Li metal anode was first adopted in the TiS_2-Li prototype in 1976 [8,9], but was soon replaced by intercalation compounds like graphite (C) because of severe capacity fading and potential explosion hazards resulting from dendritic Li growth [10]. Since C/$LiCoO_2$-based Li-ion batteries delivered an energy density of 120-150 Wh/kg, twice that of the state-of-the-art Ni-Cd batteries at the time [9], Li-ion batteries rapidly supplanted Ni-Cd in the battery market, becoming the prevalent technology. Since then, Li-ion chemistry research has thrived, with significant effort expended towards further increasing energy and power density. Meanwhile, the use of Li metal as the anode material has also gradually resuscitated after the 20 years of dormancy since its initial introduction. Around 2010, prospering electric vehicle and consumer electronic markets urgently demanded development of high-energy-density storage devices, triggering explosive research on Li metal batteries to achieve an energy density of 500 Wh/kg or higher in the form of high-Ni NMC-Li or S-Li batteries [1]. Figure 1.6 summarizes the number of the published papers with a keyword of "lithium metal battery" over the past ~40 years, clearly demonstrating the intense interest in Li metal batteries.

Current Li-metal-battery research is primarily focused on strategies to alleviate Li dendrite formation, improve the Coulombic efficiency (CE), and better understand plating/stripping through advanced characterization methods and theoretical modeling. These efforts have been systematically summarized in the recent reviews [11–16]. Among these achievements, it is important to highlight that dense Li deposition with a CE of approximately 99% is currently readily obtainable by employing electrolytes of high salt concentration [17–21] or localized high-concentration electrolytes [22,23]. Another key achievement of note is the use of cryogenic electron microscopy (Cryo-EM) to visualize the nanostructure of the electrochemically deposited Li metal (EDLi) and mysterious solid electrolyte interphase (SEI) [24–26], affording a powerful tool to correlate nanostructure with performance and optimization strategies. Regardless of these achievements, thorough understanding of Li metal failure still remains challenging, due to the difficulties in Li metal characterization.

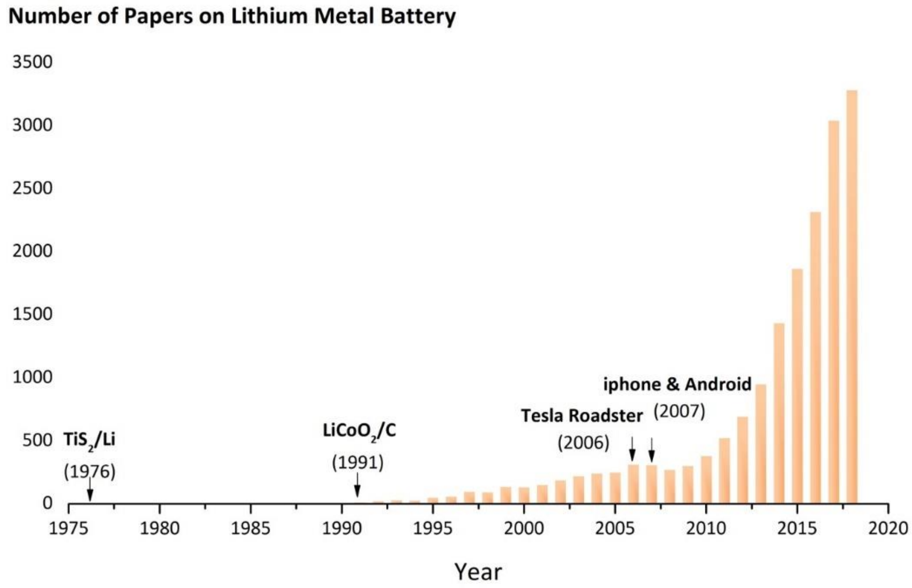

Figure 1.6 The number of papers on Li metal batteries published each year since the first introduction in 1976. A total number of 17376 of papers have been published. Statistics from Web of Science by searching key words Li Metal Battery, as of Dec. 1, 2018.

1.4 Recent advances in lithium metal characterization

1.4.1 Introduction

A variety of characterization tools have been developed to understand lithium metal growth and degradation mechanisms, which is of critical importance to achieve enhanced safety and battery performances. However, it has been challenging for lithium metal characterization, due to two reasons, 1. High reactivity of lithium metal, leading to difficulties in beam damage issues and sample protection; 2. Low atomic number of lithium, making many well developed characterization techniques based on X-ray and electrons fail on lithium metal. Despite the difficulties, efforts on lithium characterization are still being made to broad our understanding. These efforts will be discussed below from three perspectives, morphology, SEI chemical composition and quantitative analysis.

1.4.2 Morphology

Lithium dendrite growth is believed to be the biggest issue of lithium metal safety. A wide range of imaging tools from variety of length and time scales have been developed to understand the dendrite nucleation and growth. Figure 1.7 summarizes the imaging techniques that have been utilized to study lithium dendrite growth and their spatial resolution limits. Table 1.1 compares the pros and cons of these tools.

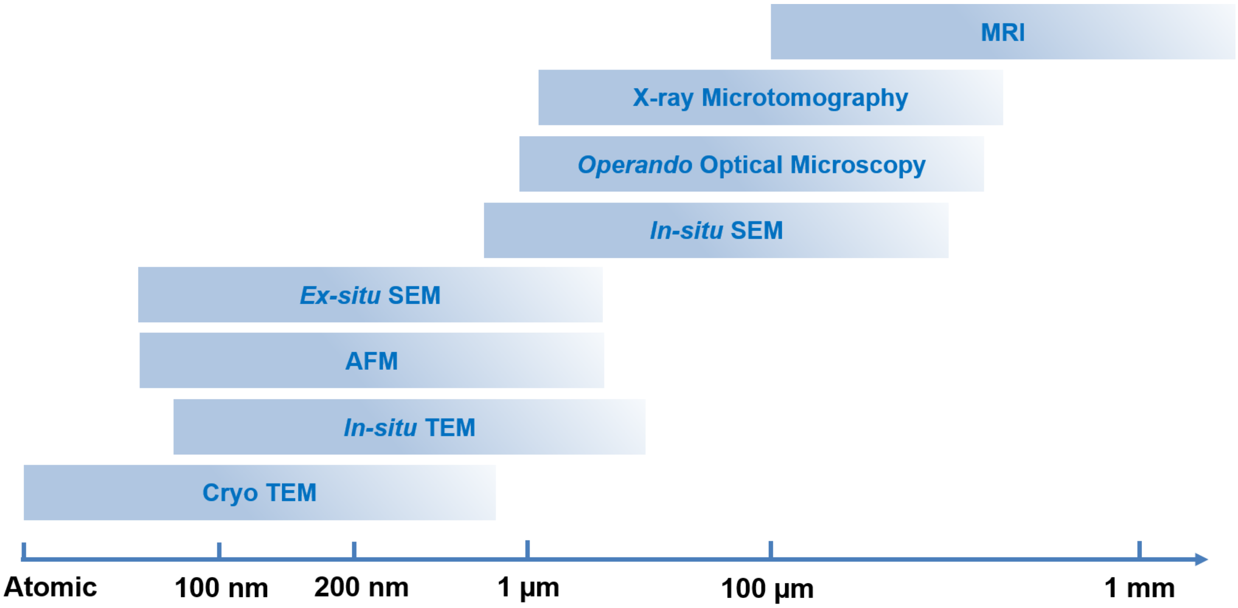

Figure 1.7 A summary of imaging tools used for lithium metal study and their detection ranges.

Table 1. 1 The pros and cons of a variety of imaging tools for lithium metal study

	Pros	Cons
Cryo TEM	• Atomic resolution • Chemical information • Reduced beam damage	Ex-situ
In-situ TEM	• In-situ • Chemical information	• Limited resolution • Beam damage
Ex-situ SEM	Relatively high resolution (< 100 nm)	• Ex-situ • Morphology only
In-situ SEM	In-situ observation	• Difficult cell design • Beam damage • Limited resolution (> 200 nm) • Morphology only
AFM	High resolution 3D imaging (30 nm)	Surface morphology only
Optical Microscopy	• Easy cell design • Operando observation	• Limited resolution (>200 nm) • Morphology only
X-ray Microtomography	• In-situ • Quantification (potentially)	Limited resolution (~ 1 µm)
MRI	• Time-resolved, in real pouch cell • Quantification of microstructure	Poor resolution (~ 100 µm)

Wood *et al*[12,27] developed operando video microscopy (Figure 1.8a) to observe the dynamic behavior of lithium dendrite during plating and stripping, and correlated the morphology change to the voltage profile response. As shown in Figure 1.8b, they identified three processes during stripping. First, the as-formed mossy dendrite dissolves into electrolyte. This is a kinetically fast reaction so that the cell polarization during this process is minimum. Dendrites exist on both electrodes. Second, “dead” lithium forms. The cell polarization becomes maximum in this step. There is a transition from electro-dissolution of dendrites to bulk lithium dissolution. Last, pitting occurs on bulk, which leads to decreased cell polarization. This step is a kinetically slow bulk dissolution of lithium. Chen and Wood *et al*[28] later also used the same set-up to investigate the voltage profile response to mass transport effect (Figure 1.8c). They observed two types of behavior from lithium plating curves, peaking and arcing. They found the peaking behavior is limited by reaction kinetics in initial cycles, while the arcing voltage is limited by mass transport within the accumulated dead lithium layers. Overall, the operando video microscopy offers a powerful platform to analyze lithium dendrites. But its spatial resolution is limited to micro level.

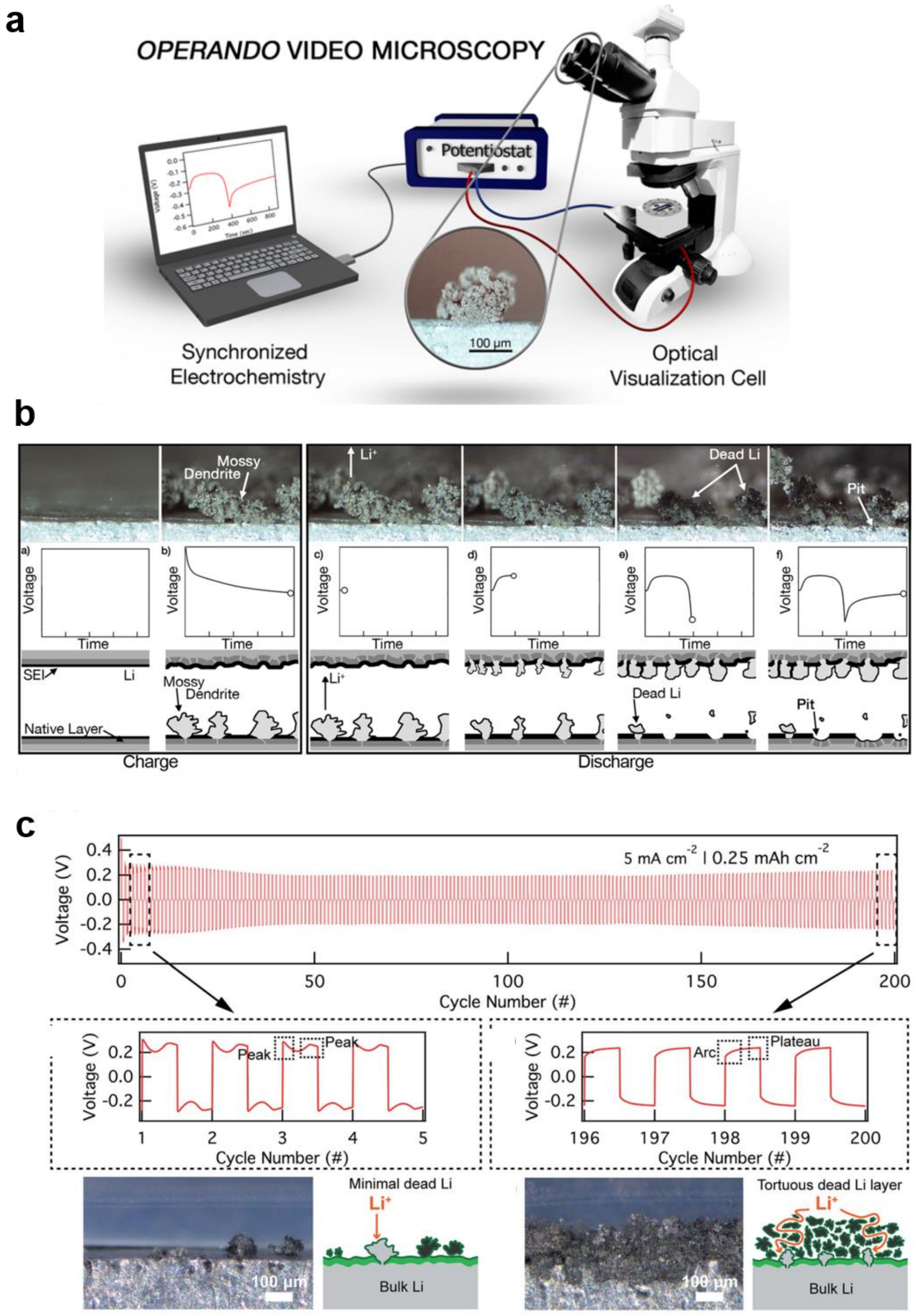

Figure 1.8 (a). schematic of synchronized electrochemical-video microscopy setup[27]; (b), video observation and schematic illustration showing the correlation between lithium morphology and electrochemical responses in lithium-lithium symmetric cell[12]; (c) the correlation between voltage profiles and mass transport effect[28].

Bai *et al*[29] also employed the operando optical microscopy to visualize lithium growth at micron level. They revealed the relationship among morphology, current, capacity and voltage responses in convention carbonate electrolyte. When the concentration of lithium ions at the electrode/electrolyte interface reaches zero, the moment is defined as "Sand's time"; The capacity at Sand's time is defined as "Sand's capacity". They found that dendritic lithium starts to grow beyond Sand's time and the dendritic growth leads to voltage spike, as shown in Figure 1.9. Before Sand's capacity, the lithium growth is limited by reaction and follows root-growing process. After Sand's capacity, the lithium growth turns to dendritic tip-growing, which is limited by transport. These findings indicate that increasing salt concentration in electrolyte could maximum Sand's capacity thus reducing the lithium dendrite formation.

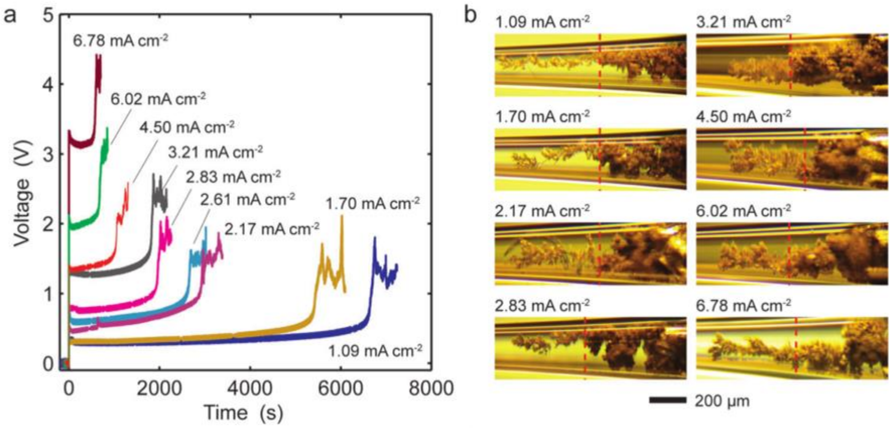

Figure 1.9 (a), voltage responses of capillary cells at various deposition current densities; (b), representative optical images of lithium deposits demonstrating the clear change of morphologies at Sand's time for various current densities.[29]

Scanning electron microscopy (SEM) is the most commonly used technique for ex situ morphology observation. It possesses higher resolution than optical microscope. However, it is challenging to design an *in situ* cell for SEM, where vacuum system is needed, thus limiting the actual achieved resolution. As a result, *in situ* SEM is not as widely adopted as operando optical microscopy. In spite of the challenges, Dolle *et al*[30] designed a polymer electrolyte based *in situ* cell (Figure 1.10a). The *in situ* SEM recorded every 20 minutes to reduce the beam damage on polymer electrolyte. They observed a root growth mechanism of lithium dendrite, as shown in Figure 1.10b.

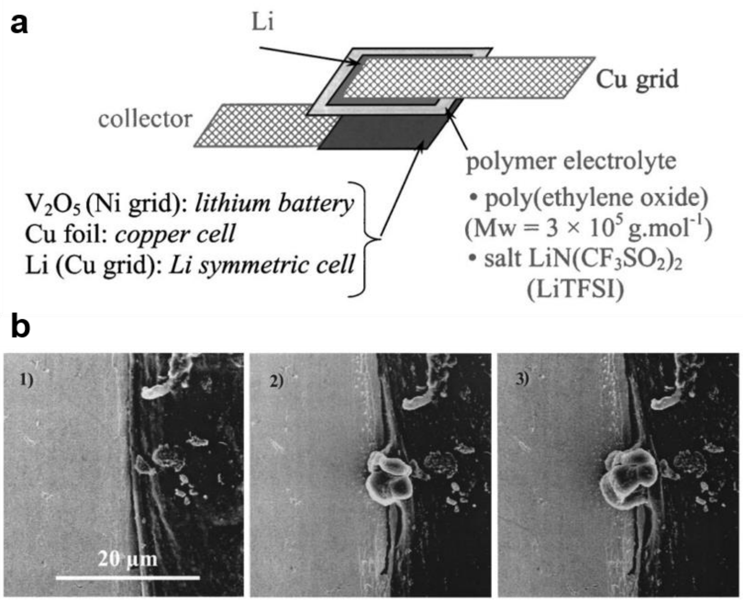

Figure 1.10 (a), configuration of the in situ SEM cell; (b) observation of lithium deposition at the Cu-polymer inferface at 0, 160 and 200 min, the current density is 0.5 mA cm^{-2}.[30]

Atomic force microscopy (AFM) enables 3D morphological image with a lateral resolution of ~ 30 nm and vertical resolution of 0.1 nm. Cohen *et al* [31] used AFM to observe a lithium surface film, where a bumper appears after lithium deposition (Figure 1.11a) and shrink after consecutive lithium dissolution (Figure 1.11b). Based on the observation, they proposed the failure mechanism of lithium is the beginning of dendrite formation and non-uniform lithium dissolution are accompanied by breakdown and reparation of surface films, as illustrated in Figure 1.11c.

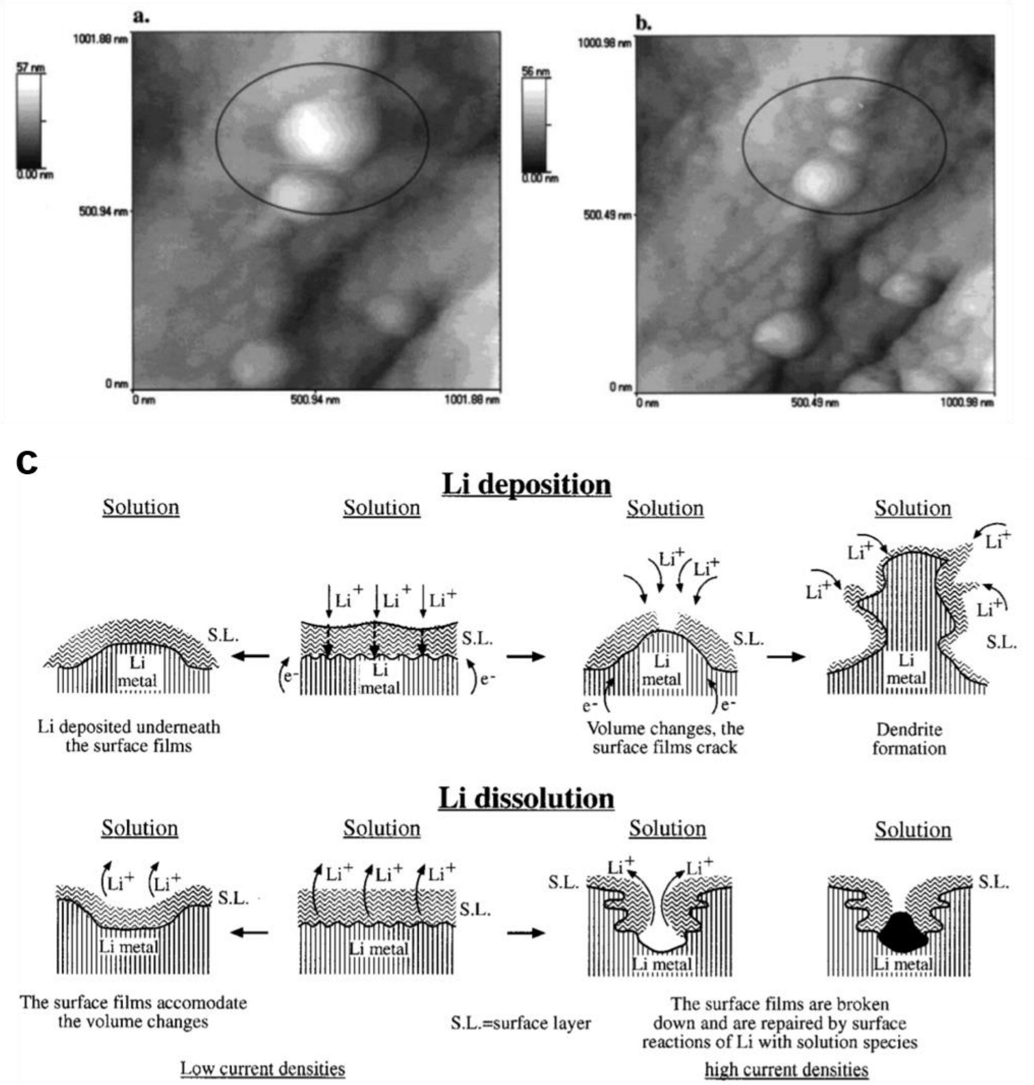

Figure 1.11 (a) AFM image showing lithium deposition; (b) AFM image showing lithium stripping; (c) schematic illustration of lithium metal failure mechanism based on AFM observation.[31]

Transmission electron microscopy is a powerful to study both morphology and chemical information of lithium at nanoscale. In 2011, Ghassemi *et al* [32] firstly adopted an open cell configuration using ionic liquid electrolyte to enable in situ observation of lithium fiber growth on Si nanorods. After this, liquid cell was employed for in situ study of dendrite growth and SEI information in conventional electrolytes[33–35]. Due to extreme sensitivity of lithium to electron beams, these in situ TEM studies at room temperature only enables a micron-scale resolution. In 2017, borrowing the wisdom from structural biology, cryogenic TEM [24] was firstly introduced to battery field and enabled the atomic resolution of lithium metal for the first time. The cells/holders used in TEM play the key role. Figure 1.12 shows three types of cells/holders that have been used in lithium metal study. Figure 1.12a is an open cell, which could enable an operando observation. However, this type of cell requires the electrolyte to be vacuum compatible and thus lack of the solid-liquid interphase study in real battery scenario. Liquid cell (environmental TEM), as shown in Figure 1.12b, allows solid-liquid interphase study using liquid electrolyte, making the observation close to real cell conditions. But the beam effect on dynamic processes is inevitable. The resolution is also limited by the presence of liquid. Cryo-holder allows the TEM operation under cryogenic temperature, which eliminate the beam damage on fragile lithium metal and SEI, thus enables an atomic resolution. But so far, the cryo-TEM can only operate ex situ. Despite of the limitations, TEM is still the most powerful tool to study the lithium nucleation and growth.

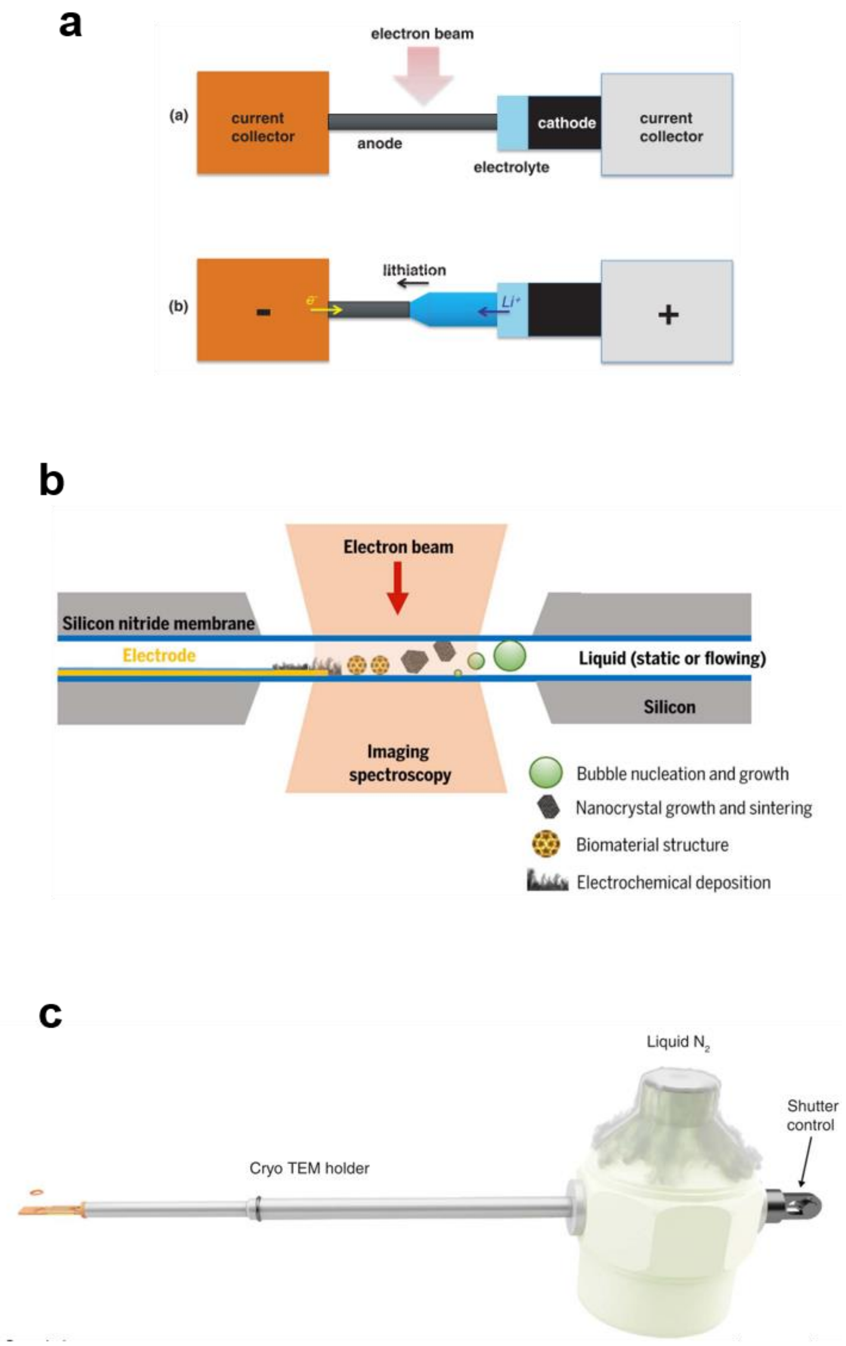

Figure 1.12 TEM cell/holders for lithium metal. (a) *in situ* open cell[36]. (b) *in situ* liquid cell[34]. (c) cryogenic holder[24].

Kushima *et al* [37] used a liquid cell design, as shown in Figure 1.13a, to in situ observe the lithium nucleation and growth in early stage. This cell design employed $LiCoO_2$ as the lithium source and 1M LiTFSI in di-methoxy sulfoxide as electrolyte, which is the one that is most close to real cell conditions in literature. Based on the real-time TEM video analysis as shown in Figure 1.13c, they identified the root growth mechanism. They also found that different overpotentials lead to surface growth or whisker growth, as illustrated in Figure 1.13b. Overall, they claimed 4 stages of growth: 1. Nucleation; 2. Whisker growth from root; 3. Growth rate decreases due to SEI accumulation; 4. A kink formed on the whisker, separating it into two segments.

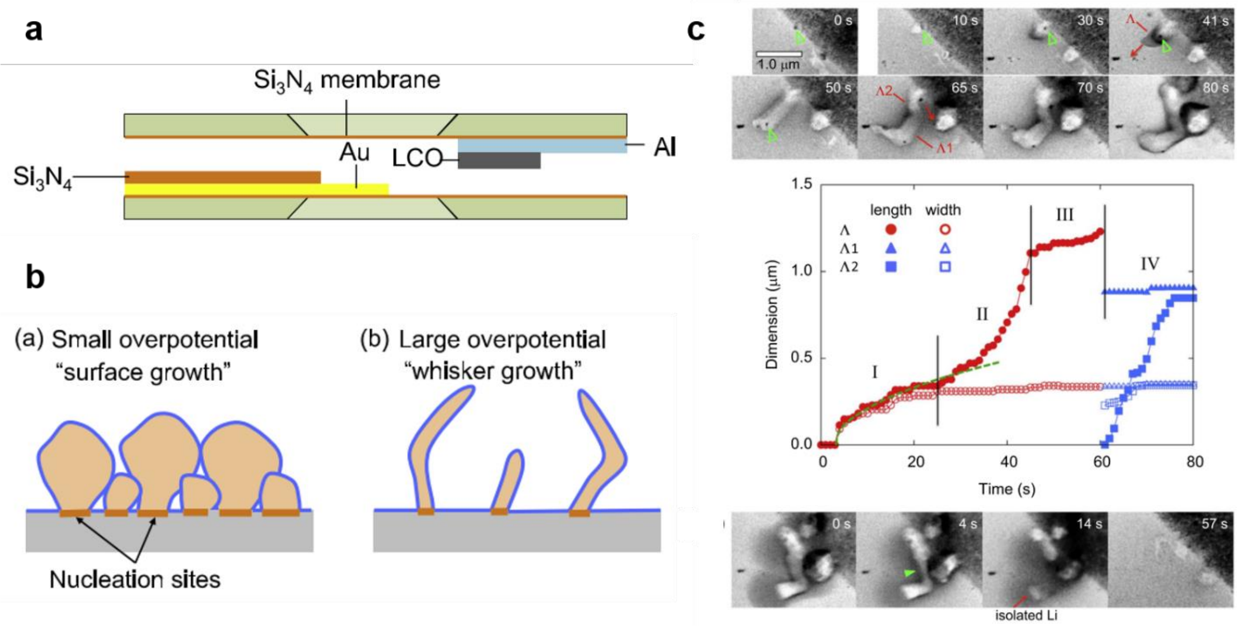

Figure 1.13 (a) schematic of cross-section of the liquid cell near the silicon nitride membrane windows; (b) schematic illustration explaining root growth mechanism of lithium whiskers; (c) real-time observation of lithium whisker growth and dissolution by *in situ* TEM.[37]

Synchrotron hard X-ray microtomography with an energy of 22 – 25 KeV is used to image the lithium dendrite formation. Imaging is achieved by voxel brightness contrast with a spatial resolution of microns. Harry *et al* [38] used a symmetric lithium-polymer-lithium cell to image the structure residing on either side. As shown in Figure 1.14, they found that dendrites initiate from subsurface structure underneath the polymer/ lithium interface. The volume occupied by the subsurface structure is significantly larger than that occupied by the dendritic structure protruding out from the electrode surface.

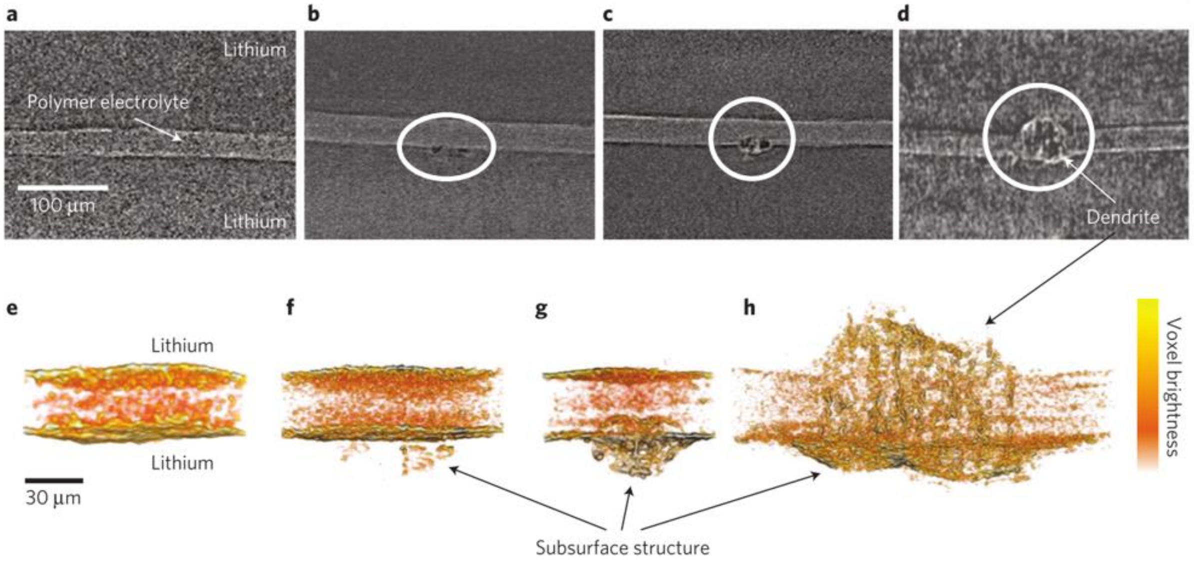

Figure 1.14 Evolution of lithium dendrite growth by X-ray tomography 3D reconstruction, in a symmetric lithium cell.[38]

Eastwood *et al* [39] used synchrotron phase contrast X-ray imaging (19 keV) to study the lithium deposition behavior. The cell design is shown in Figure 1.15a. the components are distinguished by contrast differences of lithium (lower x-ray attenuation), electrolyte (intermediate attenuation) and lithium salt (higher attenuation). Greater X-ray attenuation relates to an increased electron density due to the incorporation of higher atomic number elements in the structure. Figure 1.15b shows the 2D slice through reconstructed microstructure after plating. The dark parts represent mossy/bulk lithium, while the light grey indicates the electrolyte. Figure 1.15c shows the reconstructed morphology after stripping, indicating the “dead” lithium residue. Conceptively, this method potentially could be used to quantify the “dead” lithium by differences in X-ray attenuation; lithium metal has the least X-ray attenuation and SEI components exhibits increased X-ray attenuation. However, this is limited by the spatial resolution, which is submicron level, whereas the SEI thickness is less than 100 nm, and the influence from salts.

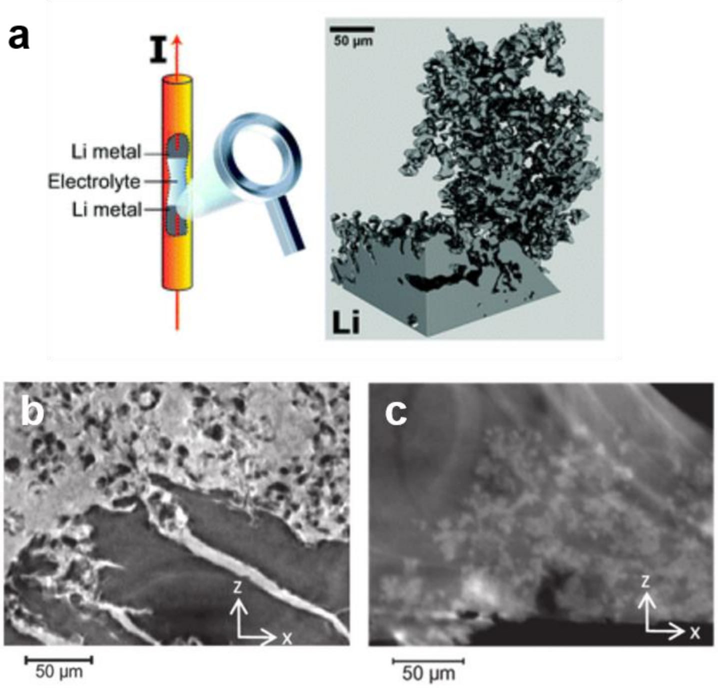

Figure 1.15 (a) schematic illustration of the cell setup for in situ tomographic X-ray imaging. (b) 2D slice through reconstructed microstructure after plating; (c) 2D slice through reconstructed microstructure after stripping, showing the presence of “dead” lithium.[39]

Magnetic resonance imaging (MRI) is also investigated as an in situ, non-invasive tool to study the dendrite growth. Even through the spatial resolution of MRI is poor (60 μm * 376 μm along x and y directions), this time-resolved technique can be used to diagnose dendrite growth real-time in a pouch cell, as exampled in Figure 1.16.[40]

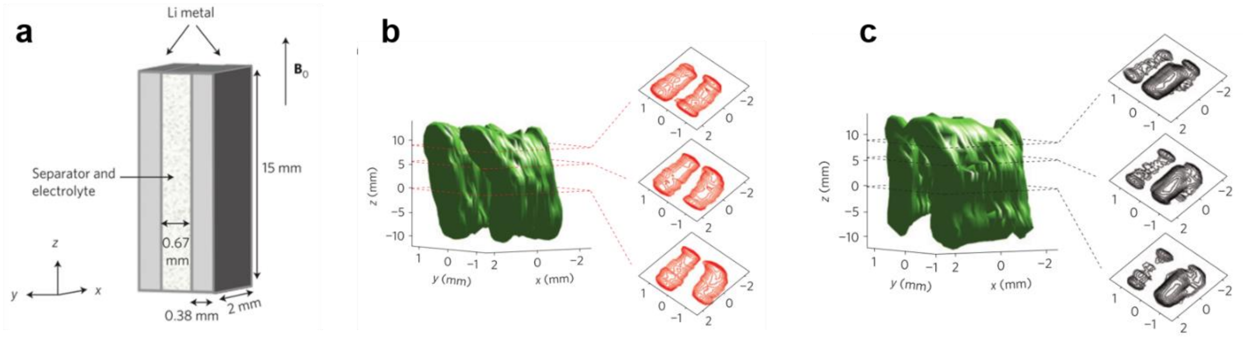

Figure 1.16 (a) schematic representation of the bag-cell battery, and its orientation with respect to the static magnetic field in the NMR spectrometer; 3D MRI images of (b) in pristine stage and (c) after charging.[40]

1.4.3 SEI chemical composition

Lithium instantaneously reacts with a solvent to form an electrically insulating and ionically conductive interface (solid electrolyte interphase, SEI), which physically prevents the direct contact between Li and the solvent, making Li dynamically stable in some organic solvents. The passivation by SEI makes it possible to operate a lithium metal cell under a reductive environment and extend the operation voltage window to 4 V and above. SEI layer is related to the electrolyte composition (including salts, solvents, and additives) and strongly affects the lithium morphology and cycling performance of a lithium metal battery. It is the most important yet mysterious component of lithium metal anode.[41,42]

X-ray photoelectron spectroscopy (XPS) is one of the most popular and effective tools to study the global SEI chemical compositions.[22,23,43] It has high surface sensitivity with a detecting depth of 10 nm. XPS depth profiling allows to detect the chemical information of subsurface. Qualitative and quantitative composition analysis can be achieved by well controlled experiment. Since XPS is highly surface sensitive, differentiating the surface salt residue and the actual SEI layer is critical. Properly rinsing the sample is necessary. Figure 1.17 is an example showing influence of rinsing process: surface salt residue can be removed by complete solvent rinsing (SEI formed in 4M LiFSI + 2M LiTFSI in DME).

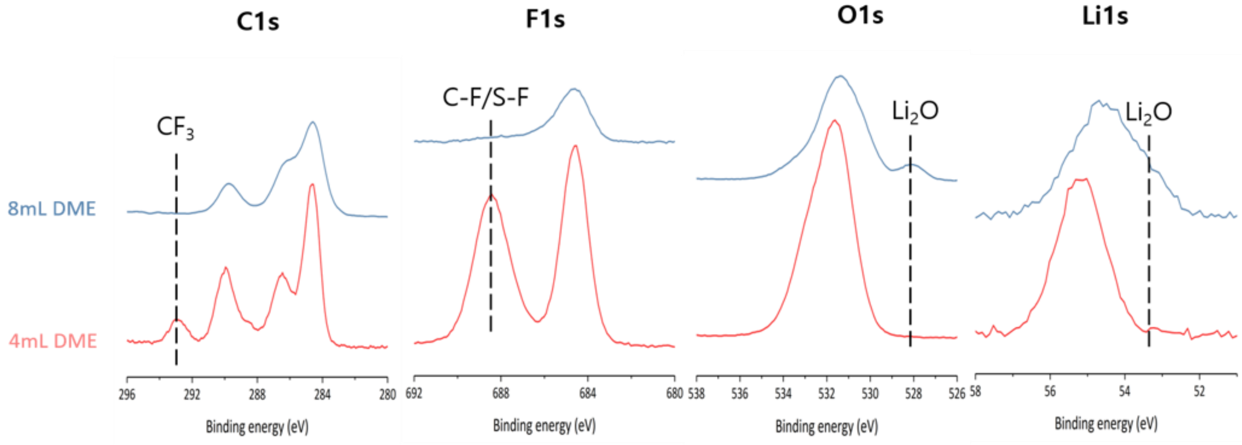

Figure 1.17 The influence of rinsing process on XPS results.

It has long believed that the SEI has a Mosaic structure, namely Li_2CO_3, Li_2O, LiF, polyolefins and semicarbonates are mixed forming a surface layer. [44] Recently the Mosaic type of SEI was directly imaged by Li *et al* [24] using cryo-TEM, as shown in Figure 1.18a and b, exhibiting that crystalline Li_2CO_3 and Li_2O embedding in an amorphous matrix. They also observed another multilayer model, where Li_2O lies outside layer (Figure 1.18c and d) using an FEC electrolyte. The correlation of SEI nanostructure and the battery performance needs further investigation.

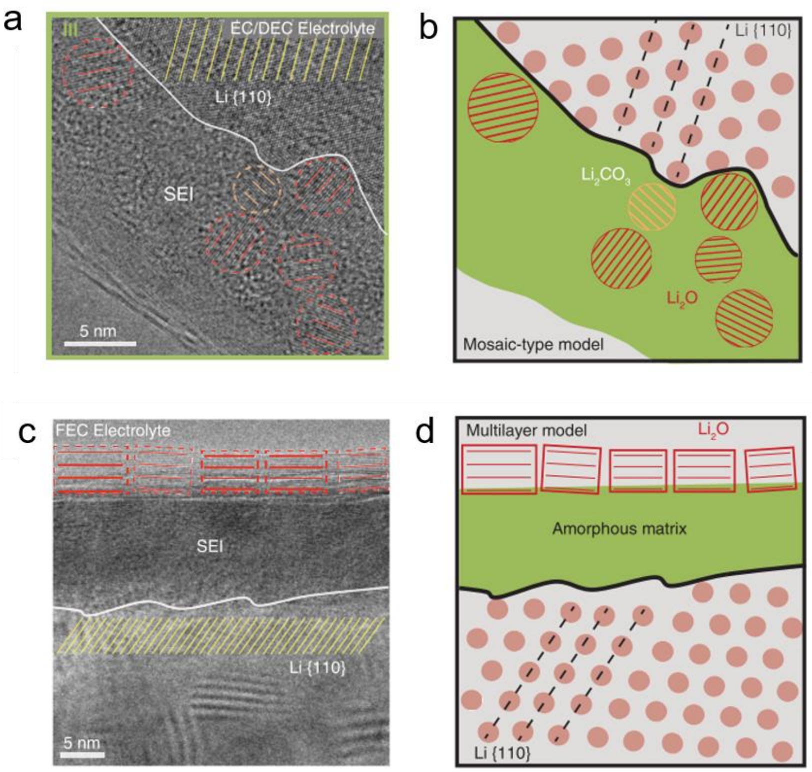

Figure 1.18 (a) and (b) Mosaic type of SEI; (c) and (d) Multilayer type of SEI observed by cryo-TEM.[24]

1.4.4 Quantitative analysis

Quantitatively studying the deposited lithium and inactive lithium have been challenging for decades. Nuclear magnetic resonance (NMR) has the capability to distinguish lithium ions in SEI and lithium in metallic status.[45–47] Bhattacharyya *et al* [46] firstly quantifies the mossy/dendritic lithium and smooth deposited lithium by ^{7}Li NMR. As demonstrated in Figure 1.19a, they utilized skin-depth effect (the finite penetrating ability of radiofrequency field) to differentiate dendritic lithium and bulk lithium. For lithium dendrites whose diameter is less than 2 µm, the RF could fully penetrate so that the signal is proportional to volume/mass; for bulk lithium, RF could only partially penetrate so that the signal is proportional to area. Figure 1.19b shows an example of $LiCoO_2$-Li cell during the first cycle: M_{Li} is the total mass of deposited or stripped Li extracted from electrochemistry; M_{μ} is measured microstructure Li, taking into account the skin-depth problem; M_{SD} is M_{Li} - M_{μ}. Even through NMR has the capability to distinguish SEI and metallic lithium, but the method introduced here is only effective in dendritic lithium measurement. In many advanced electrolytes, deposited lithium is no longer dendritic, but dense with little porosity, making NMR difficult to quantify.

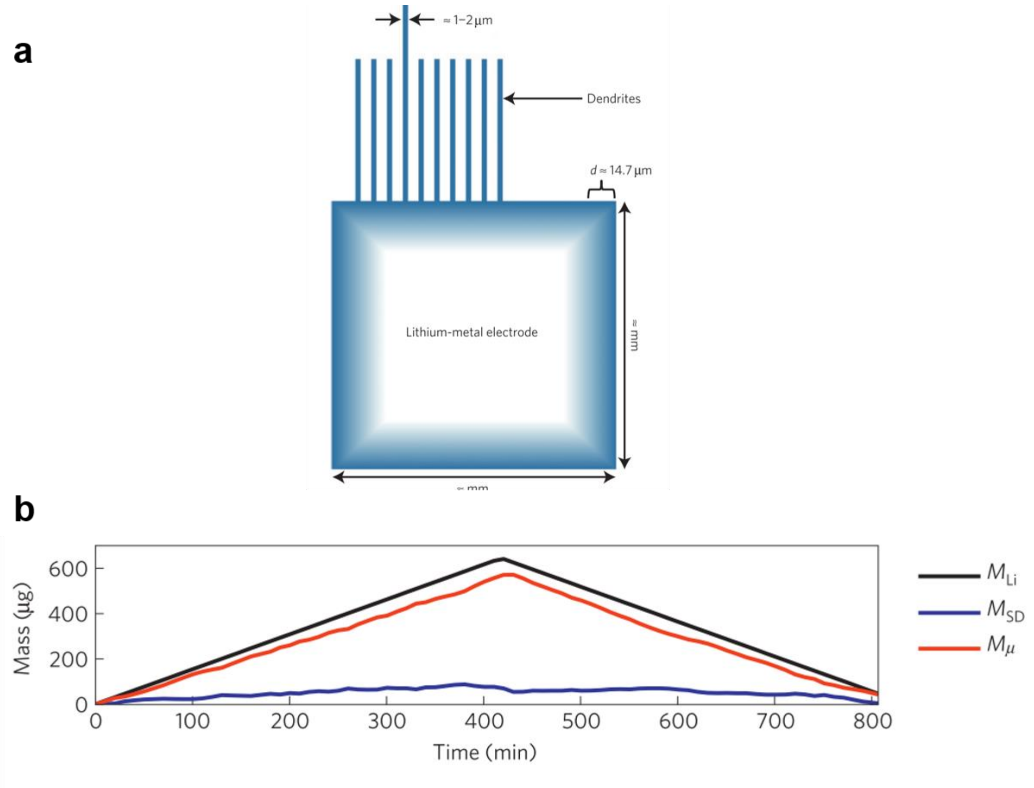

Figure 1.19 (a) schematic explaining "skin-depth" effect that the radiofrequency penetration in a block of lithium metal and in the whisker-like dendritic structures; (b) total mass of lithium deposited or stripped $M_{Li}(t)$ (extracted from the electrochemistry) can be used to calculate the mass of deposited lithium $M_{SD}(t)$ and lithium microstructures $M_{\mu}(t)$, taking into account the skin-depth problem.[46]

1.5 Motivation and Outline

The slow progress of battery technologies has become the bottleneck of many of today's cutting-edge electronic technologies, for example, electric vehicles and portable electronics. In order to realize next generation high-energy batteries, new cathode and anode materials are urgently needed.

For the cathode material, lithium (Li) rich layered oxides (LRLO) exhibit high reversible specific capacities over 300 mAh g^{-1}, attributing to the oxygen redox reaction. However, oxygen activity comes with instability in the form of oxygen loss, which is associated with irreversible voltage decay and capacity fading. In **Chapter 2**, a joint study of DFT calculation and experiments was carried out to investigate the elemental doping effects on LRLO performances. Calculation proves that incorporating 4d elements, such as Mo, enhances the material's structural stability by altering the local band structure and impeding oxygen vacancy formation. Experimentally, Mo is co-doped with Co into $Li[Li_{0.2}Ni_{0.2}Mn_{0.6}]O_2$, showing notably reduced voltage decay and capacity fading without sacrificing energy density and cycle life.

For anode materials, Li metal is critical to break the energy-density bottleneck of current Li-ion chemistry. Inactive Li formation is the immediate cause of capacity loss and catastrophic failure of Li metal batteries. However, its composition has not yet been quantitatively studied due to the lack of effective diagnosis tools that can accurately differentiate Li^+ in solid electrolyte interphase (SEI) components and the electrically isolated unreacted metallic Li^0, which together comprise the inactive Li. It is generally assumed that the low CE is dominated by the continuous repairing of SEI fracture that consumes both electrolyte and active Li metal[48], though a few works also suggested that unreacted metallic Li^0 may increase the tortuosity at the electrode/electrolyte interphase and decrease the CE[28,49]. Overall, most of these assumptions and hypothesis are observational, while the actual contribution to capacity loss from the SEI formation has never been successfully quantified. Consequently, efforts may be misdirected as we strive to make Li metal a valid anode material. Differentiating and quantifying the Li^+ and Li^0 remaining on the electrode after stripping, therefore, becomes the key to understanding the mechanisms leading to capacity decay. **Chapter 3** detailly introduces a new analytical method, Titration Gas Chromatography (TGC), to accurately quantify the contribution from unreacted metallic Li^0 to the total amount of inactive Li. Using the new TGC method, in **Chapter 4**, we identify the Li^0, rather than the (electro)chemically formed Li^+ in SEI, as the dominating cause for the inactive Li and capacity loss. Coupling the measurements of the unreacted metallic Li^0 global content to the observations of its local micro- and nano-structure by cryogenic electron microscopies, we also reveal the formation mechanism of inactive Li in different types of electrolytes, and determine the true underlying cause of low CE in Li metal deposition and stripping. We ultimately propose strategies for highly efficient Li deposition and stripping to enable Li metal anode for next generation high-energy batteries. **Chapter 5** summarizes the new findings and future perspectives.

Chapter 1, in part, is a reprint of the material “Key Issues Hindering a Practical Lithium Metal Battery” as it appears in the Trends in Chemistry, **Chengcheng Fang**, Xuefeng Wang, Ying Shirley Meng, 2019, 1, 152-158. The dissertation author was the primary investigator and author of this paper. The author wrote the paper.

Chapter 2 Mitigating Oxygen Release in Anionic-Redox-Active Cathode Materials by Cationic Substitution through Rational Design

2.1 Introduction

Lithium ion battery technology has enabled the advancement of handheld devices and electric vehicles, and has reached to grid-scale storage markets. To further these technologies, improving battery life and extending electric vehicle ranges, the energy density of LIB cathodes must increase well beyond the current reach of commercially available cathodes[50,51] Lithium rich layered oxide cathodes have sparked intense interest due to their strikingly high capacities, in excess of 250 mAh/g—well beyond the capacity of current commercial cathodes such as $LiCoO_2$, $LiMn_2O_4$ and $LiFePO_4$ (160, 120, and 168 mAh/g, respectively) [52]. This is generally attributed to anionic redox behavior—a phenomenon under intense scrutiny, yet widely accepted as the source of this capacity[53–55]. Unfortunately, the increased capacity is accompanied with a host of problems, including transition metal (TM) migration [56], surface phase transformations [57], and the irreversible release of oxygen[58,59]. Furthermore, this oxygen loss subsequently reduces the barrier for transition metal migration [60]. A combination of these effects leads to characteristic voltage decay and capacity fade. Many methods have been employed to combat this rapid degradation, including surface modification[61,62] and coating [63], morphological control [64], and incorporation of dopants [65]; each method shows a degree of improvement in one aspect of cycling, yet a comprehensive solution to Li-rich layered oxide cathodes shortcomings is still lacking. Despite the clear role of surface phase evolution in lithium rich layered oxide cathodes, the majority of oxygen activity occurs in the bulk, and doping remains an effective strategy for modifying bulk properties.

Most recent computational advances have described the notion of anionic redox in terms of two general phenomena: reorientation of oxygen ions into peroxo-like oxygen dimers, in the case of 4d transition metal layered oxides[55,66], and more relevant to 3d transition metal elements, the alignment of two lithium ions across an oxygen atom creating labile oxygen states, susceptible to redox [67]. Looking at doping in particular, an extensive amount of *ab initio* calculations and experiments have been performed in Li-rich layered oxide cathodes. Computationally, density functional theory (DFT) studies generally provide insight into structural modification, band structure, voltage, and diffusion behavior. Though the majority of these studies lack experimental interpretation, and, similarly, if experimental doping exists, these experiments lack description in terms of this computational work. A few noteworthy exemptions include the work of Deng *et al.* [65], Wang *et al.* [68], Xiao *et al.* [69], and Gao *et al.* [70]. Deng *et al.* [65] and Wang *et al.* [68] performed a range of cationic substitution experiments on lithium-rich layered oxides for a range of TM stoichiometries, and substituting Al, Co Cr, Fe, Ga and Ti into the NiMn framework; results showed an increased initial charging plateau for the Co substitution and decreased plateau for the Ti substitution, attributed to the degree of overlap between the dopant t_{2g} and O 2p orbitals, correlated to the extent of electron localization [65]. This work was followed up by a computational explanation of the impact of cation substitution on oxygen evolution, attributing increased oxygen loss to an effective decrease in band gap. The band gap is thought to serve as an impediment to charge transfer, a prerequisite for oxygen evolution [69]. Gao *et al.* [70] and Kong *et al.* [71] have performed the most comprehensive computational screening, both applied to Li_2MnO_3, Kong performing a comparative study between the classical layered and Li-rich analogue. Gao *et al.* [70] calculate oxygen release energies by removing anions with the lowest Bader charge on delithiation, predicting Nb-doping as a stabilizing agent, and Kong *et al.* [71] shows that typical dopants are thermodynamically stable within the Li-rich layered oxide framework and have the potential to alter electronic conductivity through hole polaron formation. Prior to this work, Gao *et al.* [72] had also calculated the impact of doping Mo into Li_2MnO_3, predicting a reduced band gap and improved Li mobility between Li and TM layers. Aforementioned doping experiments are generally difficult to describe via computation due to the potential for effects beyond purely bulk doping; as such, low doping amounts are used in this study to aid ease of dopant incorporation and prevent notable surface effects. Other experimental doping includes Ba into Li-rich NiMn layered oxide (LNMLO) cathode, showing improved rate capability [73] and B-doping into Li-rich NiMnCo showing modified crystallization [74], not calculation in this study. A multitude of other doping studies generally show that substitution of a small percentage of metal cations significantly alters cathode performance, though most experimental studies generally lack spectroscopic data and further lack the theoretical framework to understand the role of the dopant in these changes. Moreover, the importance of local environment to the dopant is not addressed in most computational work.

This work uniquely combines *ab initio* calculations of oxygen stability in LNMLO cathode material with experimental synthesis and characterization based on these findings, focusing on the notion of site-dependent anion stabilization in the lithium rich layered oxides. Analysis of the delithiated structure, subsequent structural changes, and bonding environment changes increase the complexity of the model, more closely resembling the true nature of an experimental material. Using first principles approaches, we show that oxygen vacancy formation is highly dependent on the local bonding environment, which has been shown to vary with the state of charge of the cathode. Using this site-based approach, we relate oxygen stability to the local environment changes during cycling. Findings of formation energies are rationalized using calculated data, showing a strong influence of doping on the charge density distribution, affecting the potential to form of oxygen vacancies. Doping of LNMLO with Al, Ti, Co, and Mo is then performed, clearly impacting the initial charging plateau associated with oxygen redox and loss. Al and Ti doping show little change to the oxygen redox plateau, as predicted by computation of the E_{Ov}^{F} calculations. Co-doping shows the opposite affect, due to increased oxygen loss from the lattice, again as predicted. When co-doped with Co and Mo, reduced oxygen loss, reduced voltage fade and improved capacity retention are observed. Incorporation of the Mo dopant is evident through X-ray diffraction, X-ray photoemission spectroscopy and energy dispersive X-ray spectroscopy. These findings demonstrate that *ab initio* calculations can be used to rationally select cation dopants to improve oxygen stability within the bulk of lithium rich layered cathode materials, while leaving oxygen available for reversible redox.

2.2 Experimental

2.2.1 Density Functional Theory (DFT)

A spin-polarized GGA+U approximation to the DFT was employed, to account for electron correlations in transition metal and rare earth elements. Projector augmented-wave method (PAW) pseudopotentials were used as implemented in the Vienna Ab Initio Simulation Package (VASP). The Perdew-Burke-Ernzerhof exchange correlation and a plane wave representation for the wavefunction with a cutoff energy of 450 eV were used. The Brillouin zone was sampled with a k-points mesh of 5 x 4 x 7 for structural relaxations and oxygen vacancy formation energy calculations and 10 x 8 x 14 for density of states (DOS) calculations, both by Gamma packing. Atomic coordinates and lattice vectors were fully relaxed for each structure. Effective U values used in the calculations are provided in the Supplemental Information, applied with the rotationally invariant approach [75].

2.2.2 Cathode Synthesis

Pristine $Li[Li_{0.2}Ni_{0.2}Mn_{0.6}]O_2$ (LNMLO), Co-doped $Li[Li_{0.144}Ni_{0.136}Co_{0.136}Mn_{0.544}]O_2$ (LNMLO-Co), and Mo-doped $Li[Li_{0.144}Ni_{0.136}Co_{0.136}Mn_{0.544}]_{0.99}Mo_{0.01}O_2$ (LNMLO-CoMo) materials were synthesized by carbonate co-precipitation method (CCP). TM nitrate solutions (Ni:Mn = 1:3, Ni:Co:Mn = 1:1:4, 1M) were titrated into $NaCO_3$ solution (0.2 M) under stirring. The pH value during the co-precipitation process was carefully controlled between 7.80 and 7.85 to avoid hydroxide precursor generation. The slurry was then aged at 80 ^oC for 12 hours. After washing and drying, the TM carbonate precursor was sufficiently mixed with a stoichiometric amount of Li_2CO_3 and MoO_2. The two-step calcination conditions are 500 °C for 5 hours and 850 °C for 15 hours.

Al-doped $Li[Li_{0.2}Ni_{0.19}Mn_{0.59}Al_{0.02}]O_2$ (LNMLO-Al) and Ti-doped $Li[Li_{0.2}Ni_{0.2}Mn_{0.59}Ti_{0.01}]O_2$ (LNMLO-Ti) lithium rich layered oxide cathode materials were prepared through hydroxide co-precipitation method (OHCP). Synthesis of TM (Ni, Mn) hydroxide precursors was detailed in our previous work [76]. Then the as-prepared TM precursors were mixed with a stoichiometric amount of $LiOH\cdot H_2O$ and Al_2O_3 (for Al-doped sample). Ti was incorporated during co-precipitation process by using $Ti(OC_4H_9)_4$. After grinding for 30 minutes, the mixture was then annealed by two steps, 480 °C for 12 hours and 900 °C for 12 hours in air, to get the final product.

2.2.3 X-ray Diffraction (XRD)

XRD spectra were acquired using a Bruker D8 advance diffractometer with a Bragg-Brentano θ-2θ geometry and a Cu Kα source ($\lambda = 1.54$ Å). Samples were scanned from 10° to 80° at a scan rate of 0.05°/step. Rietveld refinement was performed using FullProf software.

2.2.4 X-ray photoemission spectroscopy (XPS)

XPS was performed using a Kratos AXIS Supra with the Al anode source operated at 15 kV. The chamber pressure was $< 10^{-8}$ Torr during all measurements. High-resolution spectra were calibrated using the hydrocarbon C1s peak at 284.6 eV. Data fitting was performed using CasaXPS software using a Shirley-type background.

2.2.5 Electrochemical Measurement

Electrochemical performances were measured using an Arbin battery cycler in galvanostatic mode between 2.0 – 4.8 V vs. Li/Li^+, at a current density of 12.5 mA/g for first cycle, 25 mA/g for following cycles. Cathodes, consisting of 80 wt % of active materials, 10 wt % of Super P carbon and 10 wt % of poly(vinylidene fluoride) (PVDF) binder, were assembled into standard 2016 coin cells with Li metal as the anode and 1 M $LiPF_6$ in ethylene carbonate/dimethyl carbonate (EC:DMC in 3:7 weight ratio) as the electrolyte. The mass loading is ~ 3 mg/cm^2. The plateau length refers to the capacity above 4.4 V after aligning the plateau voltage of doped materials to that of pristine materials. Electrochemical impedance spectroscopy (EIS) measurements were carried out with 10 mV perturbation and ac frequencies from 0.01 to 1×10^6 Hz on galvanostatic cycled electrodes at OCV and 30 cycles. The electrodes were assembled in a R2016 coin cells, where the active materials are the working electrodes and Li metal serves as the counter electrode. A Solatron 1287 Potentiostat was used to measure the impedance. After the EIS measurements were taken, an equivalent circuit model was fit to the data to analyze the reactions that took place using Z view software (v. 3.4a, Scribner Associates, Inc.).

2.3 Results and Discussion

2.3.1 Oxygen Vacancy Formation Energy

A model supercell was used containing 14 Li (2 within the transition metal layer), 3 Ni, 7 Mn and 24 O, corresponding to a stoichiometry of $Li[Li_{2/12}Ni_{3/12}Mn_{7/12}]O_2$. In this manuscript, the fully lithiated state is referred to as "pristine", and the lack of dopants as "undoped". For doping studies, one ion, M, is substituted for Mn, resulting in a stoichiometry of $Li[Li_{2/12}Ni_{3/12}Mn_{6/12}M_{1/12}]O_2$, similarly referred to as "M-doped". Optimal coordination of atoms within the transition metal layer were determined through structural relaxations, and are consistent with previously published work [57]. This configuration, shown in Figure 2.1a, creates four local TM environments surrounding oxygen ions, though this number is expanded with the incorporation of dopants and delithiation of the structure. Li-rich materials initial charging plateau following transition metal redox is attributed to oxygen evolution [64]. As such, the state of delithiation selected for analysis of oxygen evolution is at a lithium concentration of 8/14, referred to as "delithiated". The relaxed structure on delithiation of the supercell was determined by analyzing energies of all permutations of lithium removal. From this relaxed supercell, each oxygen atom was removed and a final calculation was performed. The oxygen vacancy formation energy, E_{Ov}^{F}, was calculated by

$$E_{Ov}^{F} = E\left(Li_{\frac{8}{12}}Ni_{\frac{3}{12}}Mn_{\frac{7}{12}}O_{2-\frac{y}{12}}\right) + \frac{y}{24}E(O_2) - E\left(Li_{\frac{8}{12}}Ni_{\frac{3}{12}}Mn_{\frac{7}{12}}O_2\right) - 1.36$$

where the -1.36 eV correction factor is included to account for overbinding in $+U$ calculations, the oxygen vacancy formation energy was determined for each of these sites [77]. A similar process was performed for dopant incorporation, first determining the most stable site of the particularly dopant, delithiating, and extracting oxygen, further described in the Supplemental

Information.

To briefly discuss current understanding of oxygen redox in Li-rich cathode materials, there are a few theories pertaining to the mechanism leading to oxygen oxidation: most prevalent theories are the formation of a peroxo-like species [55,78] and the formation of electron holes in certain oxygen bonding environments [58,79]. The notion of the peroxo-like formers has been experimentally viewed, but further computational and experimental work suggests that this phenomenon is limited to the case of 4d and 5d transition metal oxides, which may be phenomenologically viewed as having weaker localized bonding with oxygen, and allowing more flexible bond angles with the subsequent formation of O-O bonds[78–80]. For the case of more traditional, commercially relevant materials consisting of 3d TM elements, TM-O bonds are viewed as more rigid. Both computation and experiment view the formation of peroxo-groups in these materials unlikely, and further evidence supports the presence of localized electron holes [80]. A similar rigidity is observed both in literature [67] and in our model calculations, for TM-O bonds. It is further noted that through the application of GGA+U, similar to the previously demonstrated use of hybrid functionals [67], an increased partial density of states is observed near the Fermi energy for oxygen ions exhibiting a Li-O-Li bond (Supplemental Information). Despite the advantage of labile oxygen, as reflected in the initial charge capacity of lithium rich layered oxides, these easily oxidized anions also exhibit reduced bonding stability and are subject to removal. As such, calculation of E_{Ov}^{F} is critical in understanding anion stabilization.

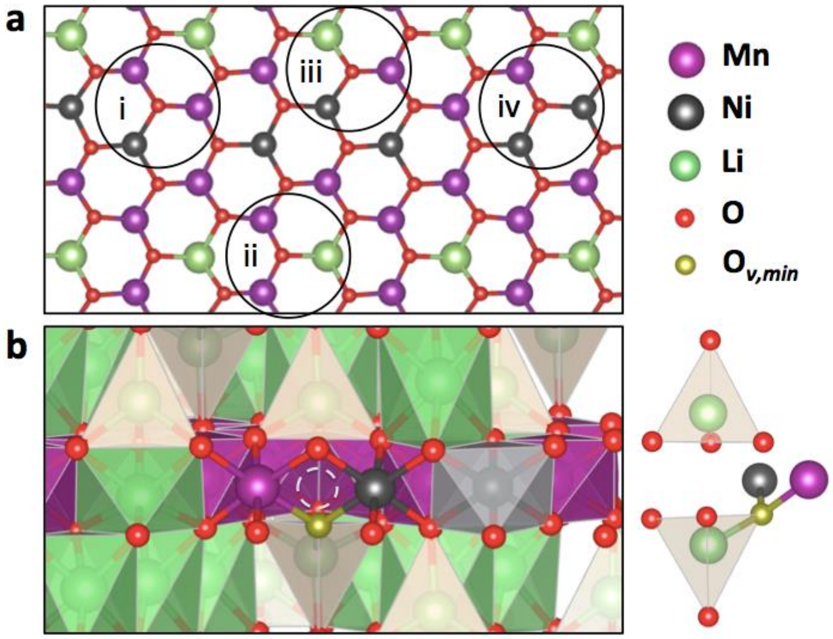

Figure 2.1 The undoped structural model used in this study contains four general TM environments for each oxygen atom: (i) Mn-Mn-Ni, (ii) Mn-Mn-Li, (iii) Mn-Ni-Li, and (iv) Mn-Ni-Ni; (b) Relaxed structure contains a wider range of neighboring configurations, including the formation of lithium dumbbells, isolated at right, around lithium vacancies within the transition metal layer (dashed circle).

From the calculated E_{Ov}^{F} results, a wide range of E_{Ov}^{F} is observed in the undoped, delithiated structure. To understand this E_{Ov}^{F} variation, it is first necessary to examine the relaxed structure of the undoped material, delithiated to the point where oxygen is experimentally observed to release from the lattice. The broad range of local atomic environments in the relaxed structure is seen to directly impact E_{Ov}^{F}, and is generally overlooked in simulated oxygen vacancy formation energy calculations. A critical feature of this relaxed structure is the formation of the lithium dumbbell or the migration of lithium ions to tetrahedral sites surrounding a TM-layer lithium vacancy, shown in Figure 2.1b [57]. A few trends are observed related to the variation in E_{Ov}^{F} in Figure 2.2. The lowest energy sites contain three critical environmental factors: (1) the presence of a Ni nearest neighbors generally results in a lower oxygen vacancy formation energy, due to reduced electrostatic repulsion between the oxygen vacancy (effectively a positive charge) and the less positive Ni cation [60]; (2) a minimized coordination with cations; and (3) subsequently occurs near a TM layer lithium vacancy and hence is in proximity to a tetrahedral lithium ion. The migration of lithium to the tetrahedral site creates a local environment loosely resembling a trigonal plane with a tetrahedral lithium, Ni ion, and Mn ion as vertices. Intuitively, this distorted trigonal planar environment does not well suit the orbital symmetry of oxygen ions, and the reduced bonding stability is evident through the reduced E_{Ov}^{F}.

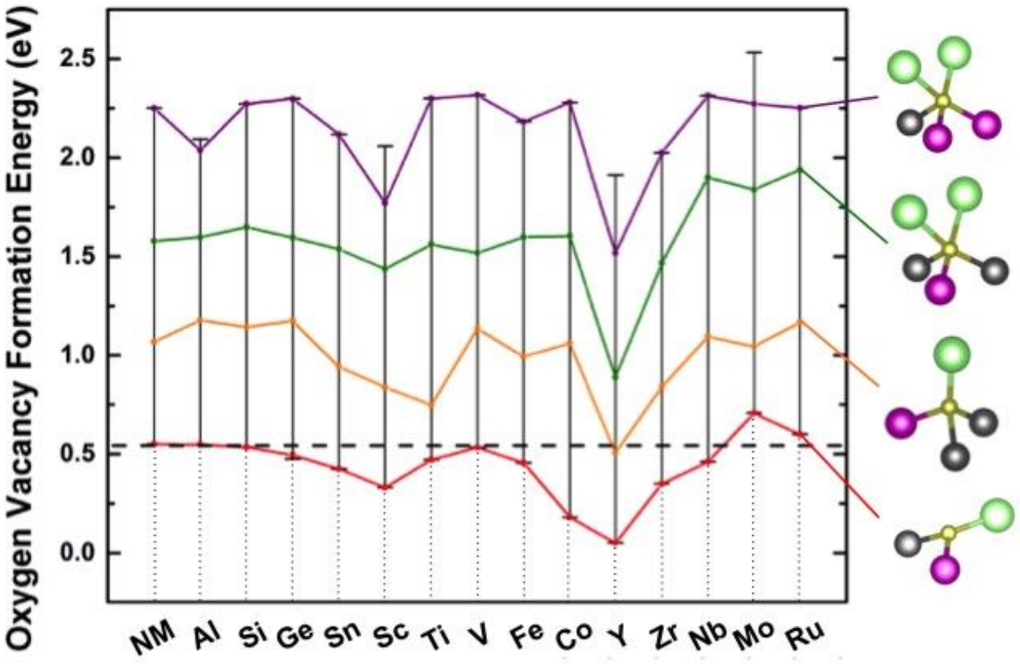

Figure 2. 2 Distribution of oxygen vacancy formation energies, $E_{Ov,}^{F}$ for each oxygen site for a full range of dopants. Representative bonding environments are indicated to reflect their relative E_{Ov}^{F}.

2.3.2 Impact of Dopants on Oxygen Stability

Generally, a similar range in E_{Ov}^{F} is present in the doped and delithiated structures, though doping is seen to alter the distribution and magnitude of these energies. Al, Ti, Co and Mo were selected as representative dopants for further analysis, either showing little (Al, Ti) or notable changes (Co, Mo) in E_{Ov}^{F}. Of the simulated dopants, Mo and Ru are predicted to raise the E_{Ov}^{F} of the lowest energy site for oxygen release. Despite Ru having shown an enhanced E_{Ov}^{F}, as well as interesting properties when used in lithium rich layered oxides, showing the formation of peroxo-like species on discharge [81], the advantages of Ru doping are far outweighed by its cost, and hence will not be further discussed as a dopant in this work. Similar to the undoped scenario, the lowest E_{Ov}^{F} is present at same local environment displaying the near-trigonal planar configuration. Al and Ti are further discussed for analytical comparison due to the calculated E_{Ov}^{F} being similar to that of the undoped material, and are of further interest due to their reduced cost and low toxicity, respectively. Last, Co was selected due to its predicted decrease in E_{Ov}^{F}, enhancing oxygen release, and its relevance in commercial cathode use. Co is also unique in that its predicted location is in proximity to the most volatile oxygen site (i.e., lowest E_{Ov}^{F}), which may further promote instability and oxygen loss.

To rationalize this predicted oxygen vacancy formation energy change, a site-dependent analysis of the delithiated charge density distribution and density of states (DOS) were performed to determine if the dopant affected the electronic behavior of the cathode material. First, a Bader charge analysis was performed to observe trends in electron density with the incorporation of dopants, detailed in the (Table 2.5). In previous oxygen vacancy formation studies [70,72], oxygen sites with the lowest Bader charge and largest Bader charge difference between pristine and delithiated states are supposed to evolve most easily, and these sites are generally used for the E_{Ov}^{F} calculations. While this is the case for incorporated 3d transition metal dopants, Mo-doping shows a discrepancy between oxygen sites with maximum Bader charge difference and minimum E_{Ov}^{F}. Mo-doping also shows the highest net increase in charge density associated with oxygen sites.

To better understand electron charge redistribution, charge density differences were calculated (Figure 2.3). For clarity, charge density differences between undoped and doped structures were calculated for the same dopant site, and in the case of Co will not reflect the exact bonding environment present in the minimum E_{Ov}^{F} value. However, for the intent of observing change in charge distribution, the simulation yields fundamentally applicable results. Intuitively, Al-doping presents a local charge deficiency, and the redistribution of charge on surrounding O 2p orbitals is a coulombic effect; this redistribution is local, and does not extend far beyond the immediate AlO_6 octahedron. Converse to Al, Ti-doping predicts an increased charge density on the oxygen in the surrounding TiO_6 octahedron; though similarly, the charge redistribution does not extend beyond the octahedrally coordinated oxygen. Variations in the charge density of Co- and Ti-doped structures reflect the modified bonding relative to the original Mn environment. The Co bonding results in a charge reduction on surrounding oxygen ions; as this Co is actually neighboring the lowest E_{Ov}^{F} site, this oxygen ion will directly experience the reduced charge density and will more directly impact this site. Last, Mo shows the most significant charge redistribution, increasing charge density to local oxygen p orbitals. Interestingly this charge redistribution extends beyond the MoO_6 octahedron, increasing the charge density of the trigonal-planer-like oxygen site, a potential source of reduction of E_{Ov}^{F}.

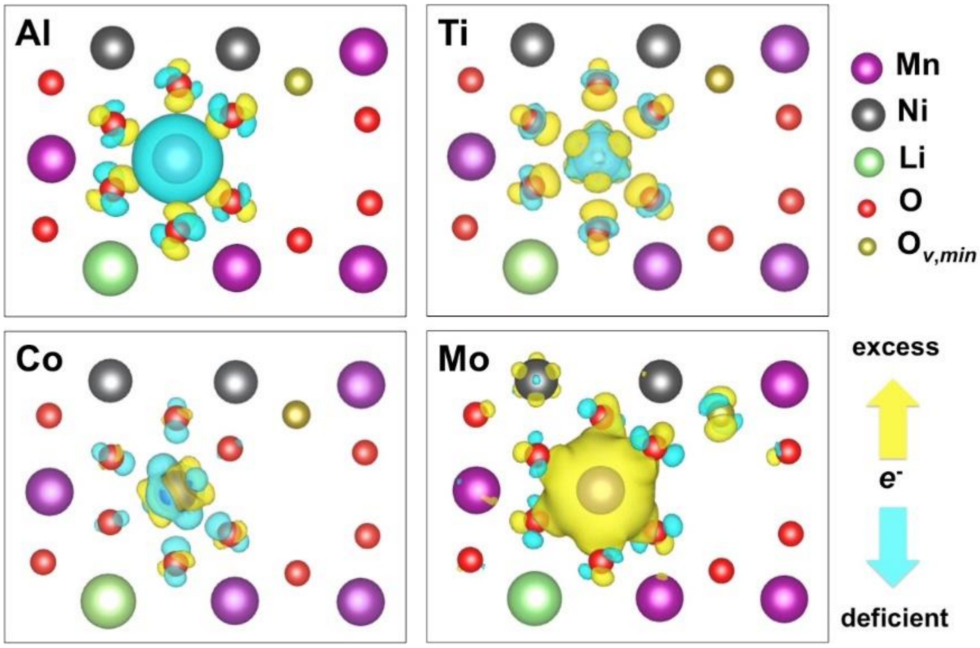

Figure 2. 3 The difference in charge densities between undoped and doped structures (delithiated state; iso-surface of 0.01 electrons/Bohr^3) elucidates the alteration of electron distribution and bonding upon introduction of a dopant. Most notably, Mo-doping results in diffusely distributed electron excess, having a more notable change to the most susceptible bonding environment to oxygen loss. $O_{v,min}$ (gold ion) denotes the minimum E^F_{Ov} site.

E^F_{Ov} results are further described by the DOS calculations of the lowest E^F_{Ov} oxygen site and surrounding ions. Figure 2.4 shows that most dopants have little local impact on the DOS of this site, but for the case of the Mo-dopant a notable shift of the energy of local bonding orbitals below the Fermi energy is observed. This shift creates a barrier to charge transfer between bonding and antibonding orbitals for this particular oxygen ion, subsequently impeding the removal of oxygen from the oxygen sublattice. Integration of the oxygen DOS between the Fermi energy and -1.5 eV shows a 27% increase in the electron density in the O 2p orbitals. This extra charge, due to the charge reconfiguration from Mo-doping, is the likely source of the relatively increased Fermi energy of the local bonding orbitals.

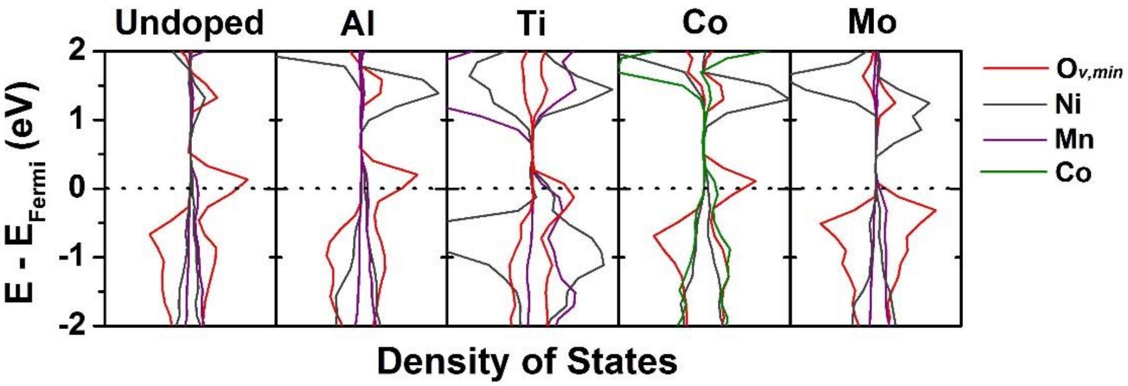

Figure 2. 4 The partial density of states for the lowest E_{Ov}^{F} site prior to oxygen removal. Analysis shows that Mo doping shifts the bonding states below the Fermi energy, and increases electron density below the Fermi energy, a potential sources of anion stabilization.

2.3.3 Experimental Observations

Guided by the E_{Ov}^{F} calculations, synthesis preceded with the dopants previously discussed in terms of calculation results: Co, Mo, Al, and Ti are, incorporated into pristine Li-rich layered oxide cathode (LNMLO).

Co-doped LNMO (LNMLO-Co) was examined to observe the potential decrease in oxygen stability of the cathode material. It is known that Co readily forms a solid solution with LNMLO at large concentrations, allowing an amount of Co to be doped into LNMLO consistent with calculations. Shown in the works of Deng *et al.* and Wang *et al.*, electrochemical cycling can be partially described in terms of the calculated oxygen stability [65,66]. The initial charging plateau in the cycling profile is attributed to both reversible anion redox and irreversible oxygen evolution. As predicted computationally, the Co-doped sample shows an extended initial charging plateau relative to the undoped material. As shown in Figure 2.5a, the plateau length of LNMLO is 228.0 mAh/g, while that of LNMLO-Co increases to 266.9 mAh/g. Cycling instability of the material is further presented in the form of the severe voltage decay after 50 cycles, shown in Figure 2.5c. The average voltage retention after 50 cycles decreases from 97% to 93.6% after Co doping. As compared in Figure 2.5e, LNMLO-Co delivers significantly improved discharge capacities in the initial several cycles but drops sharply. The LNMLO-Co shows a first discharge capacity of 290 mAh/g, while that of pristine LNMLO only delivers 220 mAh/g reversible capacity. After 50 cycles, the capacity of LNMLO-Co only maintains 79.3% of initial capacity, 230 mAh/g. Yet, the capacity of LNMLO slightly increases to 232 mAh/g. The experimental observations are in complete agreement with the computational prediction that Co doping leads to decreased oxygen stability, resulting in increased irreversible oxygen gas evolution.

Aiming to provide insight for practical application, obtaining high energy density while maintaining excellent cycling stability, Mo doping is performed on LNMLO-Co material. 1% of Mo was doped into bulk of LNMLO-Co, as will be evident. Doping of 3% of Mo into LNMLO-Co (LNMLO-CoMo) structure was also attempted; however, impurity peaks appear (Figure 2.14), consistent with previous literature. 1% is likely near the maximum amount of doping into the structure, due to the large ionic radius of Mo [82]. The first charging curve of LNMLO-CoMo (Figure 2.5b) shows a reduced initial charging plateau (253.4 mAh/g) compared with LNMLO-Co (266.9 mAh/g). This indicates, conversely to the Co material, a reduction in electron charge transfer from oxygen, which would otherwise accompany the irreversible oxygen loss from the lattice. The material also shows moderately less voltage decay after 50 cycles (Figure 2.5d). The average voltage retention improves by 0.6% with Mo doping. Last, and most notably, the specific capacity and cycling stability are greatly improved. As shown in Figure 2.5e, LNMLO-CoMo delivers a high reversible capacity of 297 mAh/g. After 50 cycles, the capacity remains 256 mAh/g with retention of 86.5%. A detailed electrochemical performances comparison of the three samples is shown in Table 2.1. Electrochemical Impedance Spectroscopy (EIS) measurements are carried out to understand the different electrochemical behaviors of LNMLO-Co and LNMLO-CoMo. As compared in Figure 2.11, at OVC state, both cells only show one semicircle, which represents charge transfer resistance (Rct). After 30 cycles, SEI built on the surface of cathode materials, thus an additional semicircle can be measured at high frequency region, representing resistance of SEI film (Rsei). W is the Warburg impedance related to bulk lithium ion diffusion. The fitting values are listed in Table 2.6. Mo-doped sample shows reduced Rct before and after cycling, and much smaller Rsei after 30 cycles, indicating that fast electron transfer and facile lithium ion diffusion path have been achieved after Mo doping. Even though only 1% of Mo is added, Mo doping in deed significantly changes the local electronic structure and crystal structure, thus both electronic conductivity and ion diffusion are notably improved. More evidence for Mo incorporation into crystal structure will be specified later. The above results clearly show the positive effect of Mo doping on electrochemical performance.

Table 2. 1 A comparison of electrochemical performance parameters of LNMLO, LNMLO-Co and LNMLO-CoMo.

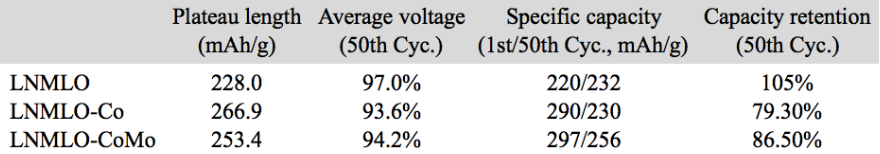

	Plateau length (mAh/g)	Average voltage (50th Cyc.)	Specific capacity (1st/50th Cyc., mAh/g)	Capacity retention (50th Cyc.)
LNMLO	228.0	97.0%	220/232	105%
LNMLO-Co	266.9	93.6%	290/230	79.30%
LNMLO-CoMo	253.4	94.2%	297/256	86.50%

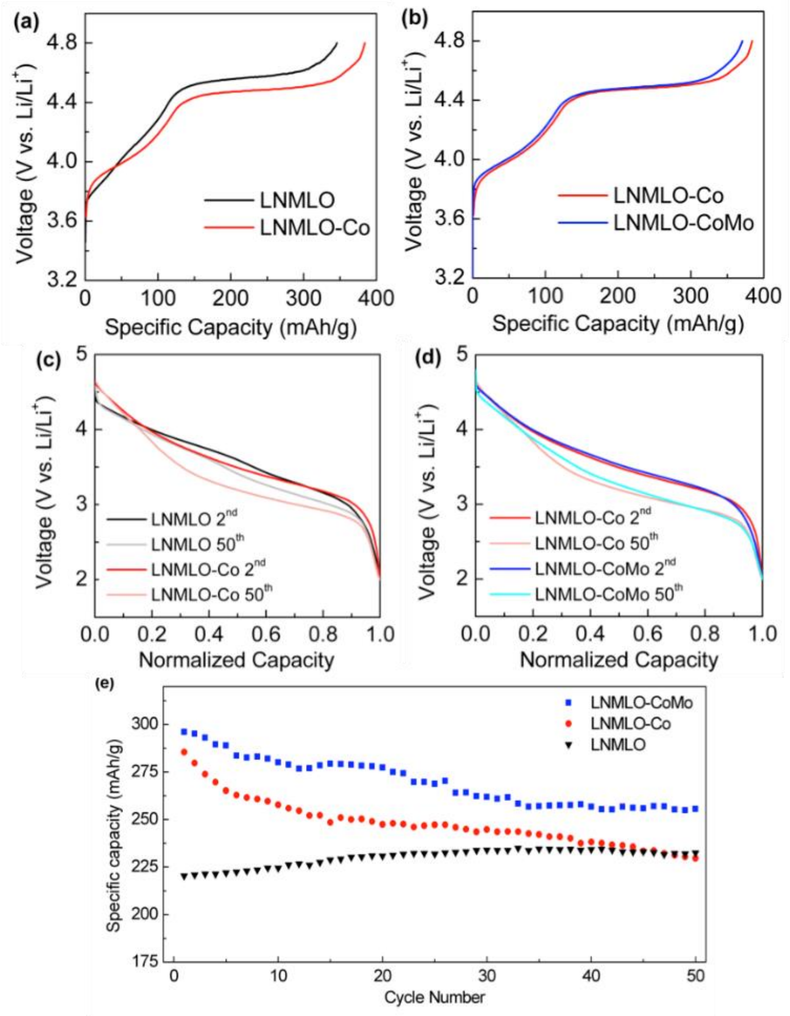

Figure 2. 5 Cycling results of LNMLO, LNMLO-Co, and LNMLO-CoMo. Incorporation of Co (a) is shown to increase the initial charging plateau, where Mo-doping (b) reduces the plateau, suggesting reduced oxygen gas evolution. Mo-doping further shows reduced voltage decay (d) and improved capacity retention (e).

The incorporation of Mo into the structure was verified by X-ray diffraction (XRD), X-ray photoemission spectroscopy (XPS), energy dispersive X-ray spectroscopy (EDS) of focused ion beam cross-sectioned secondary particles (FIB-EDS) and scanning transmission electron microscopy (STEM) mapping: (1) Figure 2.12 compares XRD and Rietveld refinement results of LNMLO, LNMLO-Co and LNMLO-CoMo materials. The lattice parameter variation trend of the three materials is shown in Figure 2.6. Co^{3+} (0.545 Å) doping leads to shrinking of a- and c- lattice parameters compared with pristine LNMLO. A slight a-lattice expansion is caused by Mo^{5+} (0.61 Å) substitution into the structure, also noting that Mo^{5+} doping causes significant expansion of c-, due to the increased Mo-O bond length. The increased c-lattice parameter facilitates Li^+ diffusion, explaining in part the increment of capacity in LNMLO-CoMo material. (2) Figure 2.7 compares the XPS analysis of LNMLO-Co and LNMLO-CoMo samples. Results of the XPS suggest that most of the Mo dopant takes the Mo^{5+} oxidation state in the pristine state. Specifically, the two peaks at binding energies of 231.7 eV and 234.8 eV are attributed to Mo^{5+}. Weak shoulders at higher binding energy of 232.8 eV and 236 eV indicate a small amount of Mo^{6+} [83]. Oxidation states of TM's are predicted using magnetization data from DFT calculations (Table 2.2), and calculate Mo in the pristine state to have a +5 charge. This dopant is predicted to be oxidized to Mo^{6+} on the first delithiation, not explored in this work. Oxidation states of Ni show no change, as the peak at 854.5 eV does not shift after Mo doping. Mn appears to be slightly reduced, again consistent with computation results. The predicted mixed valence of Mn may enhance the conductivity of the material, partially explaining the increased specific capacity [82]. Co is slightly reduced after Mo doping, as the satellite peak area increases from 6.84% to 8.99% after doping [84]. (3) Further evidence of a homogeneous distribution of the Mo dopant was observed by focused ion beam cross-section of a secondary particle coupled with EDS, as shown in Figure 2.15. It is noted that Mo-doping has indeed been explored for lithium rich layered oxides Li_2MnO_3 [85], $Li[Li_{0.2}Ni_{0.2}Mn_{0.6}]O_2$ [82], and $Li[Li_{0.2}Mn_{0.54}Ni_{0.13}Co_{0.13}]O_2$ [69,70], and in the case of Li_2MnO_3, Mo^{5+} was observed by X-ray absorption spectroscopy. Though again, little to no emphasis was placed on the stabilization of oxygen within the lattice in these prior works.

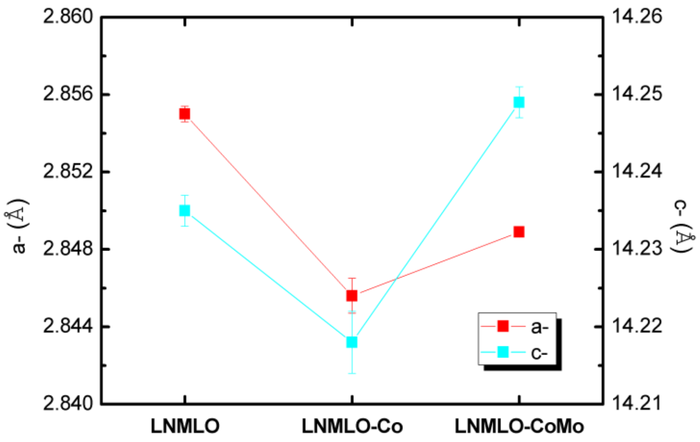

Figure 2. 6 Lattice parameters of LNMLO, LNMLO-Co and LNMLO-CoMo as determined by Rietveld refinement of XRD spectra (Figure 2.12).

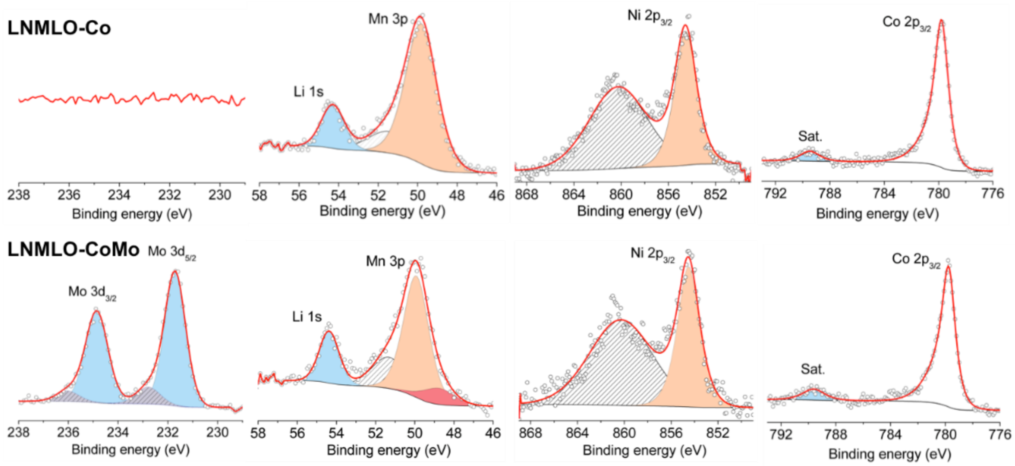

Figure 2. 7 XPS of LNMLO-Co and LNMLO-CoMo show that Mo took the predicted Mo^{5+} valence. Results further show a portion of the Mn is reduced from Mn^{4+} to Mn^{3+}.

Table 2. 2 Impact of dopant on oxidation state change on delithiation and oxygen removal of redox-active ions, as measured by simulated magnetizations. The multiplier refers to instances of the redox change within a single supercell.

Dopant	Theor. Redox change	
No dopant	$Ni^{2+} \rightarrow Ni^{3+}$	x 2
	$Ni^{2+} \rightarrow Ni^{4+}$	x 1
Al	$Ni^{2+} \rightarrow Ni^{3+}$	x 2
	$Ni^{2+} \rightarrow Ni^{4+}$	x 1
Co	$Ni^{2+} \rightarrow Ni^{3+}$	x 2
	$Ni^{2+} \rightarrow Ni^{4+}$	x 1
Mo	$Ni^{2+} \rightarrow Ni^{3+}$	x 2
	$Mn^{3+} \rightarrow Mn^{4+}$	x 1
	$Mo^{5+} \rightarrow Mo^{6+}$	x 1

Similarly, Al and Ti were chosen to verify the negligible impact on oxygen evolution as observed by the electrochemical performance of LNMLO, according to calculation prediction. Numerous studies have doped Al and Ti in a range of concentrations, each with varying results [86,87]. In spite of discrepancies in optimal doping concentrations, a small amount of substitution (1%, 2%) consistently shows notable deviations from the undoped cases. With the intent to prevent possible surface coating effects from excess dopant content, 2% Al (LNMLO-Al) and 1% Ti (LNMLO-Ti) doping into LNMLO is performed to re-evaluate the impact of doping in terms of oxygen behavior. In Figure 2.8a and b, first charging curves of LNMLO-Al and LNMLO-Ti materials both show an oxygen plateau of a similar width to that of the undoped LNMLO. Specifically, the plateau length of LNMLO-Al and LNMLO-Ti are 212 and 206 mAh/g, respectively, near that of pristine LNMLO is 204 mAh/g, indicating Al and Ti doping have a weak influence on oxygen activities; this is in line with calculations, having shown little change in the lowest E_{Ov}^{F} site. Figure 2.8c and d show further evidence for the relatively small impact of Al and Ti doping, exhibiting similar voltage decay to the undoped material after 100 cycles. The average voltage retention of LNMLO-Al, LNMLO-Ti and LNMLO are 96.7%, 96.2% and 96.4%, respectively, indicating little change after Al and Ti doping. However, it is worth mentioning that our conclusions on Al and Ti doping into lithium rich layered oxides are not in agreement with most previous studies, as variations of electrochemical performances were observed after doping in these other works. For instance, Nayak *et al.* reported that doping $Li_{1.2}Ni_{0.16}Mn_{0.56}Co_{0.08}O_2$ by Al results in a decreased capacity but improved cycling stability, as well as reduced average discharge voltage decay [87]. As mentioned before, Wang *et al.*'s and Deng *et al.*'s experimental work also shows that higher substitution amounts (6-20%) of Al and Ti doping lead to a suppression of oxidation of O^{2-} ions to oxygen [68]. Though based on both of our computational and experimental results, we speculate the more drastic changes in electrochemical behaviors in these previous works may to some extent be attributed to incomplete dopant incorporation and subsequent surface effects.

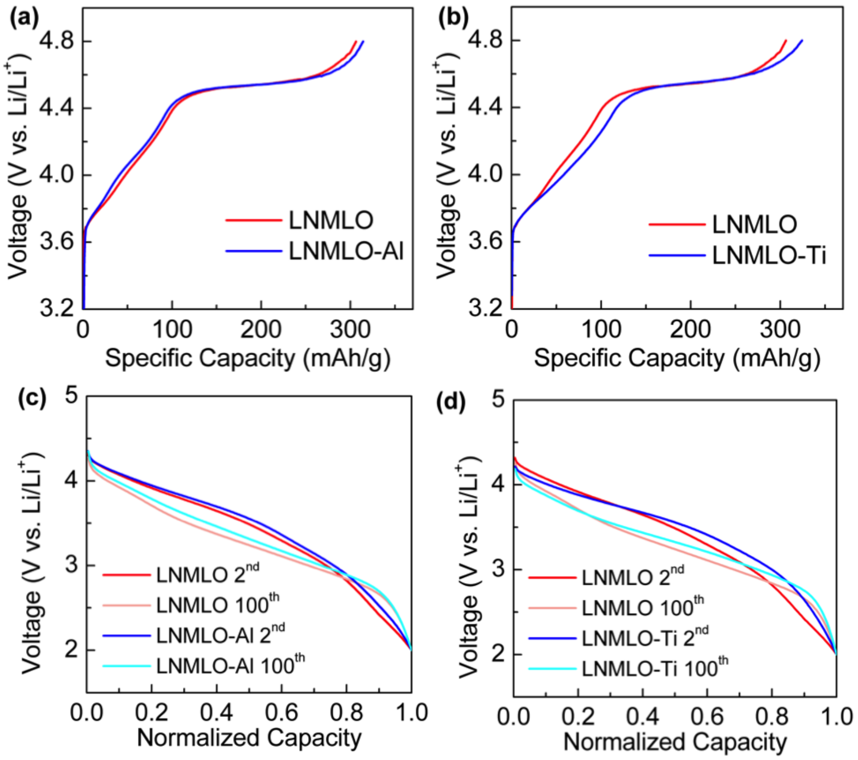

Figure 2. 8 (a) First charging profiles of LNMLO-Al and LNMLO-Ti materials, compared with pristine LNMLO. Oxygen plateau length of doped materials is similar to that of pristine material, commensurate with DFT calculations. (b) LNMLO-Al, LNMLO-Ti and LNMLO show similar voltage decay after 100 cycles, indicating Al- and Ti- doping does not have influence on electrochemical performance.

To verify the phase purity and observe structure changes of as-synthesized materials, X-ray diffraction and subsequent Rietveld refinement were performed (Figure 2.13). For LNMLO-Al, two dopant ions per formula unit substitutes one Ni^{2+} (0.69 Å) and one Mn^{4+} (0.53 Å) to maintain charge balance during synthesis. The decreased lattice parameters of LNMLO-Al can be ascribed to the smaller ionic radius of Al^{3+} (0.535 Å). Accordingly, the refined experimental a-lattice parameter of LNMLO-Ti does not show obvious change compared with that of undoped LNMLO. Variation in structural parameters with cation substitution was also calculated by DFT (Table 2.3). It was predicted that Al-doping results in a slight contraction of the *a* and *c* lattice parameters, showing reduced bond lengths in the MO_6 octahedron. Further consistent with experiment, Ti is predicted to expand the *c* lattice parameter, due to the increased Ti-O bond lengths relative to the replaced Mn-O bond lengths. As shown in Figure 2.13 and Table 2.3, experimental fittings show these values to generally follow the predicted trends. The XRD results suggest Al and Ti have been successfully doped into the structure.

Table 2. 3 Lattice parameters from DFT calculation (Theoretical) and from Rietveld refinement (Experimental) for Al and Ti doping

	Theoretical		Experimental	
	a=b (Å)	c (Å)	a=b (Å)	c (Å)
Undoped	2.908	14.435	2.8600(7)	14.241(3)
Al	2.897	14.421	2.8548(8)	14.235(4)
Ti	2.907	14.482	2.8599(1)	14.253(2)

Experimentally, a variety of dopants, including Al, Ti, Co and Mo, were selected to evaluate the impact on initial charge plateau, voltage fade, and capacity loss, and results are presented in the context of *ab initio* calculations. The observed electrochemical performance suggests that Al and Ti doping shows little impact on oxygen activities, having no effect on the width of the initial charging plateau; Co leads to decreased oxygen stability, increasing the width of the plateau; incorporation of Mo can mitigate oxygen loss from the lattice to some extent—consistent with E_{Ov}^{F} calculations. In this work, both theoretical and experimental findings show Mo-doped LR-NMC shows the highest specific capacity and improved cycling stability.

Full structural model description

For brevity, a complete description of the model was omitted from the full text. A number of considerations were put into the development of a model for the incorporation of a dopant into the $Li_{12}[Li_2Ni_3Mn_7]O_{24}$ supercell. First, the location of the dopant may vary between doping cases. As a rule of thumb, delithiation and E_{Ov}^{F} calculations were performed on the lowest energy configuration for each dopant scenario. It should be noted that the local environment of a particular oxygen vacancy does not necessarily contain the same local environment across dopants. Similarly, the incorporation of a dopant is naturally accompanied by an increased variety of local environments (Figure 2.9). However, the general trends to remain the same: in the relaxed structure, the oxygen vacancy near a combination of a nickel atom, a transition metal layer lithium vacancy, and a lithium-layer lithium that has migrated to a tetrahedral dumbbell site consistently produces the lowest E_{Ov}^{F} site.

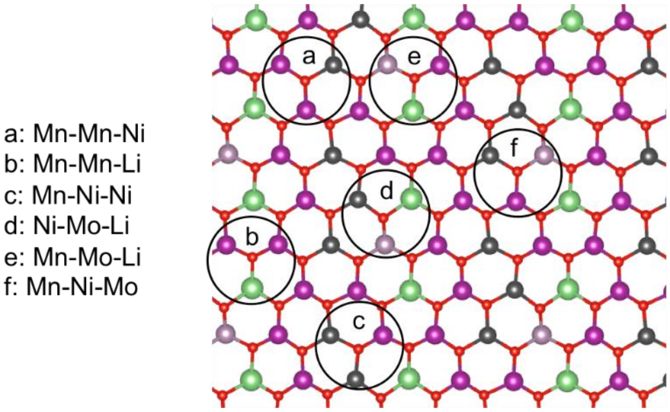

Figure 2. 9 Incorporation of dopants introduces a wider range local bonding environments. The Mo-doped structure is shown as an example.

Mott-Hubbard values used in the GGA+U calculations in this work are provided in Table 2.4 below. It is apparent that the +U parameter may have a drastic impact on the results of density functional theory calculations. Care was taken to use well-established values these cases, and where not established for energy storage materials, follow literature values with experimentally confirmed values.

Table 2. 4 Mott-Hubbard values and references used in the $+U$ calculations in this work [88–97].

	$+U_{eff}$	Ref.		$+U_{eff}$	Ref.
Sc	6	1	Ni	6	4
Ti	4.2	2	Y	5.08	6
V	4	3	Zr	2	7
Mn	6.96	4	Nb	2.07	8
Fe	4.3	5	Mo	2.5	9
Co	4.91	5	Ru	3	10

Calculation results in the context of oxygen redox

As shown in previous work, the notion of labile oxygen is observed computationally through he increased density of states below the Fermi level of oxygen atoms coordinated with TM layer lithium. This work, having used GGA+U similarly shows an increased oxygen density of states below the Fermi level for oxygen with a linear Li-O-Li bond (Figure 2.10b), suggesting that electronic structure for oxygen redox is still observable using the GGA+U functional. Conversely, oxygen sites lacking the Li-O-Li bond lack this delocalized density (Figure 2.10a).

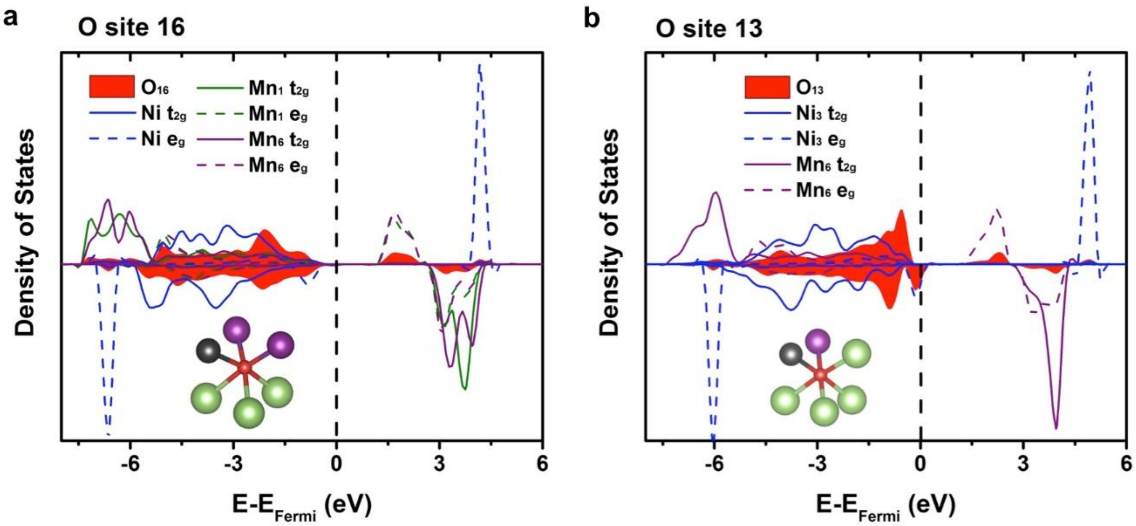

Figure 2. 10 An example of an oxygen site in the fully lithiated structure (a) without a Li-O-Li linear bond and (b) with a Li-O-Li linear bond, required for labile oxygen states. The presence of the Li-O-Li linear configuration shows a greatly increased 2p density of states within 1.5 eV of the Fermi energy.

Bader charge analysis

Although unable to quantitatively determine oxidation states, Bader charge analysis is useful for examining trends in charge density behavior. Table 2.5 displays the Bader charge for the delithiated state and the change in Bader charge after delithiation. Previous *ab initio* work operated under the assumption that oxygen sites with the lowest Bader charge is the most likely to evolve, though under Mo-doping there exists a discrepancy between the lowest E^F_{Ov} site (oxygen site 13) and the site with the lowest charge and largest change (oxygen site 5). Analysis was performed using a grid-based method as described in reference [98].

Table 2. 5 Bader charge difference between lithiated and delithiated states for undoped and doped materials. Items in bold are sites exhibiting the lowest Bader charge and the largest change in Bader charge.

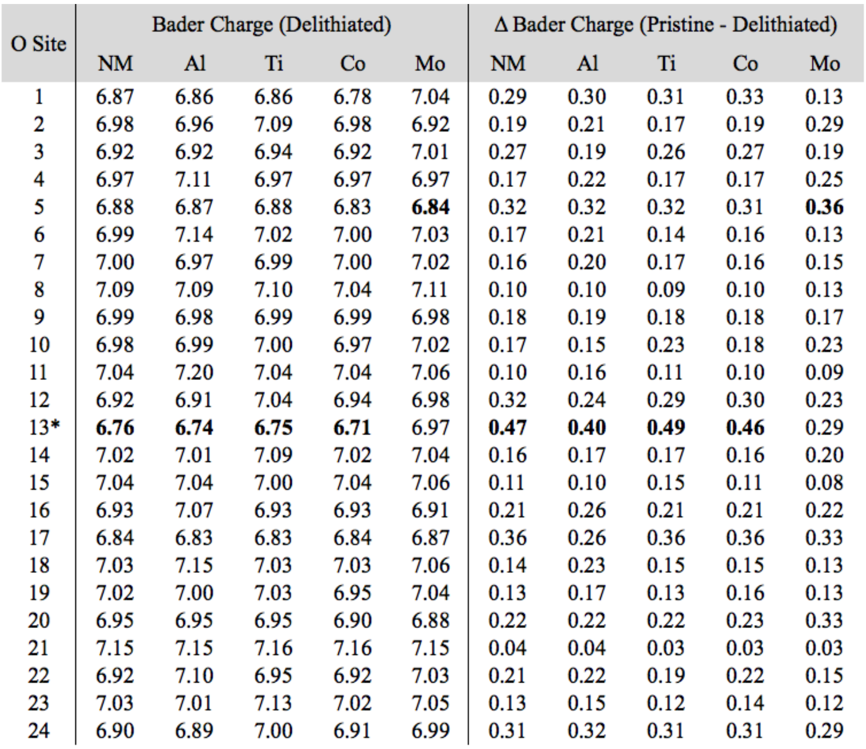

O Site	Bader Charge (Delithiated)					Δ Bader Charge (Pristine - Delithiated)				
	NM	Al	Ti	Co	Mo	NM	Al	Ti	Co	Mo
1	6.87	6.86	6.86	6.78	7.04	0.29	0.30	0.31	0.33	0.13
2	6.98	6.96	7.09	6.98	6.92	0.19	0.21	0.17	0.19	0.29
3	6.92	6.92	6.94	6.92	7.01	0.27	0.19	0.26	0.27	0.19
4	6.97	7.11	6.97	6.97	6.97	0.17	0.22	0.17	0.17	0.25
5	6.88	6.87	6.88	6.83	**6.84**	0.32	0.32	0.32	0.31	**0.36**
6	6.99	7.14	7.02	7.00	7.03	0.17	0.21	0.14	0.16	0.13
7	7.00	6.97	6.99	7.00	7.02	0.16	0.20	0.17	0.16	0.15
8	7.09	7.09	7.10	7.04	7.11	0.10	0.10	0.09	0.10	0.13
9	6.99	6.98	6.99	6.99	6.98	0.18	0.19	0.18	0.18	0.17
10	6.98	6.99	7.00	6.97	7.02	0.17	0.15	0.23	0.18	0.23
11	7.04	7.20	7.04	7.04	7.06	0.10	0.16	0.11	0.10	0.09
12	6.92	6.91	7.04	6.94	6.98	0.32	0.24	0.29	0.30	0.23
13*	**6.76**	**6.74**	**6.75**	**6.71**	6.97	**0.47**	**0.40**	**0.49**	**0.46**	0.29
14	7.02	7.01	7.09	7.02	7.04	0.16	0.17	0.17	0.16	0.20
15	7.04	7.04	7.00	7.04	7.06	0.11	0.10	0.15	0.11	0.08
16	6.93	7.07	6.93	6.93	6.91	0.21	0.26	0.21	0.21	0.22
17	6.84	6.83	6.83	6.84	6.87	0.36	0.26	0.36	0.36	0.33
18	7.03	7.15	7.03	7.03	7.06	0.14	0.23	0.15	0.15	0.13
19	7.02	7.00	7.03	6.95	7.04	0.13	0.17	0.13	0.16	0.13
20	6.95	6.95	6.95	6.90	6.88	0.22	0.22	0.22	0.23	0.33
21	7.15	7.15	7.16	7.16	7.15	0.04	0.04	0.03	0.03	0.03
22	6.92	7.10	6.95	6.92	7.03	0.21	0.22	0.19	0.22	0.15
23	7.03	7.01	7.13	7.02	7.05	0.13	0.15	0.12	0.14	0.12
24	6.90	6.89	7.00	6.91	6.99	0.31	0.32	0.31	0.31	0.29

Electrochemical Impedance Spectroscopy

Impedance measurement is conducted to investigate the influence of Mo doping on electrochemical behavior, including electronic conductivity and bulk ion diffusion. Before cycling, both LNMLO-Co and LNMLO-CoMo cells show relatively larger charge transfer impedance than that of after cycling, as a formation cycle is needed to reduce the overall resistance. It is clearly shows in Figure 2.11 that after Mo doping, the material exhibits much reduced impedance and improved ionic diffusion. Table 2.6 lists the quantitatively fitting results of both materials before and after cycling.

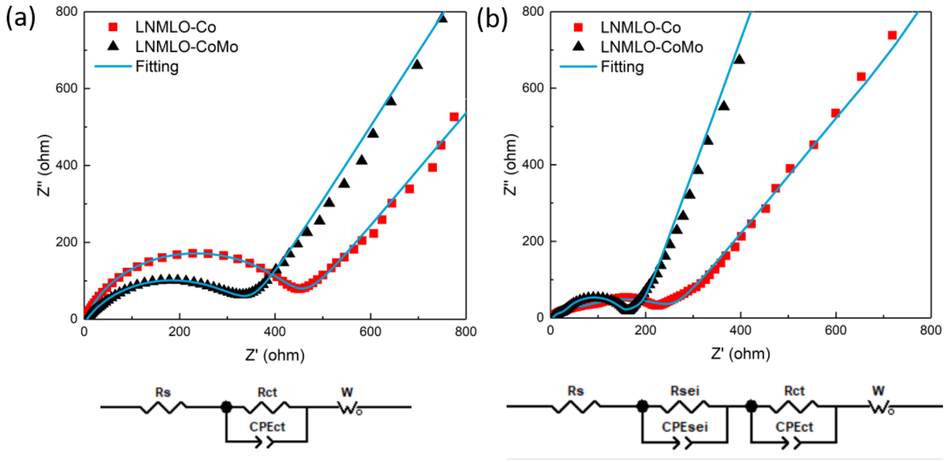

Figure 2. 11 Nyquist plots of LNMLO-Co and LNMLO-CoMo (a) at OCV and (b) after 30 cycle, and corresponding fitting circuits

Table 2. 6 EIS fitting results of LNMLO-Co and LNMLO-CoMo at OCV and after 30 cycle

	LNMLO-Co 0 cycle	LNMLO-CoMo 0 cycle	LNMLO-Co 30th cycle	LNMLO-CoMo 30th cycle
Rs (Ω)	3.662	5.787	4.584	4.965
Rsei (Ω)	--	--	44.52	24.72
Rct (Ω)	436.4	339.5	210.3	111

X-ray diffraction

To observe structural change and verify phase purity, X-ray diffraction and subsequent Rietveld refinement were performed on all samples studied in this work. The experimental observations of lattice parameters variation for LNMLO-Co, LNMLO-CoMo, LNMLO-Al, and LNMLO-Ti, match well with DFT calculation prediction, indicating all dopants have been successfully incorporated into the pristine NM structure. For Mo, 1% is the saturate point of doping according to previous study [82]. Consistently in the present work, 3% of doping shows impurity peaks.

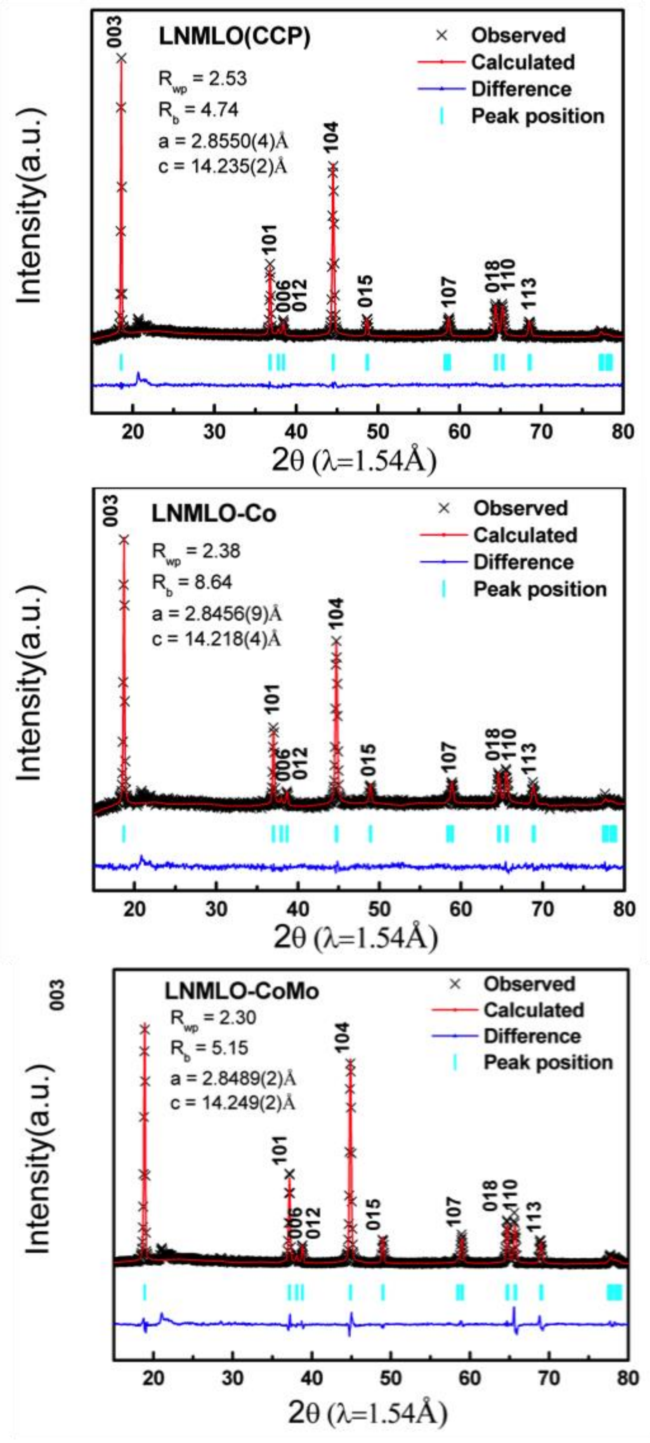

Figure 2. 12 X-ray diffraction and Rietveld refinement of LNMLO, LNMLO-Co, LNMLO-CoMo. As the ionic radius of Co^{3+} is smaller than Ni^{2+} and close to Mn^{4+}, NMC shows shrink lattice parameters. After 1% of Mo doping, both a- and c- of LNMLO-CoMo increase compared with LNMLO-Co, indicating Mo has been successfully doped into LNMLO-Co structure.

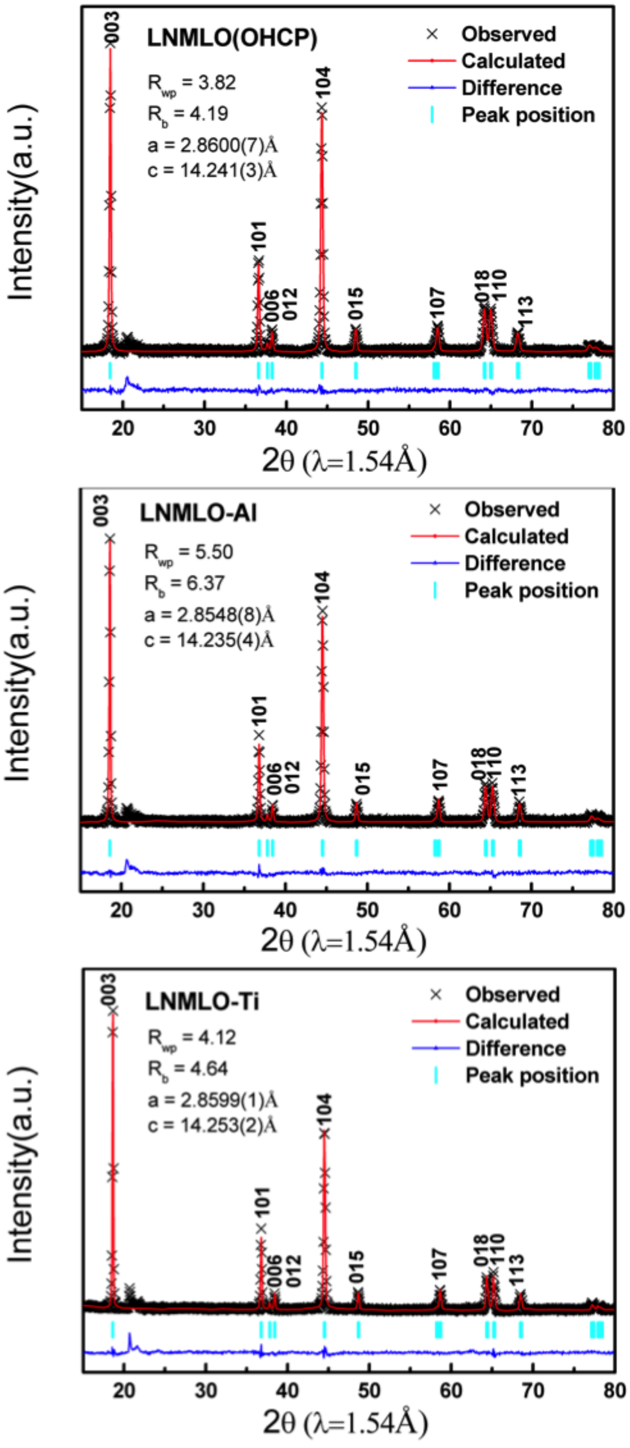

Figure 2. 13 X-ray diffraction and Rietveld refinement of LNMLO, LNMLO-Al, and LNMLO-Ti. LNMLO-Al shows decreased a- and c- lattice parameters due to the smaller ionic radius of Al^{3+}; LNMLO-Ti exhibits similar a-, but much higher c-, comparing with LNMLO.

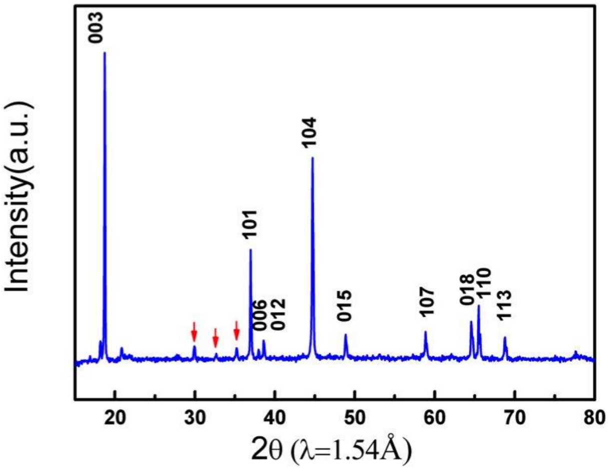

Figure 2. 14 3% Mo-doping shows the presence of impurity peaks in XRD.

Evidence of uniform doping distribution

To confirm the uniformity of Mo distribution, focused ion beam cross-sections of secondary particles was performed, allowing a clear view of the distribution of transition metal ions through profiles of the primary particles. Using energy dispersive x-ray spectroscopy, a uniform distribution of all TMs is observed, suggesting that the Mo dopant is uniformly distributed throughout the bulk of the material.

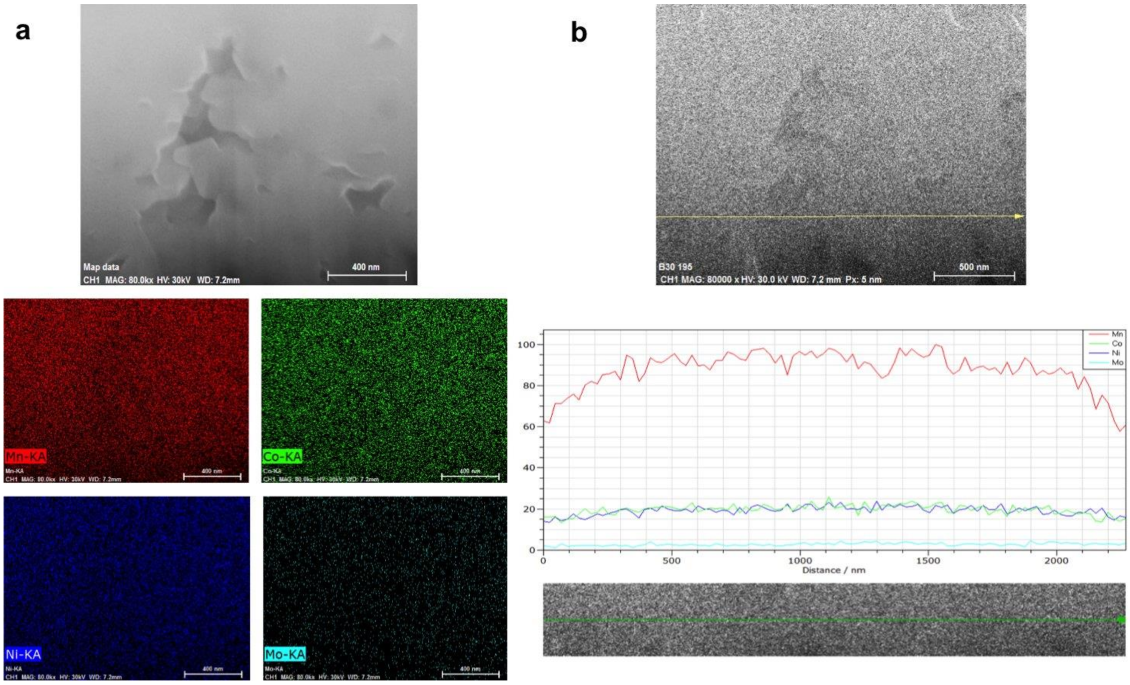

Figure 2. 15 Energy dispersive x-ray spectroscopy was performed on a focused ion beam cross-section of a secondary particle of the Mo-doped material. (a) The Mo map suggests that the Mo is evenly disbursed, further evidence of incorporation into the structure. (b) Similarly, a higher resolution line-scan shows no accumulation at primary particle boundaries and surfaces.

2.4 Conclusion

Oxygen vacancy formation energies, E_{Ov}^{F}, were calculated for a wide range of dopants using *ab initio* calculations. The range of calculated E_{Ov}^{F} were shown to be strongly dependent on local environment, both compositionally and structurally. The source of E_{Ov}^{F} change between dopants was attributed to the charge density modification and subsequent change in band structure, increasing the E_{Ov}^{F} in the case of a Mo dopant. These calculated E_{Ov}^{F} values guided experimental doping, showing results in line with computational prediction. Al- and Ti-doped materials showed little change to the initial charging plateaus, consistent with the predicted E_{Ov}^{F}, where Co-doping showed an increase in the plateau width, indicating exaggerated oxygen loss from the lattice. Mo-doping experiments shows improved cycling stability through reduced voltage decay, suggesting oxygen is stabilized by the incorporation of Mo. Experiments show the presence of a majority of Mo^{5+} ions, as predicted. When considering the nature of oxygen activity within cathode material, it is clear that the formation of molecular oxygen in the bulk of the material accounts for the majority of this irreversible capacity loss. As such, methods of mitigating must extend beyond surface modification. Calculation results show that doping of particular elements (Mo and Ru) work to reduce the degree of oxygen loss from the lattice, while leaving the oxygen available for redox. However, the degree of dopant incorporation is limited by solubility of the dopant in the structure. This work validates cationic substitution as a fundamental method of improving capacity retention of lithium rich layered oxide cathodes, and should be combined with advanced surface modification to result in improved high capacity cathodes. This work further demonstrates the application of density functional theory towards the rational design of cathode materials, streamlining the design process and speeding the optimization of these materials.

Chapter 2, in full, is a reprint of the material “Mitigating oxygen release in anionic-redox-active cathode materials by cationic substitution through rational design” as it appears in the Journal of Materials Chemistry A, Thomas A. Wynn*, **Chengcheng Fang***, Minghao Zhang, Haodong Liu, Daniel M. Davies, Xuefeng Wang, Derek Lau, Jungwoo Z. Lee, Bo-Yuan Huang, Kuan-Zong Fung, Chung-Ta Ni and Ying Shirley Meng, 2018, 6, 24651- 24659. The dissertation author was the co-primary investigator and author of this paper. All experiment parts and corresponding writing were performed by the author.

Chapter 3 Titration Gas Chromatography: A New Method for Inactive Lithium Quantification

3.1 Introduction

The formation of inactive Li, also known as “dead” Li, is the immediate cause of low CE, short cycle life and violent safety hazard of LMBs. It consists of both (electro)chemically formed Li^+ compounds in the solid electrolyte interphase (SEI) and the electrically isolated unreacted metallic Li^0 [99,100]. It is generally assumed that the low CE is dominated by the continuous repairing of SEI fracture that consumes both electrolyte and active Li metal[48], though a few works also suggested that unreacted metallic Li^0 may increase the tortuosity at the electrode/electrolyte interphase and decrease the CE[28,49]. Overall, most of these assumptions and hypothesis are observational, while the actual contribution to capacity loss from the SEI formation has never been quantified. Consequently, efforts may be misdirected as we search for solutions to the low CE. Differentiating and quantifying the Li^+ and Li^0 remaining on the electrode after stripping, therefore, becomes the key to understanding the mechanisms leading to capacity decay. But this is quite challenging due to the lack of proper characterization tools. Microscopy and other imaging tools, such as operando optical microscopy[12], *in-situ* environmental transmission electron microscopy (TEM)[29,101], X-ray microtomography[38] and magnetic resonance imaging (MRI)[40], have all been used to visualize the dynamic growth of Li dendrites, but most of them only provide morphological perspective with little chemical information. Nuclear magnetic resonance (NMR) utilized as a quantitative and operando tool revealed the Li microstructure formation with a resolution of tens of micrograms of Li, however the limited penetrating ability of radio frequency makes it only effective to quantify dendritic/mossy Li[46].

The X-ray photoelectron spectroscopy (XPS)[102] and cryogenic TEM[24,25] have the capability to distinguish between the Li^+ in SEI and metallic Li^0, but their detection ranges are limited to surfaces or local regions, which lack of both quantitative nature and global representation. It is thus of essential significance to develop a new set of experimental tools that both qualitatively profile the micro/nano-structures of inactive Li, and quantitatively differentiate the SEI Li^+ and metallic Li^0.

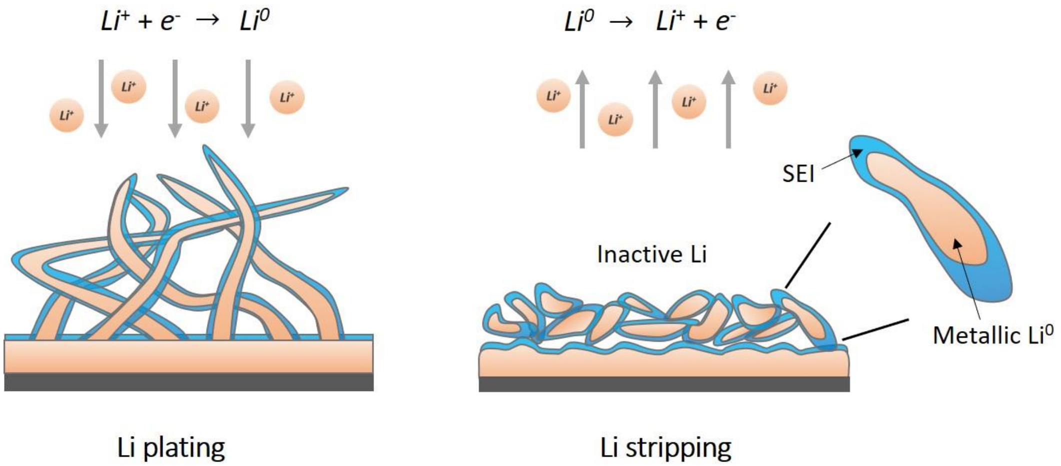

Figure 3. 1 Schematic illustration of the electrochemical reactions of Li plating/stripping, dendrite formation and inactive Li formation. In a Li metal battery, during the plating, Li^+ deposits on the fresh Li. In commercial carbonate-based electrolytes, Li deposits exhibit whisker-like morphology. During stripping, Li dissolves into the electrolyte becoming Li^+. If the dissolution occurs firstly on the roots of the Li whiskers, the top parts will disconnect from the electronic conductive network and thus become electrochemically inactive, forming inactive Li, which consist of SEI and unreacted metallic Li wrapped by the insulating SEI.

3.2 Titration Gas Chromatography (TGC) Method

3.2.1 TGC concept

Inactive Li consists of diverse Li^+ compounds within the SEI, such as LiF, Li_2CO_3, Li_2O, $ROCO_2Li$[16,103], and of unreacted metallic Li^0 which is isolated by SEI from the electronic conductive pathway. The pivotal difference between the SEI Li^+ and metallic Li^0 that inspired us is their chemical reactivity: only the metallic Li^0 reacts with protic solvents (e.g. H_2O) and generates hydrogen gas (H_2). The solubility/reactivity of known SEI species with H_2O are listed in Table 3.1. Noting that the possible LiH-existence[26,104,105] in inactive Li might affect the metallic Li^0 quantification because LiH also reacts with water and produces H_2, the exclusion of LiH in the present study is critical, which will be detailed later. Therefore, we combine H_2O titration (the step to react all metallic Li^0) and gas chromatography (the following step to quantify the H_2 generated in the reaction) into a single analytic tool, hereafter referred to as TGC (schematic process in Figure 3.2), which is able to quantify the content of metallic Li^0 based on the following reaction:

$$2Li + 2H_2O \rightarrow 2LiOH + H_2 \uparrow .$$

Coupling with an advanced barrier ionization H_2 detector (BID), the measurement accuracy for metallic Li^0 in the designed system is as low as 10^{-7} g.

Table 3. 1 The solubility/reactivity of known SEI species with H_2O

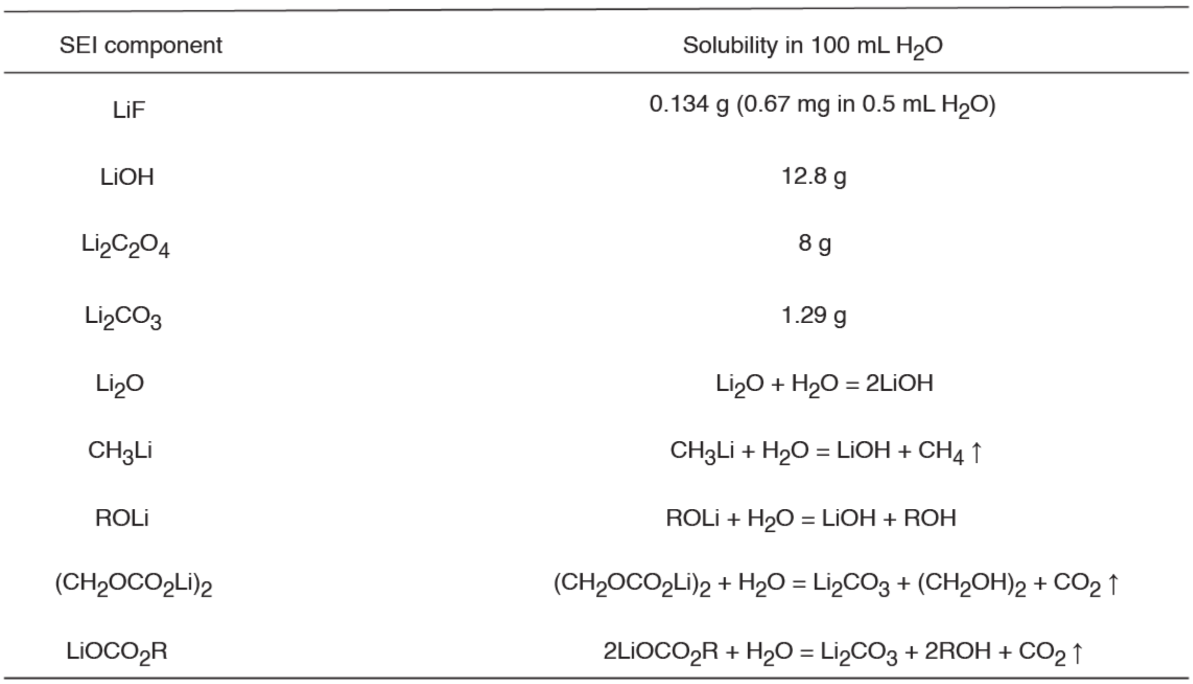

SEI component	Solubility in 100 mL H_2O
LiF	0.134 g (0.67 mg in 0.5 mL H_2O)
LiOH	12.8 g
$Li_2C_2O_4$	8 g
Li_2CO_3	1.29 g
Li_2O	$Li_2O + H_2O = 2LiOH$
CH_3Li	$CH_3Li + H_2O = LiOH + CH_4 \uparrow$
ROLi	$ROLi + H_2O = LiOH + ROH$
$(CH_2OCO_2Li)_2$	$(CH_2OCO_2Li)_2 + H_2O = Li_2CO_3 + (CH_2OH)_2 + CO_2 \uparrow$
$LiOCO_2R$	$2LiOCO_2R + H_2O = Li_2CO_3 + 2ROH + CO_2 \uparrow$

Figure 3.2 demonstrates the typical processes of the TGC method for the inactive Li quantification, including the following six main steps. (1) After plating and stripping, the Li||Cu coin cell was disassembled in an Ar-filled glovebox. (2) Both the Cu foil and separator on the Cu foil side were harvested without washing and sealed into a container by a rubber septum which is stable against water with an inside pressure of one atmosphere in the glovebox. (3) After transferring the sample container outside of the glovebox, 0.5 mL of H_2O was injected into the container to react with the inactive Li completely. (4) 30 µL of the resultant gas was taken from the container into the GC system by a gas-tight syringe. (5) The H_2 amount was measured by the GC. (6) The content of the metallic Li^0 was determined by converting the corresponding H_2 amount

based on a pre-established standard calibration curve. All the processes minimize the potential damage and contamination during sample transfer, guaranteeing trustworthy and accurate results.

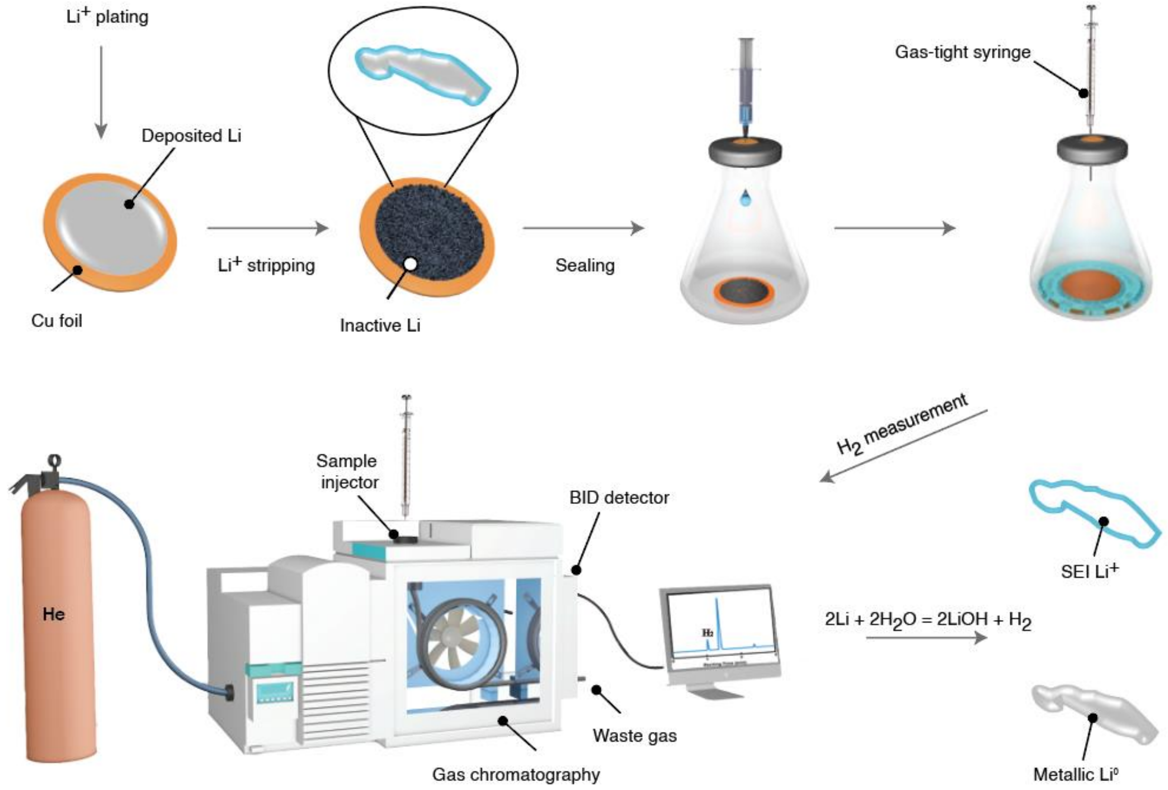

Figure 3. 2 Schematic working principle of the TGC method. Combing H_2O titration on inactive Li sample and H_2 quantification by GC, metallic Li^0 amount is determined based on the chemical reaction $2Li + 2H_2O \rightarrow 2LiOH + H_2\uparrow$.

In the GC column, the stationary phase has a different affinity with different species, so that gas species can be differentiated by retention time. Figure 3.3a shows the GC chromatograms of background gases from an empty container well sealed in the Ar-filled glovebox. The peaks at 1.45 min, 2.42 min, and 3.21 min represent Ar, N_2 and CH_4, respectively. When a H_2O titration process is applied on a small piece of pure Li metal, H_2 will be generated. The H_2 characteristic peak appears at 1.05 min, as shown in Figure 3.3b

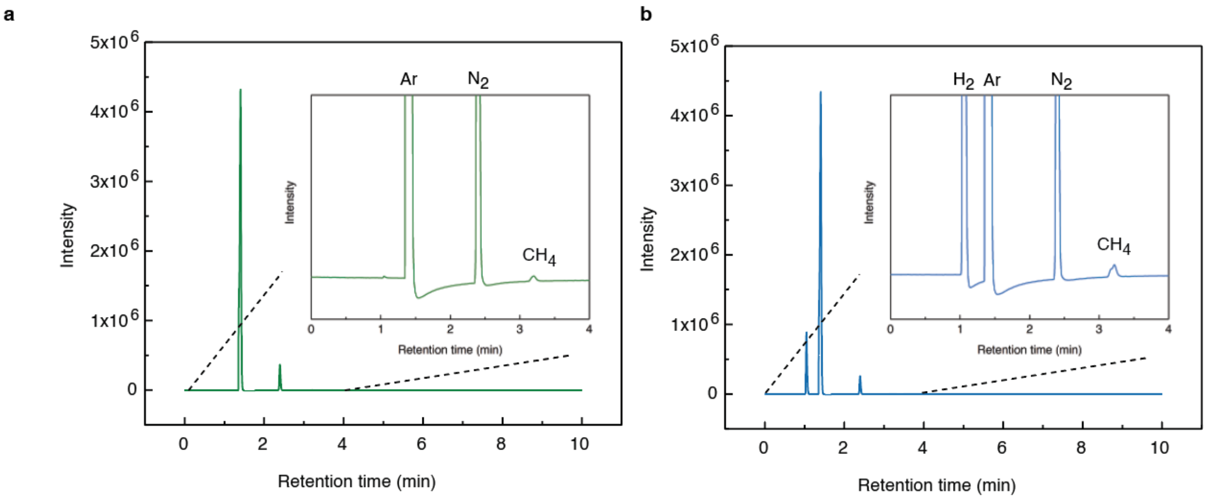

Figure 3. 3 Examples of GC chromatograms. (**a**) Blank control group. The background gas from glovebox. (**b**) Gases with H_2 after H_2O titration on metallic Li.

3.2.2 Calibration

The H_2 concentration was calibrated and measured using Shimadzu GC-2010 Plus Tracera equipped with a Barrier Ionization Discharge (BID) detector. 99.9999% Helium was used as the carrier gas. Split temperature was kept at 200 °C with a split ratio of 2.5 (split vent flow: 20.58 mL/min, column gas flow: 8.22 mL/min, purge flow: 0.5 mL/min). Column (0.53mm, RT- msieve 5A) temperature was kept at 40 °C. A BID detector was kept at 235 °C, and BID detector gas flow rate was 50 mL/min. All calibration and sample gases were immediately collected via a 50 μL Gas-Tight Hamilton syringe before injection. For calibration of H_2 concentration, 1500 ppm of H_2 gas was produced by reacting high purity of Sodium with DI water in a septum sealed glass vial. 5, 10, 15, 20, 25 and 30 μL of produced H_2 gas corresponding to 250, 500, 750, 1000, 1250 and 1500 ppm, respectively, were collected and injected into the GC. The calibration curve was plotted and fitted with H_2 concentration versus GC measured H_2 peak area. The as-established H_2 calibration curve ($H_{2,\,ppm}$ – *detected* H_2 *area*) and equation are shown in Figure 3.4a. In order to acquire the exact number of H_2 molecules within the container, the H_2 concentration calibration curve was converted to the mole number of H_2 calibration curve as a function of detected area based on the following two conditions:

(1) 1 ppm = 4.08×10^{-8} mmol/mL (1 atm, 298 K);

(2) Container volume (30 ± 0.5 mL).

The mole number of H_2 calibration curve directly established a relationship between GC software reported H_2 area and the number of H_2 molecules in the fixed TGC set-up, making the following inactive Li measurement independent from slight pressure change in virtue of a Gas-Tight syringe. Based on the chemical reaction $2Li + 2H_2O \rightarrow 2LiOH + H_2\uparrow$, the standard calibration curve and the equation for Li metal mass as a function of the detected H_2 area (m_{Li} - *detected* H_2 *area*) are obtained and shown in Figure 3.4b.

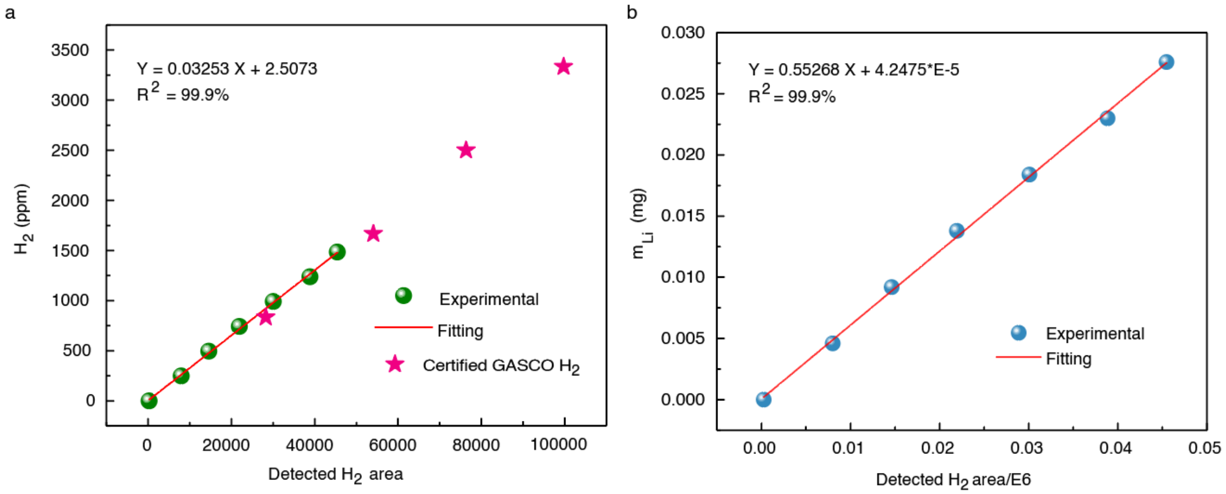

Figure 3. 4 (a) Original H_2 concentration calibration curve as a function of detected H_2 area ($H_{2,\,ppm}$ – *detected* H_2 *area*) and verification with certified GSCO H_2 calibration gas. (b) Converted metallic Li^0 weight calibration curve as a function of detected area (m_{Li} - *detected* H_2 *area*).

3.2.3 Validation of TGC method

(1) The H_2 concentration in ppm as a function of GC detected H_2 area (*$H_{2,\,ppm}$ – detected H_2 area*, Figure 3.4a) has been verified by the certified GASCO H_2 Calibration Test Gas.

(2) We then used the commercial Li metal with known weight to verify the as-established *m_{Li} - detected H_2 area* relationship (Figure 3.4b). We carefully weighted 9 pieces of commercial Li metal with mass ranging from 0.54 to 1.53 mg in the Ar-filled glovebox by a 5-digit balance (10^{-5} g) and then performed the TGC. The detected H_2 area as a function of the Li metal weight from the 9 pieces of Li metal is shown in Figure 3.5a. The result shows that the mass of Li metal is linearly related to (R^2 = 99.8%) the detected H_2 area, indicating the validity of the TGC system for quantifying metallic Li^0. In reverse, we calculated the Li metal weight from the detected H_2 area using the *m_{Li} - detected H_2 area* relationship. The TGC measured Li metal weights and balance measured Li metal weights are compared in the Figure 3.5b. The exact numbers of TGC measured Li metal weights and balance measured Li metal weights are listed in the Figure 3.5c. The negligible differences between the TGC quantification and balance measurement indicate the validity and accuracy of the TGC method. Noting that the significant digit of the balance is 0.01 mg (10^{-5} g), as marked in red in Figure 3.5c, whereas the TGC is 0.0001 mg (0.1 µg, 10^{-7} g), which has been demonstrated in the limit of detection/limit of quantification (LOD/LOQ) analysis. The minimal difference between the two quantification methods is mainly ascribed to the inaccuracy of the balance, of which the precision is two orders of magnitude smaller than the TGC.

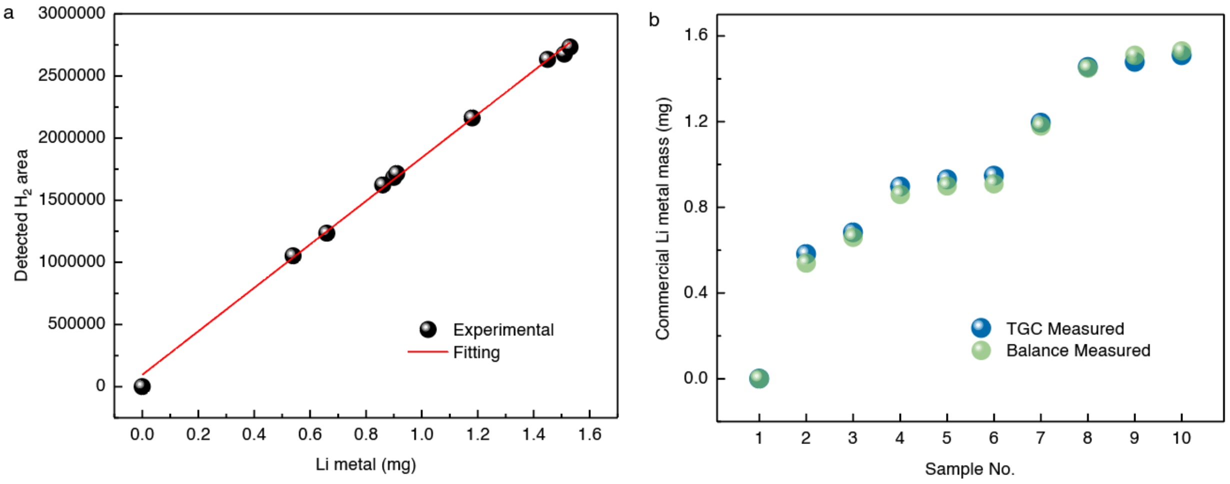

c

Li, mg	1	2	3	4	5	6	7	8	9	10
TGC	0.0005	0.5820	0.6825	0.8970	0.9304	0.9472	1.1943	1.4550	1.4781	1.5098
Balance	Blank	0.54	0.66	0.86	0.90	0.91	1.18	1.45	1.51	1.53

Figure 3. 5 (a) Nine pieces of Li metal with known weight were tested using TGC set-up. The great linear relationship versus detected H_2 area indicates the feasibility of this method. (b) A comparison between the balance weighed mass and TGC quantified mass of the commercial Li metal pieces. Since the accuracy of the balance is two orders of magnitude lower than the TGC (10^{-5} vs 10^{-7} g), the differentials should mainly come from the balance. (c) The numeric comparison between the balance weighted mass and TGC quantified mass of the commercial Li metal pieces.

3.2.4 The possible existence of LiH

Besides the SEI species listed in Table 3.1, there have been mixed reports regarding the existence of LiH in Li metal electrode[26,104,105]. There are two possible scenarios that LiH may exist in the Li metal electrodes: 1. LiH in SEI as an electrochemical reduction product at excessively negative potentials[104,105]; 2. LiH may largely exist in bulk electrode as another type of mossy dendrite[26]. To examine the possible influence from LiH in SEI, we repeatedly polarized the current collectors above 0 V, so that only SEI forms without metallic Li^0 deposition[106]. For the electrolytes investigated in this work, after such cyclic polarizations between 0-1V for ten cycles, the TGC detects no H_2 from all SEI-water reactions (Figure 3.6a-h), indicating that LiH does not exist in the SEIs.

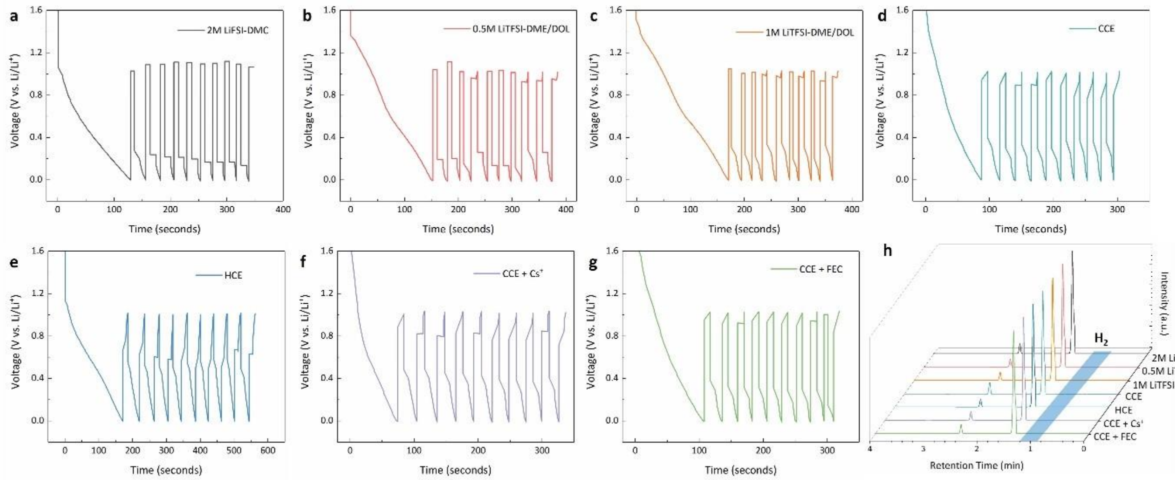

Figure 3. 6 TGC characterization of SEIs formed by plating/stripping Li above 0V. By plating/stripping Li above 0 V, only SEI without metallic Li^0 will be formed on the current collector. **(a)** – **(g)** show the voltage profiles of SEI formation between 0-1V at 0.1 mA for ten cycles in (a) 2M LiFSI-DMC, (b) 0.5M LiTFSI-DME/DOL, (c) 1M LiTFSI-DME/DOL, (d) CCE, (e) HCE, (f) CCE+Cs^+, and (g) CCE+FEC, respectively. After the SEI formations, current collectors with SEI on top were performed TGC measurement. **(h)** shows the TGC results of the seven types of electrolytes. No H_2 can be detected from any of them, indicating no LiH presence in the as-studied systems.

To examine the possible influence from LiH in bulk inactive Li, we changed the titration solution from H_2O to D_2O, which can distinguish LiH and metallic Li^0 by producing HD and D_2, respectively, based on the reactions: 1. $LiH + D_2O = LiOD + HD\uparrow$; 2. $2Li + 2D_2O = 2LiOD + D_2\uparrow$. Differentiating HD and D_2 was then achieved based on partial pressure analysis by the Residual Gas Analyzer (RGA)[107], as demonstrated in Figure 3.7. The base pressure in the vacuum chamber is ~8×10^{-8} torr. The gas mixtures were introduced into the chamber using an MKS pressure/flow control valve controlled by a computer. The partial pressures of gases in the system were measured using an SRS RGA with a detection limit down to 10-11 torr. The turbo pump and backing pump used in this vacuum system were specially designed for handling highly corrosive gases. This setup can provide a wide-range partial pressure control (10^{-11} torr to 10^{-4} torr) and allow for the identification of the different gas molecules including hydrogen isotopes present in the system under high vacuum conditions. Before measuring each sample, the whole system was pumped down to high vacuum to ensure the possibility of contamination is minimized.

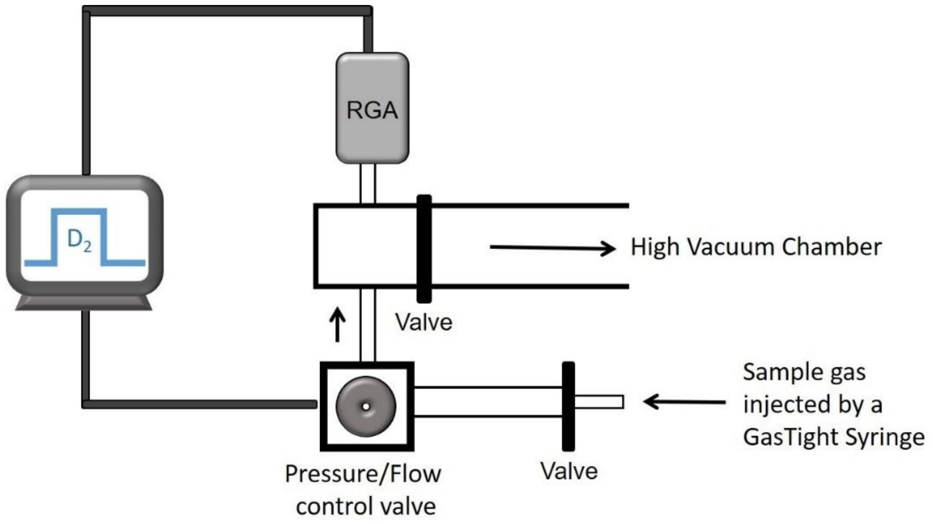

Figure 3. 7 Schematic of the RGA setup for partial pressure analysis to differentiate HD/D_2 isotopes, which are generated from the reaction from LiH and Li metal with D_2O, respectively.

Based on the RGA results (Figure 3.8), we confirmed that LiH does not exist in the bulk inactive Li generated by the electrolyte systems of low CE. The exclusion of LiH from either SEI or bulk inactive Li confirms that the conclusion that is drawn from the TGC analysis should be reliable and free of interference from possible LiH species.

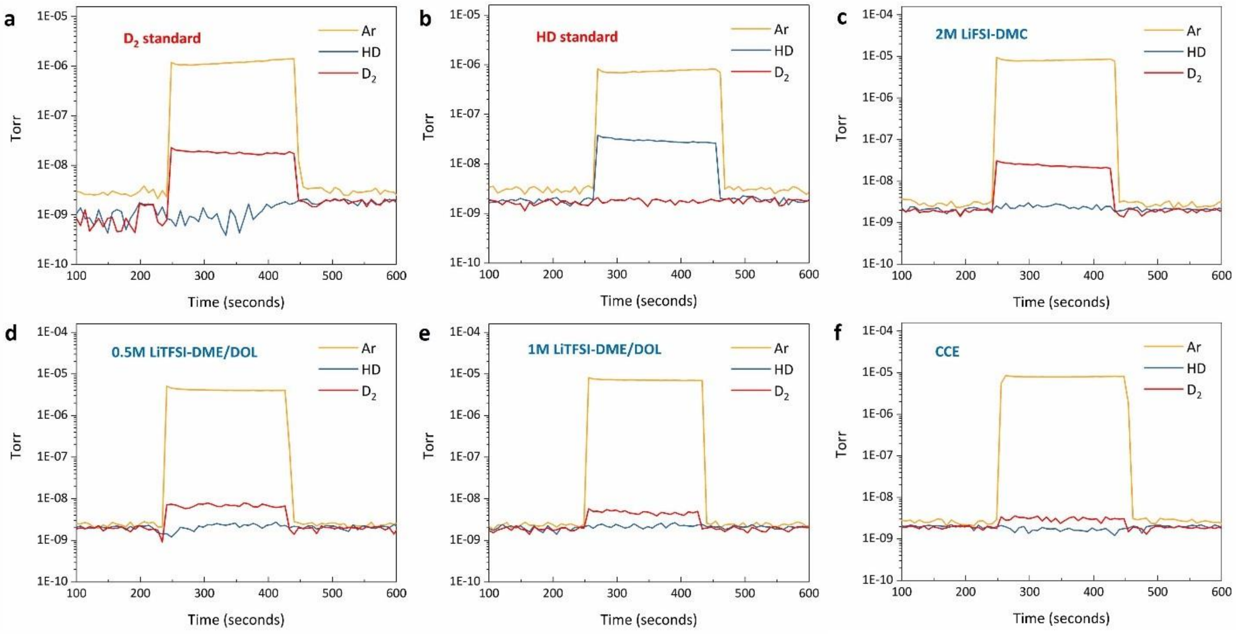

Figure 3. 8 The study of potential LiH presence in bulk inactive Li. Both metallic Li^0 and LiH react with H_2O and generate H_2. To differentiate the two species, we substitute the titration solution from H_2O to D_2O, which reacts with LiH and metallic Li^0 to produce HD and D_2, respectively, based on the reactions: 1. LiH + D_2O = LiOD + HD↑; 2. 2Li + $2D_2O$ = 2LiOD + D_2↑. Residual Gas Analyzer (RGA) can effectively distinguish HD (molecular weight is 3) and D_2 (molecular weight is 4) by partial pressure analysis. **(a)** the D_2 standard that comes from the reaction between ~1 mg of commercial pure Li metal and D_2O. **(b)** the HD standard comes from the reaction between ~1 mg of commercial LiH powder and D_2O. The gaseous products analysis from reactions between D_2O and inactive Li forming in **(c)** 2M LiFSI-DMC, **(d)** 0.5M LiTFSI-DME/DOL, **(e)** 1M LiTFSI-DME/DOL, and **(f)** CCE, respectively. Within the detection limit of RGA, the results indicate LiH does not exist in the bulk inactive Li in the as-studied electrolyte systems, confirming the accuracy on metallic Li^0 quantification by TGC.

3.2.5 The source of nitrogen in GC chromatograms

Note that N_2 detected from the GC comes from the GC gas sampling process, instead of existing in the reaction container. As schematized in the TGC process in Figure 3.2, the inactive Li samples were loaded and sealed into the reaction container in an Ar-filled and N_2-free glovebox. After being taken out from the glovebox, 0.5 mL of pure H_2O was injected into the container and reacted with the inactive Li sample. This is an air-free process. A gas-tight syringe was then used to take the gas sample for GC injection and measurement. There is a small amount of air left in the needle space of the gas-tight syringe. Moreover, in the GC injection process, when the needle breaks the septum, a tiny amount of air might be brought into the GC column. Even though the air peak is inevitable for the injection gas sampling method, the inactive Li samples indeed have all been reacted in advance and were never exposed to N_2.

To prove that the N_2 comes from air during sampling and the presence of air has negligible impact on the inactive Li (H_2) quantification. First, we measured the gas in the blank container without any inactive Li, which has been well sealed in the Ar-filled glovebox. If the N_2 comes from the reaction container, the N_2 peaks intensity will vary proportionally to the injected gas amount into the GC. We took different amounts of gas sample from the blank container and performed GC measurement. As shown in Figure 3.9a, the N_2 peak intensities keep almost identical with injection amounts varied from 5-30 µL. The same result was obtained when H_2O titration on inactive Li was performed. The measured H_2 content increase as a function of injected gas amount while the N_2 content keeps almost constant (Figure 3.9b). Noting that the reaction container is sealed in the Ar-filled glovebox, the Ar peak is saturated even only 5 µL of sample gas is injected and keeps unchanged in all measurements. The invariability of N_2 peaks is not because of saturation in the previous measurements since the intensity of the N_2 peak increases significantly after purposely injecting 10 µL of air (Figure 3.9c). Therefore, we confirmed that the N_2 comes from the injection sampling process which will not have any chemical reactions with the inactive Li samples. Moreover, the H_2 quantification is not influenced by the injection sampling process.

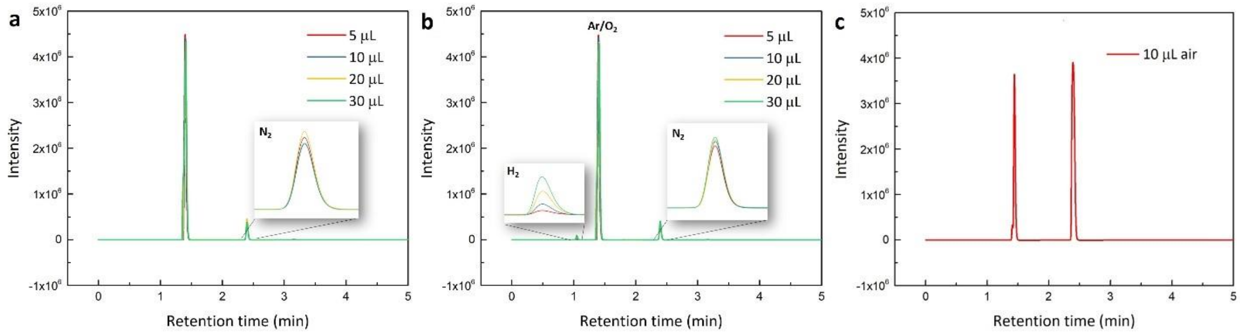

Figure 3. 9 Experimental evidences to show that N_2 comes from the sampling process, by using different gas injection amounts. (**a**) **Glovebox background gas measurement**. The N_2 amounts keep the same level with variety of injection amounts, indicating the N_2 does not exist in the container; (**b**) **Container gas measurement after the H_2O titration**. The N_2 amounts still keep identical with different injection amounts, whereas the H_2 amounts proportionally increase along with the increment of injection amounts, indicating that the N_2 comes from the injection sampling process thus will not have any chemical reactions with the inactive Li samples; the H_2 quantification is not influenced by the injection sampling process; (**c**) **Air sample.** 10 µL of air was directly injected into the GC in order to demonstrate that the invariant of N_2 peaks in Fig. a and b are not due to the N_2 measurement saturation.

3.2.6 LOD/LOQ analysis of TGC method

The concentration of hydrogen in the air is 0.000053 %. In order to get the LOD/LOQ values, 30 µL of the air sample was injected into GC by the same gas-tight syringe for the hydrogen measurement and repeated for 10 times. The results are listed in Table 3.3. Based on the definition of LOD/LOQ, the calculated LOD/LOQ from the table is 16.44 ppm and 49.81 ppm, respectively, corresponding to 0.28 µg and 0.84 µg of metallic Li^0 in the designed TGC system.

Table 3. 2 The hydrogen concentration in the blank samples measured for LOD/LOQ analysis. Total 10 measurements for the LOD/LOQ calculation.

Blank Sample Trial No.	H_2 Concentration in ppm
1	47.20
2	58.27
3	54.39
4	41.07
5	46.54
6	51.02
7	51.03
8	54.65
9	45.49
10	53.98

3.2.7 Inactive lithium sample preparation (Electrochemical testing) for TGC measurement

Coulombic efficiency was measured in Li||Cu coin cells: Li metal (1 mm thick, 1/2’), two pieces of separators (Celgard) and Cu foil (1/2’) were sandwiched in CR2032 coin cells with a spacer and a spring, and crimped inside an Ar-filled glovebox. 50 µL of the electrolyte was added in each cell. Composition of HCE is 4M LiFSI (lithium bis(fluoro sulphonyl)imide, battery grade, Oakwook Products, Inc.) + 2M LiTFSI (lithium bis(trifluoromethane sulphonyl)imide, battery grade, Solvay) in DME (1,2-dimethoxyethane, anhydrous, >99.5%, BASF). CCE consists of 1M $LiPF_6$ (lithium hexafluorophosphate, battery grade, BASF) in EC/EMC (ethylene carbonate/ethyl methyl carbonate, battery grade, BASF) (3:7 by weight) with 2 wt% of VC (vinylene carbonate, battery grade, BASF). CCE + Cs^+ contains 50 mM of $CsPF_6$ (cesium hexafluorophosphate, Synquest Lab). CCE + FEC contains 10 wt% of FEC (fluoroethylene carbonate, anhydrous, >99%, Sigma-Aldrich). DOL (1,3-dioxolane, anhydrous, >99.5%) and $LiNO_3$ were purchased from Sigma-Aldrich. Cells for TGC are plating at 0.5 mA cm^{-2} for 1mAh cm^{-2} and stripping at various rates (0.5, 2.5 and 5 mA cm^{-2}) to 1 V, or unless otherwise specified.

3.2.8 Inactive lithium sample measurement by TGC method

Li||Cu cells after stripping at various conditions were disassembled inside Ar-filled glovebox (H_2O < 0.5 ppm). The Cu foil and separator near the Cu foil side with inactive Li residue on top were placed into a 30 mL container without washing. The container was sealed by a rubber septum and further capped by a stainless-steel/copper ring for safety concern and to minimize the deformation of the rubber septum when gas was generated later. The internal pressure of the sealed container was adjusted to one atmosphere by connecting the container and glovebox environment (0 mbar) with an open-ended syringe needle. After transferring the sealed container out of the glovebox, 0.5 mL of water was injected into the container, allowing complete reaction of inactive Li residue with water. Excess amount of H_2O has been added to react with all the inactive metallic Li^0, leading to a complete conversion to the H_2 products. The Cu foil became shiny and the separator normally turned clean when reactions finished, indicating a complete reaction of the inactive Li with H_2O. The as-generated gases were then well dispersed and mixed by shaking up the container to prevent H_2 accumulation on top of the container. Then a gas-tight syringe is used to quickly take 30 µL of the well-mixed gas and to inject it into GC for H_2 measurement. The GC measured H_2 areas as a function of cell CE are shown in Figure 3.10a. The conversion between mAh and mg of Li is shown in Figure 3.10b.

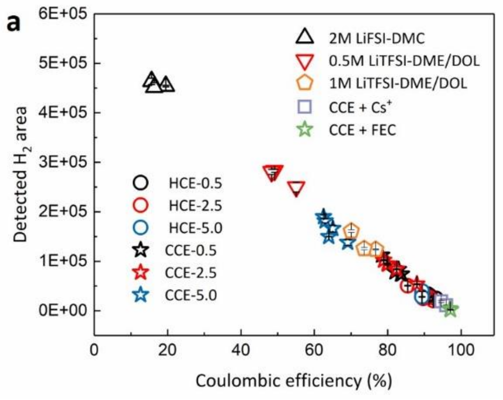

b

$$1\,C = 1\,A * s = 1000\,mA * \frac{1}{3600}h = \frac{1}{3.6}\,mAh$$

$$1\,C = 6.25 * 10^{18}\,e^{-} = 1.038 * 10^{-5}\,mol\,e^{-}$$

$$Li^{+} + e^{-} = Li$$

$$1\,mAh = 3.7368 * 10^{-5}\,mol\,Li = 0.2594\,mg\,Li$$

Figure 3. 10 (**a**) Directly measured H_2 area as a function of Coulombic efficiency under variety of testing conditions. Every data point is an average of three separate measurements. The small error bars indicate the accuracy and reproducibility of the GC measurement. (**b**) Units conversion between mAh and mg of Li

3.2.9 Safety considerations of TGC method

Li is electrochemically inactive, but chemically hyperactive due to the high surface areas which may lead to serious potential safety hazards[108]. The operation of inactive Li quantification using the TGC method should be very careful, taking the following aspects into consideration:

1. The proper amount of inactive Li for TGC measurement. The minimum amount of inactive metallic Li has been measured is as low as 1 µg (~ 0.04 mAh). The maximum amount of Li metal that has been measured in present work is ~ 1.6 mg, corresponding to ~ 6 mAh. It is generally preferred to reduce the amount of inactive Li sample, since the GC with an advanced H_2 detector can be very sensitive (1 ppm). The larger amount of H_2 generated, the more dangerous could be.
2. Reaction container must be completely sealed inside the Ar-filled glovebox before taking out, to avoid O_2 and moisture entering the reaction container. While moisture in air

influences the measurement accuracy, O_2 may lead to an explosion when a large amount of water reacts with inactive Li.

3. Stainless steel/copper rings are utilized to minimize the rubber septum deformation when H_2 generated inside the reaction container after water titration, and to prevent potential explosion due to the increased internal pressure.
4. Waste gas in the container after TGC measurement should be disposed in a fume hood to avoid regional H_2 accumulation which can lead to an explosion (explosive limits of H_2 in air range from about 18 - 60%, the flammable limits are from 4 - 75%).

Chapter 3 and Chapter 4, in full, is a reprint of the material “Quantifying inactive lithium in lithium metal batteries” as it appears in the Nature, **Chengcheng Fang***, Jinxing Li*, Minghao Zhang, Yihui Zhang, Fan Yang, Jungwoo Z. Lee, Min-Han Lee, Judith Alvarado, Marshall A. Schroeder, Yangyuchen Yang, Bingyu Lu, Nicholas Williams, Miguel Ceja, Li Yang, Mei Cai, Jing Gu, Kang Xu, Xuefeng Wang and Ying Shirley Meng, 2019, 572, 511-515. The dissertation author was the co-primary investigator and author of this paper. The author conducted all the experiment and data analysis except for the TEM data collection, and cowrote the paper.

Chapter 4 Quantifying Inactive Lithium in Lithium Metal Batteries

4.1 Introduction

To achieve the energy density of 500 Wh/kg or higher in the next-generation battery technologies, Li metal is the ultimate anode of choice, because it is the lightest metal known (0.534 g cm^{-3}), delivers ultra-high theoretical capacity (3860 mAh g^{-1}), and has the lowest negative electrochemical potential (-3.04 V *vs.* SHE)[9]. Yet, Li metal suffers from dendrite growth and low Coulombic efficiency (CE), which have prevented the extensive adoption of Li metal batteries (LMBs)[14,15,109]. Since the first demonstration of a Li metal battery in 1976[8], tremendous effort has been made in preventing dendritic Li growth and improving CE, including electrolyte engineering[23,110–112], interface protection[113] and substrate architecture[114]. While densely deposited Li can be achieved without any dendrites during the plating process, the stripping process will eventually dominate the CE and thus the reversibility of Li metal anode.

Here we combine multiscale characterization techniques to achieve this goal. A new analytic method, Titration Gas Chromatography (TGC), is established to accurately determine the quantity of isolated metallic Li^0 content in inactive Li down to microgram (μg). Advanced cryogenic FIB-SEM and TEM are used to probe the microstructure and nanostructure of inactive Li in both SEI components and the isolated metallic form, providing crucial complimentary information on nanoscale. The effectiveness of such multiscale methodology can be fully demonstrated when compared with different characterization tools (Table 4.1). Combining the advanced electron microscopies with the newly developed TGC allows an unprecedentedly precise profiling of inactive Li with atomic level resolution, nanoscale morphology, and most importantly, composition quantification. Based on these results, we propose the formation mechanism of high-confidence for inactive Li as well as strategies to mitigate it for high CE.

Table 4. 1 The capability of characterization tools which can be utilized for inactive Li study. The green color indicates the methods used in the present study.

Characterization Tools	Resolution	Morphology	Chemical Info.	Inactive Li Quantification
Cryo TEM	Atomic	**Y**	**Y**	N
Ex-situ SEM	nm - µm	**Y**	N	N
XPS	nm (surface)	N	**Y**	Semi; Surface only
TGC	0.1 µg (Li)	N	**Y**	**Y**
In-situ TEM	nm	Y	Y	N
In-situ SEM	µm	Y	N	N
AFM	nm	Y; Surface only	Y	N
Optical Microscopy	µm	Y	N	N
X-ray Microtomography	µm	Y	Y	Y; Low resolution
MRI	mm	Y	Y	N
NMR	tens of µg (Li)	N	Y	Y; Dendritic Li only

4.2 Quantifying inactive lithium under variety of conditions by TGC

We then applied TGC to correlate the origin of inactive Li with the CE in Li||Cu half cells. Noting that the CE of Li metal profoundly vary with electrolyte properties and current density, two representative electrolytes, the high-concentration electrolyte (HCE, 4M LiFSI + 2M LiTFSI in DME)[115] and commercial carbonate electrolyte (CCE, 1M $LiPF_6$ in EC/EMC), were compared at three stripping rates (0.5, 2.5 and 5.0 mA cm^{-2}, all plating at 0.5 mA cm^{-2} for 1 mAh cm^{-2}). In addition, we also examined six other electrolytes with a variety of salts, solvents and additives that frequently appear in literature, including 2M LiFSI-DMC, 0.5M LiTFSI-DME/DOL, 1M LiTFSI-DME/DOL, 1M LiTFSI-DME/DOL+2% $LiNO_3$, CCE + Cs^+ and CCE + FEC. Figure 4.1a shows that their first-cycle average CE exhibit a broad range of values from 17.2% to 97.1%. Their representative voltage profiles are shown in Figure 4.2a and b. The total amount of inactive Li is equal to the capacity loss between the plating and stripping processes, displaying a linear relationship with CE (Figure 4.1d). The content of the metallic Li^0 was directly measured by the TGC method. Once the amount of unreacted metallic Li^0 is determined, the SEI Li^+ amount can be calculated since total amount of inactive Li (known) = unreacted metallic Li^0 (measured) + SEI Li^+. The average capacity utilization under all conditions were quantified by the TGC, as summarized in Figure 4.1b. The reversible capacity indubitably increases with the increment of CE. Interestingly, the unreacted metallic Li^0 amount increases significantly with the decrease of CE, whereas the SEI Li^+ amount remains at a constantly low level under all testing conditions. Further analyzing the amount of unreacted metallic Li^0 as a function of CE (Figure 4.1e), we found to our surprise that the amount of unreacted metallic Li^0 exhibits a linear relationship with loss of CE, and such relationship is almost independent from the testing conditions. This implies that the

CE loss is governed by the formation of unreacted metallic Li^0. Meanwhile, the SEI Li$^+$ amount (Figure 4.1f) as deducted from above remains low and relatively constant under various stripping rates. The ratio of SEI Li$^+$ and unreacted metallic Li^0 (Li$^+$/Li^0) under various conditions (Figure 4.1c) clearly reveals that the unreacted metallic Li^0 dominates the content of inactive Li (Li$^+$/Li^0 < 1) as well as the capacity loss when CE is under ~ 95%. Once the CE is higher than ~ 95%, the amount of SEI Li$^+$ becomes dominating. The ratio of unreacted metallic Li^0/total inactive Li, and SEI Li$^+$/total inactive Li are further shown in Figure 4.2c and d.

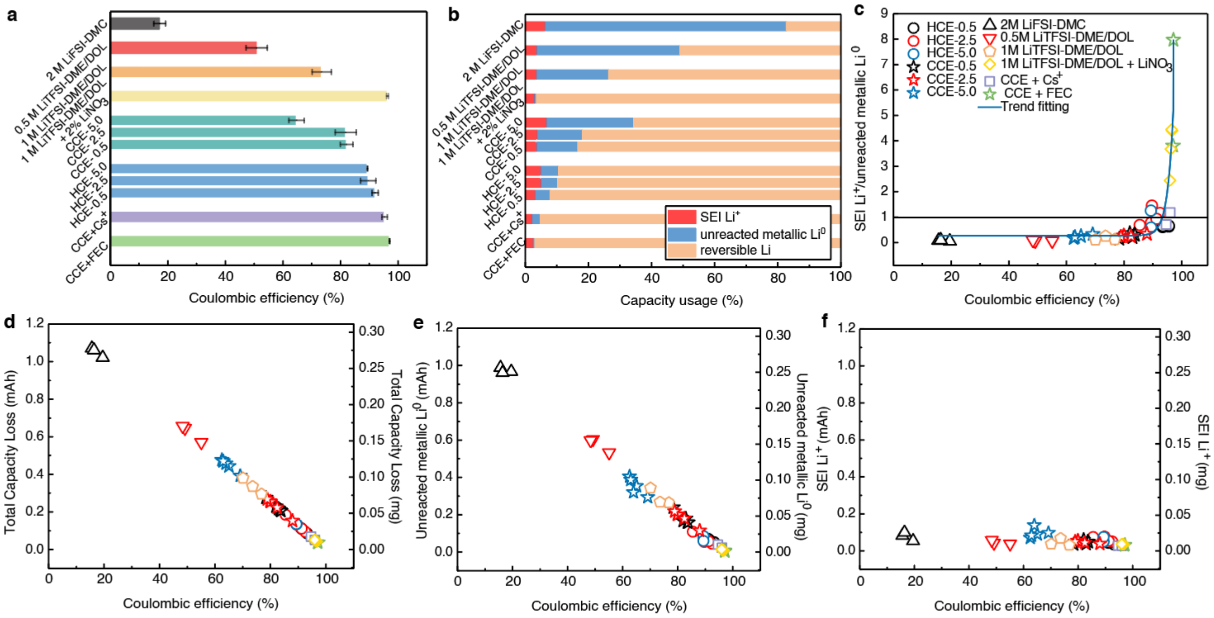

Figure 4. 1 Quantitative differentiation of inactive Li by the TGC method. (a) Average CE of Li||Cu cells under different testing conditions. Seven electrolytes (HCE, CCE, 2M LiFSI-DMC, 0.5M LiTFSI-DME/DOL, 1M LiTFSI-DME/DOL, CCE-Cs$^+$ and CCE-FEC) and 3 stripping rates (0.5, 2.5 and 5.0 mA cm^{-2}, all plating was done at 0.5 mA cm^{-2} for 1 mAh cm^{-2}) are used. **(b)** Capacity usage (SEI Li$^+$, unreacted metallic Li^0, and reversible Li) analysis under different testing conditions by TGC method. **(c)** Percentage analysis of SEI Li$^+$/unreacted metallic Li^0 based on TGC quantification results, the blue line indicates exponential fitting. **(d)** Total capacity loss as a function of CE. **(e)** Unreacted metallic Li^0 amount measured by the TGC method as a function of CE. **(f)** Calculated SEI Li$^+$ amount as a function of CE.

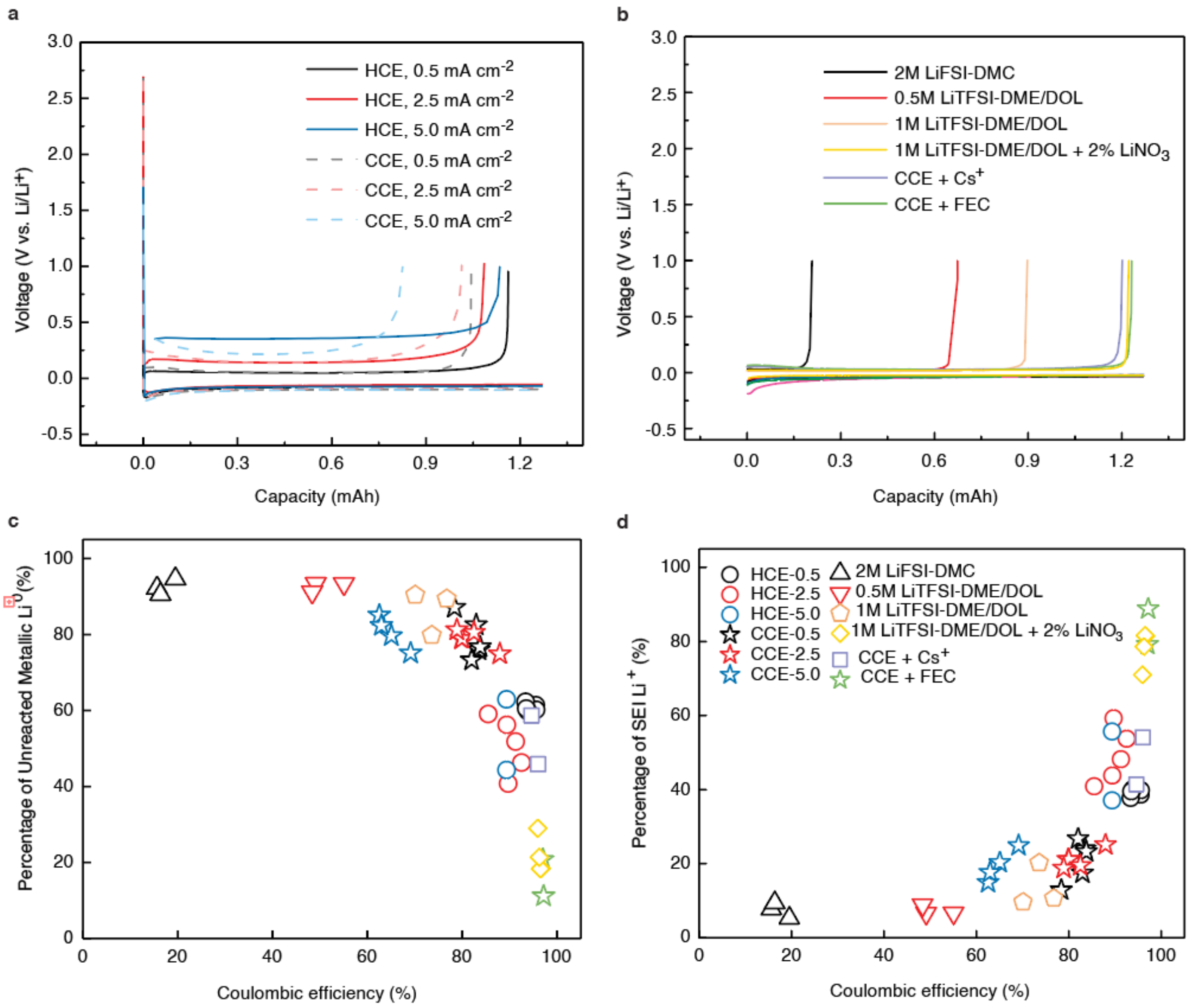

Figure 4. 2 Supplementary materials for TGC analysis. a, b, Representative voltage profiles of Li||Cu cells in (**a**) HCE and CCE, plating at 0.5 mA cm^{-2} for 1 mAh cm^{-2}, stripping to 1V at 0.5, 2.5 and 5.0 mA cm^{-2}; (**b**) 2M LiFSI-DMC, 0.5M LiTFSI-DME/DOL, 1M LiTFSI-DME/DOL, 1M LiTFSI-DME/DOL + 2% LiNO$_3$, CCE + Cs$^+$ and CCE + FEC, plating at 0.5 mA cm^{-2} for 1 mAh cm^{-2}, stripping to 1V at 0.5 mA cm^{-2}. **c,** The isolated metallic Li^0 percentage in total capacity loss (Li^0/Li^0 + Li$^+$). **d,** SEI Li$^+$ percentage in total capacity loss (Li$^+$/Li^0 + Li$^+$).

It is reported that increasing Li deposition capacity improves the first cycle CE[116]. To extend this method under different electrochemical conditions, we performed TGC tests on the CCE with increased Li plating capacities to 2, 3 and 5 mAh cm^{-2}, respectively. As shown in Figure 4.3, the TGC results clearly reveal that the SEI Li$^+$ amount increases with the extended deposition capacity; the improved CE with increased Li deposition capacity is due to the significantly reduced unreacted metallic Li^0. At 3 mAh cm^{-2}, the CE reaches 95.21%, while the ratio of SEI Li$^+$/unreacted metallic Li^0 measured to be 1.43, which is highly consistent with the above results.

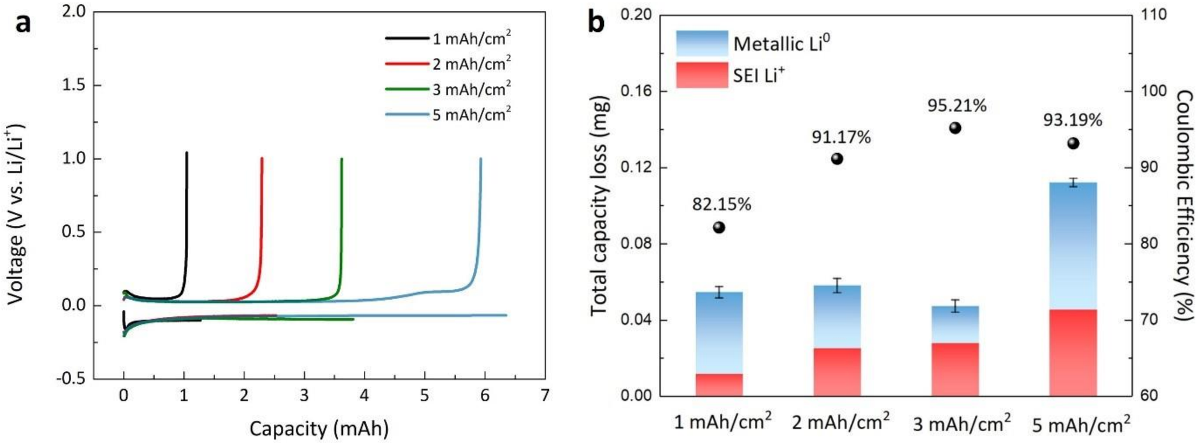

Figure 4. 3 The TGC analysis of inactive Li with different Li deposition capacities. (a) the voltage profiles of CCE with different deposition capacities at 0.5 mA/cm^2 for 1, 2, 3 and 5 mAh/cm^2, respectively. **(b)** the corresponding TGC analysis of inactive Li with associated capacity loss and CE under different deposition capacities. The TGC results clearly show that the SEI Li$^+$ amount increases with the extended deposition capacity; we observe that the improved CE with increased Li deposition capacity is associated with the significantly reduced inactive metallic Li^0. Particularly, at the deposition capacity of 3 mAh/cm^2, CE reaches 95.21%, while the ratio of SEI Li$^+$/unreacted metallic Li^0 (Li$^+$/ Li^0) measured to be 1.43, which is consistent with the conclusion that the SEI Li$^+$ dominates the capacity loss when CE is higher than 95%.

Besides the first cycle, we also investigated the ratio of SEI Li$^+$/unreacted metallic Li^0 after multiple cycles (2, 5, and 10) till the CE is stabilized around 90% in CCE. As shown in Figure 4.4, the Li$^+$/Li^0 ratio after 1, 2, 5, and 10 cycles remains 0.27, 0.30, 0.27 and 0.34, respectively, indicating the main capacity loss is from the inactive metallic Li^0. The TGC results also reveal that the unreacted metallic Li^0 amount accumulates during extended cycles, indicating the continuous consumption of active Li in LMBs. These experiments, with varying electrolytes, additives, deposition capacities and cycles, all validate the TGC method as a universally reliable tool in studying the inactive Li.

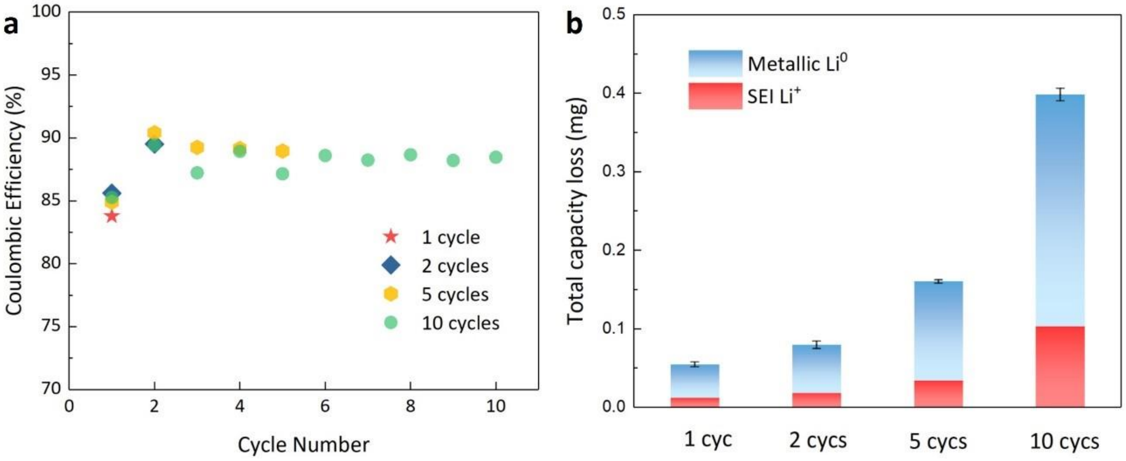

Figure 4. 4 The TGC analysis of inactive Li after multi cycles. (a) the cycling performance. **(b)** TGC analysis showing Li^0 and Li^+ contents with associated capacity loss after 1, 2, 5 and 10 cycles, respectively. The results are tested from the CCE, at 0.5 mA/cm^2 for 1 mAh/cm^2. The percentage of SEI Li^+ is 21.5%, 22.8%, 21.1% and 25.9% after 1, 2, 5 and 10 cycles, respectively. This suggests that even though the SEI percentage increased slightly after multiple cycles, the main capacity loss is still from the inactive metallic Li^0. The TGC results also reveal that the inactive Li is accumulating during extended cycles, indicating the continuous consumption of active Li in LMBs.

4.3 XPS analysis of inactive lithium under various conditions

4.3.1 Method

After a plating/stripping process, cells were disassembled in an Ar-filled glovebox with H_2O < 0.5 ppm. Cu foils with inactive Li residue were gently and thoroughly rinsed by DME (for HCE) and DMC (for CCE) to remove residual surface Li salts. The rinsed electrodes were sealed in an air-tight Dog-Bone type container and transferred into the glovebox that connected to XPS chamber. XPS was performed using a Kratos AXIS Supra with the Al anode source operated at 15 kV. The chamber pressure was $< 10^{-8}$ torr during all measurements. All XPS measurements were collected with a 300 µm by 700 µm spot size with a charger neutralizer during acquisition. Survey scans were collected with a 1.0 eV step size followed by high-resolution scans collected with a step size of 0.05 eV. Fittings of the XPS spectra were performed with CasaXPS software (version 2.3.15, Casa Software, Ltd.) to estimate the atomic compositions and chemical species. All species (Li 1s, F 1s, O 1s, and C 1s) were fitted using a Shirley type background. High-resolution spectra were calibrated using the C1s peak at 284.6 eV. The peak positions and areas were optimized by a Levenberg-Marquardt least-squares algorithm using 70% Gaussian and 30% Lorentzian line shapes. Quantification was performed based on Relative Sensitivity Factors (RSF). The curve fit for the core peaks was obtained using a minimum number of components to fit the experimental curves.

4.3.2 XPS results discussion

Further examining the SEI components in HCE and CCE by XPS, we found that stripping rates have negligible impact on the relative contributions from SEI components, as specified in

Figure 4.5. The TGC quantification analysis and XPS results firmly establish that the contribution from the SEI Li$^+$ to the global content of inactive Li is not as significant as commonly believed in previous studies[11,110,117].

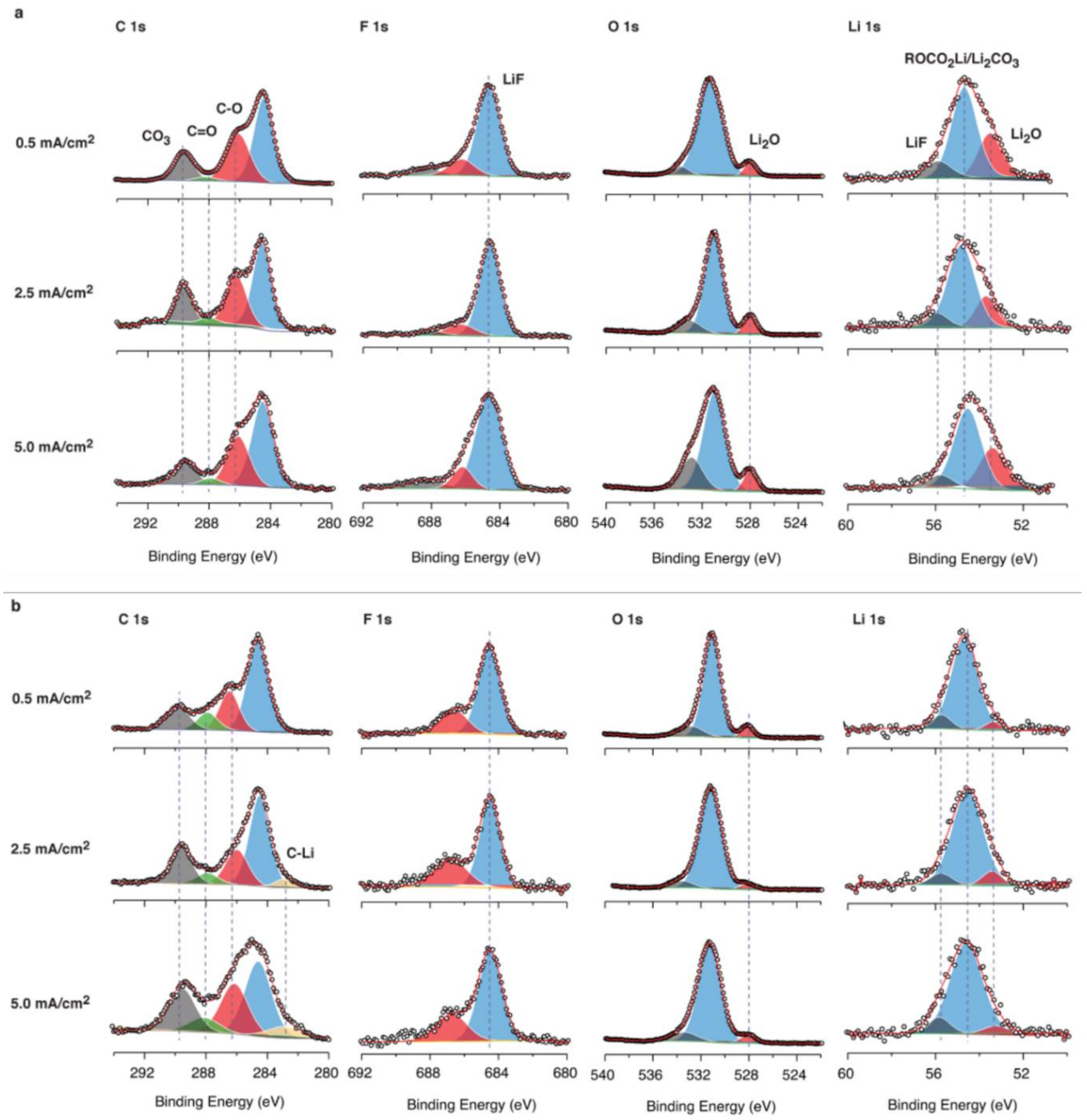

Figure 4. 5 XPS analysis of inactive Li SEI components formed in HCE and CCE under variety of stripping rates. a, inactive Li formed in HCE. **b,** inactive Li formed in CCE. The stripping rates show negligible impact on SEI components and contents in both electrolytes.

4.4 Microstructure of Inactive Lithium by Cryogenic Focused Ion Beam Scanning Electron Microscopy (cryo-FIB-SEM)

4.4.1 Method

The inactive Li samples on Cu foil were disassembled and washed with anhydrous DME (for HCE) or DMC (for CCE) in the Ar-filled glovebox. The samples were mounted on the SEM sample holder in the glovebox then transferred to a FEI Helios NanoLab Dualbeam. Platinum (Pt) was deposited for surface protection from the ion beam. 100 nm of Pt was deposited using the electron beam at 5 kV, 0.8 nA; 300 nm of Pt was deposited using the ion beam at 30 kV, 0.1 nA. The stage was cooled with liquid nitrogen to $\leq$-180 °C. Sample cross-sections were exposed using 1 nA ion beam current and 100 ns dwell time and cleaned twice at 0.5 nA and 0.1 nA, respectively. SEM images were taken with an ETD detector at 5 kV.

4.4.2 Microstructure of deposited lithium and Inactive Lithium formed under different conditions

In order to elucidate the formation mechanism of inactive Li, cryogenic focused ion beam-scanning electron microscopy (cryo-FIB-SEM) is used to explore the microstructures of inactive Li. HCE and CCE samples under different stripping rates are chosen for the morphological study. Cryogenic protection is critical here because the highly reactive Li metal is not only sensitive to the electron beam, but also is apt to react with the FIB incident Ga ion beam to form a Li_xGa_y alloy at room temperature[118]. Completely different morphologies are generated by variations in stripping rates even though starting from the same chunky morphology after plating at 0.5 mA cm^{-2} (Figure 4.6a-c). As the stripping rate increases, the morphology of inactive Li in HCE evolves from uniform sheets to local clusters (Figure 4.7a-c) with a thickness increased from 500 nm to 2 µm (Figure 4.7d-f). For the CCE, the deposited whisker-like Li (Figure 4.7d-f) becomes thinner after stripping (Figure 4.7g-i), and turns thicker in cross-section along with the increased stripping rates (Figure 4.7j-l), corresponding to the increased loss of CE at high rates. It is worth noting that these residues exhibit poor connection to the current collector, indicating the loss of electronic conductive pathways.

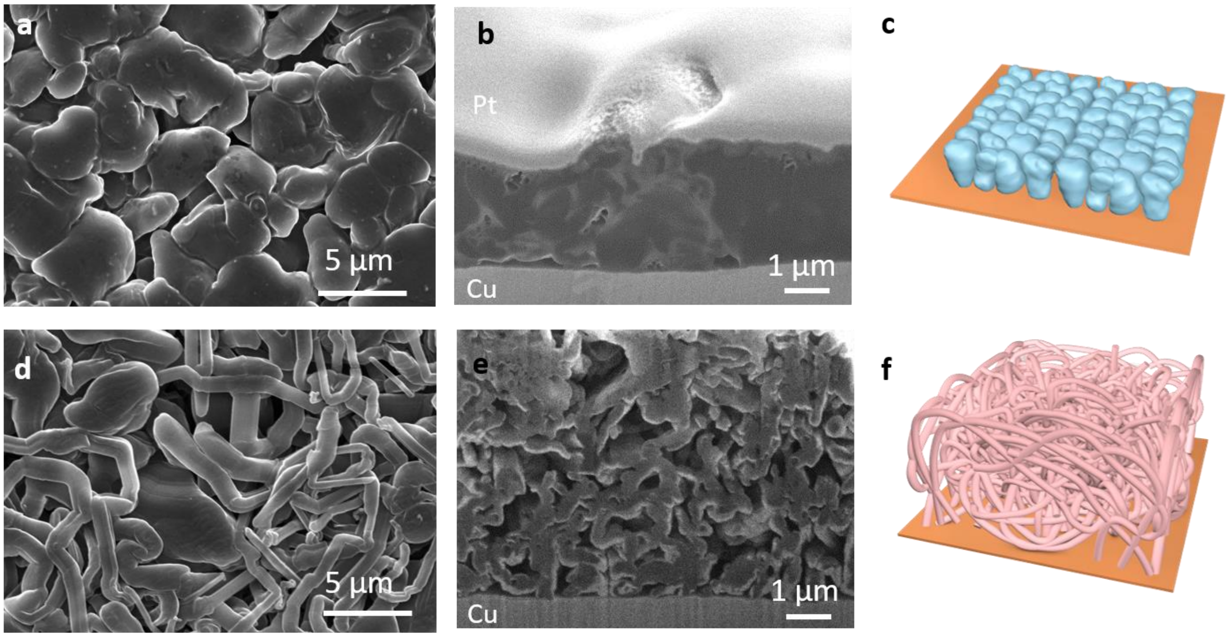

Figure 4. 6 Microstructure of electrochemically deposited Li in both HCE and CCE under 0.5 mA cm^{-2} to areal capacity of 0.5 mAh cm^{-2}, by Cryo-FIB-SEM. (a, b, and c) show the top view, cross-section and schematic in HCE, respectively. The deposited Li in HCE are large particles with sizes of several microns and reduced porosity. (d, e, and f) show the top view, cross-section and schematic in CCE, respectively. The deposited Li shows a mossy-like morphology with high porosity.

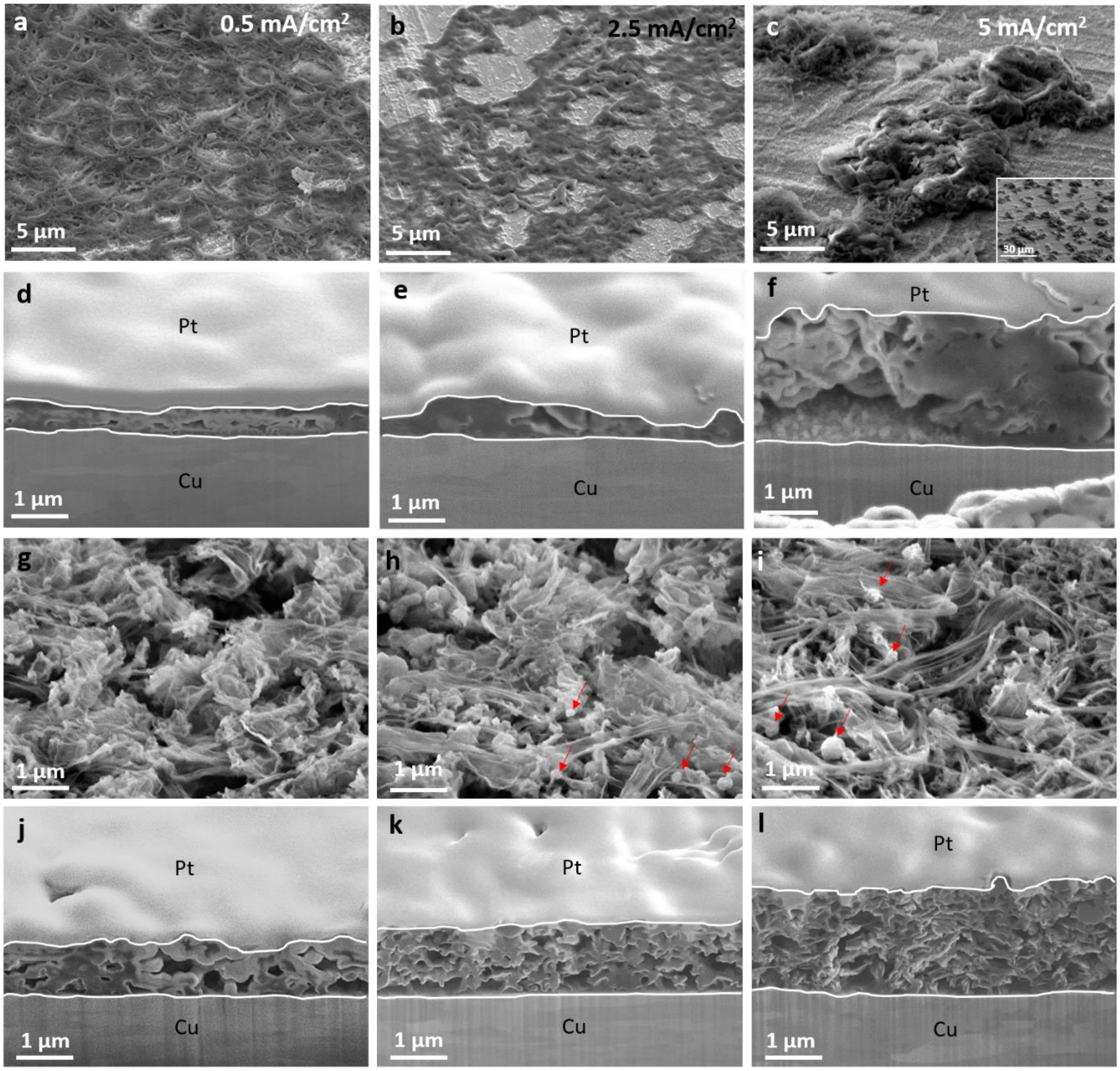

Figure 4. 7 Microstructures of inactive Li generated in HCE (a-f) and CCE (g-l) imaged by Cryo-FIB-SEM. (**a**-**c**) and (**g**-**i**) are top view of the inactive Li at 52° tilted stage. (**d**-**f**) and (**j**-**l**) are cross-sections obtained by cryo-FIB. Each column represents a stripping rate. (**a**, **d**, **g** and **j**) are at 0.5 mA cm^{-2}. (**b**, **e**, **h** and **k**) are at 2.5 mA cm^{-2}. (**c**, **f**, **i** and **l**) are at 5.0 mA cm^{-2}.

4.5 Nanostructure of inactive lithium by cryogenic transmission electron microscopy

4.5.1 Method

The Cryo-TEM sample for HCE was directly deposited and stripped on a lacey carbon grid in the Li||Cu half cell. While the sample for CCE was prepared by peeling the inactive Li from Cu foil cycled in the half cell onto the same type TEM grid. Both half cells were tested at current density of 0.5 mA cm^{-2} for plating and stripping Li for areal capacity of 1 mAh cm^{-2}. Both TEM samples were slightly rinsed with DME/DMC to remove trace Li salt in Ar-filled the glovebox. Once dry, the samples were sealed in airtight bags and plunged directly into a bath of liquid nitrogen. The airtight bags were then cut and the TEM grids were immersed in liquid nitrogen immediately. Then the grids were mounted onto a TEM cryo-holder (Gatan) via a cryo-transfer station. In short, the whole TEM sample preparation and transfer process prevents any contact of Li metal with the air at room temperature. TEM characterizations were carried out on JEOL JEM-ARM300CF at 300 kV and JEM-2100F at 200 kV. HRTEM images were taken at a magnification of 500 kx with Gatan OneView Camera (full 4K × 4K resolution) when the temperature of samples reached about 100 K. FFT pattern and Inverse FFT image after mask filtering were analyzed using DigitalMicrograph software.

4.5.2 Nanostructure of inactive lithium formed under different conditions

We further used cryo-TEM to investigate the nanostructure of the inactive Li in HCE and CCE after stripping at 0.5 mA cm^{-2}. Sheet-like inactive Li appears in the HCE sample (Figure 4.8a), while inactive Li in the CCE remains a whisker-like morphology (Figure 4.8e). Based on the (110) lattice plane distance of *bcc* Li, the region that contains crystalline metallic Li^0 is highlighted in green in the high-resolution TEM (HRTEM) images for both electrolytes (Figure 4.8b, f). Compared with the inactive Li obtained from CCE, a much smaller area of metallic Li^0 component is observed in HCE. This indicates that most deposited metallic Li^0 in HCE has been successfully stripped, corresponding to the high CE. Whisker-like unreacted metallic Li^0 as large as ~80 nm in length remains in the CCE sample and is well isolated by the surrounding SEI. The SEI components were determined by matching the lattice spacing in HRTEM images with their fast Fourier transform (FFT) patterns (Figure 4.8c, g). For the first time, the SEI components from more than 50 different sample positions is analyzed and provided in Figure 4.9 for better statistics. Consistent with the XPS results (Figure 4.5), Li_2CO_3 and Li_2O constitute the major part of SEI, which also contains LiF as well as other amorphous organic species for both electrolytes. The above observations from Cryo-TEM are summarized in the schematic plot (Figure 4.8d, h), which reveal the form of inactive Li with two different morphologies at nanoscale.

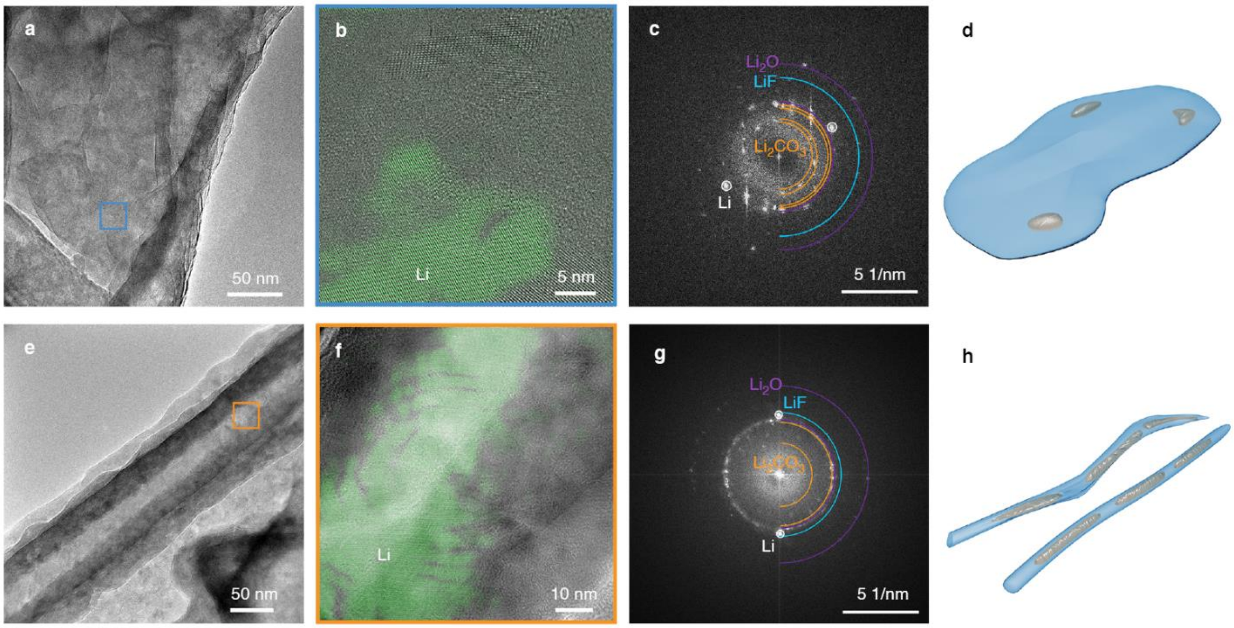

Figure 4. 8**Nanostructures of inactive Li generated in HCE (a-d) and CCE (e-h) by Cryo-TEM. a, e,** inactive Li morphology at low magnifications for both electrolytes. **b, f,** HRTEM shows a different amount of metallic Li^0 is wrapped by SEI in the two types of electrolytes. The highlighted metallic Li^0 region in green is identified through FFT-mask filtering-inverse FFT-image overlay process. **c, g,** FFT patterns of corresponding HRTEM indicate the SEI component which contains crystalline Li_2CO_3, Li_2O, and LiF. **d, h,** Schematic of inactive Li nanostructure in both electrolytes. Small area of metallic Li^0 is embedded in a sheet-like SEI layer for HCE, while a large bulk of metallic Li^0 is isolated in whisker-like SEI layer in CCE.

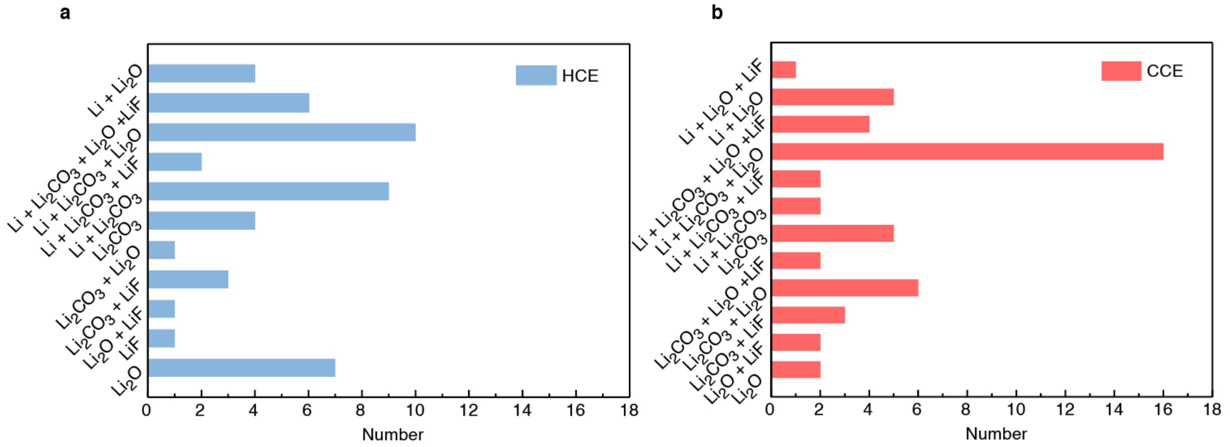

Figure 4. 9 a. Statistics of inactive Li SEI components formed in HCE from 50 different sample positions by cryo-TEM. **b.** Statistics of inactive Li SEI components formed in CCE from 50 different sample positions by cryo-TEM.

4.6 The formation mechanism of inactive lithium

Correlating the inactive metallic Li^0 content with the micro and nanostructures of inactive Li formed under different conditions, we propose an inactive Li formation mechanism as well as the stripping mechanism of Li metal. Two processes are involved in the stripping (Figure 4.10): 1) Li^+ dissolution. Under the electric field, metallic Li^0 is oxidized to Li^+, which diffuses through the SEI layers and dissolves into the electrolyte. 2) SEI collapse. When the Li is removed, the SEI simultaneously shrinks and collapses towards the current collector. During these two dynamic processes, we emphasize an ignored but crucial aspect, the structural connection, which is defined as the capability of the active Li to maintain an electronic conductive network. The cryo-FIB-SEM and cryo-TEM images show that inactive Li^0 either directly disconnected from the current collector or encapsulated by the insulating SEI, leading to the loss of structural c onnection. Obviously, for a Li deposit with whisker morphology and large tortuosity (Figure 4.11a, as from CCE), both manners of losing structural connection can easily occur due to the undesired microstructure, leading to poor structural connection and more unreacted metallic Li^0 remaining during the stripping process. In contrast, the dense Li with chunky morphology and low tortuosity (Figure 4.11b, as from HCE) has bulk integrity to maintain a structural connection and an intimate contact with the current collector, resulting in reduced presence of unreacted metallic Li^0 and high CE. This is further evidenced by an advanced novel electrolyte with columnar microstructure and minimum tortuosity which can deliver a first cycle CE as high as 96.2% (Figure 4.12a, b).

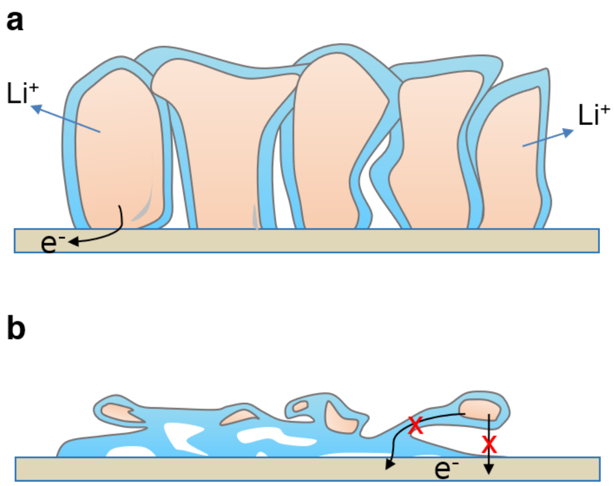

Figure 4. 10 Schematic of Li stripping process. a. Li ion dissolution. **b.** SEI layer collapse towards the current collector.

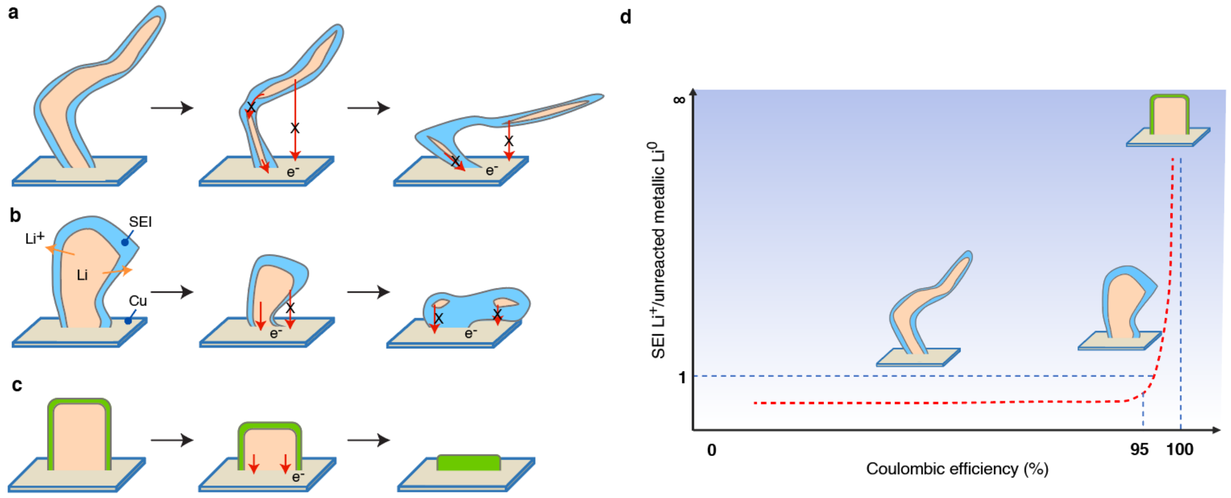

Figure 4. 11 Schematic of inactive Li formation mechanism in different electrolytes based on TGC quantification, Cryo-FIB-SEM and Cryo-TEM observation. a, Li deposits with whisker morphology and large tortuosity are more likely to lose electronic connection and maintain poor structural connection, leaving large amount of unreacted metallic Li^0 trapped in SEI. b, Li deposits with large granular size and less tortuosity tend to maintain a good structural electronic connection, only bits of metallic Li^0 are stuck in tortuous SEI edges. c, An ideal Li deposit should have a columnar microstructure with a large granular size and minimum tortuosity and homogeneous distribution of SEI components, facilitating a complete dissolution of metallic Li^0. d, A general correlation of Li deposits morphology, CE, and the ratio of SEI Li^+/unreacted metallic Li^0

4.7 Mitigation strategies of inactive lithium formation

Based on the above observation and discussion, we propose the following strategies that could improve CE. An ideal architecture of deposited Li would promote a good structural connection and mitigate the inactive Li formation, especially the formation of unreacted metallic Li^0. The ideal architecture includes 1) The Li deposits should retain a columnar microstructure with a large granular size and minimum tortuosity to minimize the unreacted metallic Li^0 residue (Figure 4.11c, d); 2) The SEI should be both chemically and spatially homogeneous so that uniform Li^+ dissolution occurs; the SEI should be mechanically elastic enough to accommodate the volume change; the SEI could be refilled during extended cycles, as schematized in Figure 4.12g. Using advanced electrolytes and artificial SEI may help to meet these requirements, while three-dimensional (3D) hosts that maintain electronic pathway and low tortuosity can contribute to constructing a durable structural connection and guiding the Li plating and stripping. To testify this hypothesis, we compared the 2D Cu foil and 3D Cu foam as the current collectors (Figure 4.12c, d). The initial CE of 2D Cu foil and 3D Cu foam are 82% and 90%, respectively (Figure 4.12e). The increased CE in the latter is attributed to the reduced amount of the unreacted metallic Li^0 (Figure 4.12f), despite that SEI Li^+ amount increases from 21.5% to 62.7% due to the higher surface area of 3D Cu foam. Therefore, while the 3D current collector helps maintaining a good electronic conductive network, it is necessary to control the surface properties of 3D current collector to minimize the SEI formation. The structural connection can also be further enforced by applying proper external pressure. Slight stacking pressure has been known to be helpful in improving cycling performance significantly[119,120]. In our proposed model, we believe that pressure promotes the structure collapse towards the current collector, thus leads to a better structural connection which mitigates the generation of unreacted metallic Li^0. We found that the critical pressure in maintaining good structural connection to be as small as ~ 5 psi, which should not damage any SEI (Figure 4.12h). Fast stripping rate could accelerate the Li^+ dissolution but may be destructive to structural connection, because of the fast dynamic that Li at the tip of column or whisks could fail to keep pace with. Overall, the tools established here can be universally extended to examine various battery chemistries under different conditions towards a better battery that is energy-dense and safe.

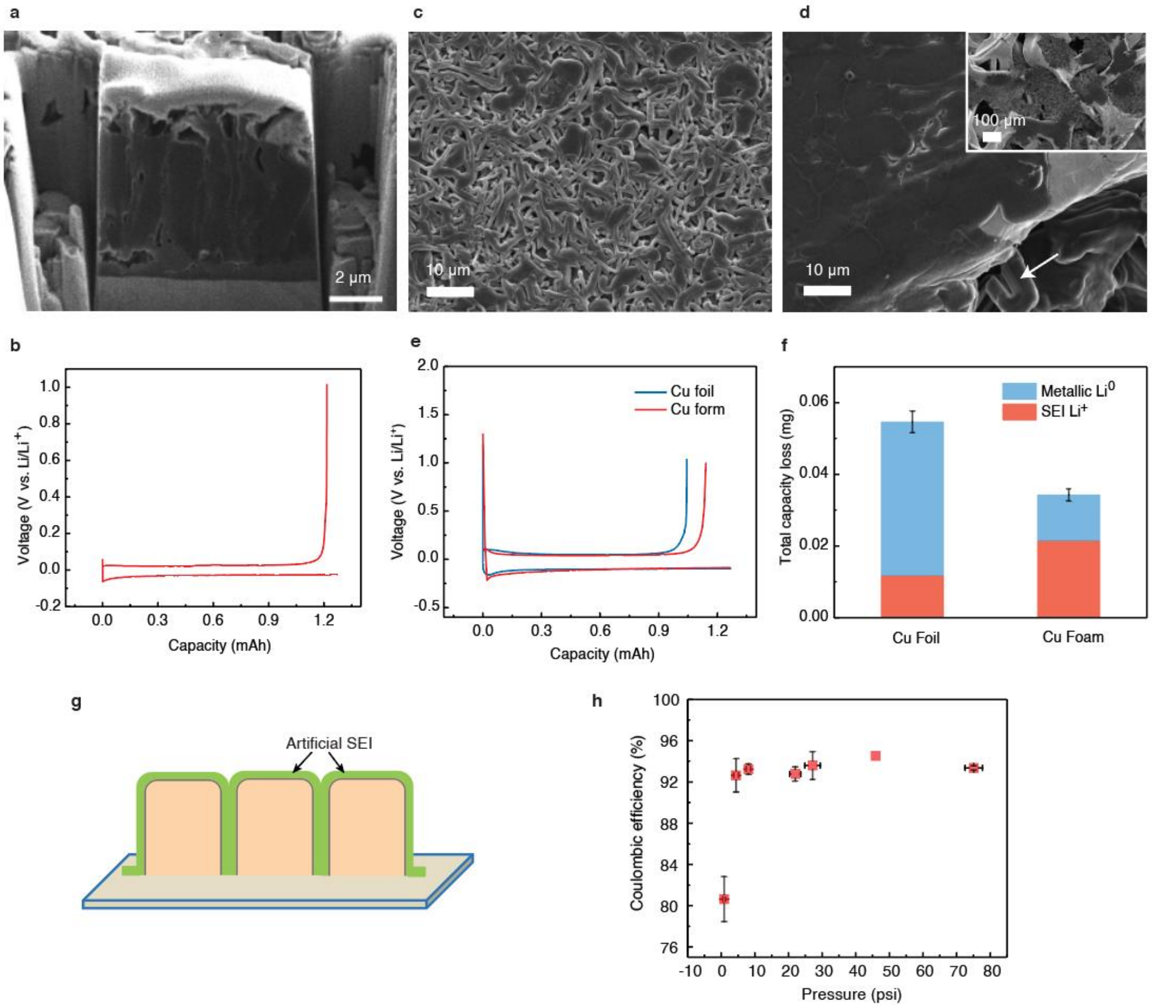

Figure 4. 12 **Strategies that may mitigate inactive Li formation.** **a.** The cross-section morphology of Li deposits generated in an advanced electrolyte developed by General Motors (GM), showing a unique columnar structure. **b.** The GM electrolyte delivers a first cycle CE of 96.2%, plating at 0.5 mA cm^{-2} for 1 mAh cm^{-2}, stripping at 0.5 mA cm^{-2} to 1 V. **c-f,** 3D current collector. **c,** SEM image of Li deposits on Cu foil. **d,** SEM image of Li deposits on Cu foam. Both were deposited at 0.5 mA cm^{-2} for 1 mAh cm^{-2} in CCE. **e.** Representative first cycle voltage profiles of Cu foil and Cu foam, plating at 0.5 mA cm^{-2} for 1 mAh cm^{-2}, stripping at 0.5 mA cm^{-2} to 1 V in CCE. **f.** TGC quantification of inactive Li for Cu foil and Cu foam samples. **g.** Schematic of an ideal artificial SEI design. The polymer based artificial SEI should be chemically stable against Li metal and mechanically elastic enough to accommodate the volume and shape change. Meanwhile, the edges of the artificial SEI should be fixed to the Li metal or the current collector, avoiding electrolyte to diffuse and contact with fresh Li metal. The flexible polymer SEI thus can accommodate the expansion and shrinkage during repeated Li plating and stripping. In this way, no Li will be consumed to form SEI during extended cycles and we can thus realize the anode-free Li metal batteries. **h.** Influence of pressure on Li plating/stripping. The results are from the HCE, at 0.5 mA cm^{-2} for 1 mAh cm^{-2}, using a load cell. At each condition, two load cells were measured. The error bars indicate the standard deviation.

4.8 Conclusion

In summary, this work has established a novel quantitative methodology to accurately differentiate and quantify the inactive Li on multi-scales. The TGC results reveal that the amount of unreacted Li^0 governs the loss of CE, as indicated by their linear relationship. This discovery unequivocally settles the long-lasting debates over the role of the two forms (SEI Li^+ and metallic Li^0) of inactive Li. The morphological study by Cryo-FIB-SEM shows that the microstructures, such as particle sizes and tortuosity, of the deposited Li play key roles in maintaining the structural electronic connection. Cryo-TEM confirmed that the isolated particles of Li^0 is indeed trapped in the electronically insulating SEI. Correlating these observations, we proposed the formation mechanism of inactive Li, revealing that the true underlying cause of low CE in LMBs is due to large amount of metallic Li^0 becoming trapped in SEI with tortuous microstructures. We also offered strategies to mitigate inactive Li formation and thus significantly improve CE. With an ideal columnar microstructure, it could be possible that the capacity loss will only come from the minor SEI formation in the initial cycle and the anode-free battery can thus be realized. The versatile characterization tools established here can be further extended to investigate inactive Li properties under different conditions, such as current densities, temperatures as well as electrolyte compositions, and serve as a standard methodology to evaluate the strategies that improve the performance of Li metal. We anticipate this novel methodology to be universally adopted for systematic study of all current and future battery chemistries.

Chapter 3 and Chapter 4, in full, is a reprint of the material “Quantifying inactive lithium in lithium metal batteries” as it appears in the Nature, **Chengcheng Fang***, Jinxing Li*, Minghao Zhang, Yihui Zhang, Fan Yang, Jungwoo Z. Lee, Min-Han Lee, Judith Alvarado, Marshall A. Schroeder, Yangyuchen Yang, Bingyu Lu, Nicholas Williams, Miguel Ceja, Li Yang, Mei Cai, Jing Gu, Kang Xu, Xuefeng Wang and Ying Shirley Meng, 2019, 572, 511-515. The dissertation author was the co-primary investigator and author of this paper. The author conducted all the experiment and data analysis except for the TEM data collection, and cowrote the paper.

Chapter 5 Conclusion and Future Perspectives

5.1 Main challenges with Li metal: dendrite formation or low Coulombic efficiency?

It is widely accepted that Li dendrite formation and low CE are two primary obstacles hindering Li metal batteries [109]. In addition, other challenges associated with Li metal anodes include volume expansion, poor cycle life, capacity fading, increased overpotential, and potential safety hazards. It is commonly thought that Li dendrites can mechanically pierce the separator, causing a short in the cell that potentially results in thermal runaway and explosion[9]. Figure 5.1a shows a Li dendrite model that has been widely spread to illustrate the potential dangers of Li dendrites. This dendritic morphology was originally observed in a beaker cell via optical microscopy [109,121,122]. However, in real coin cells and pouch cells, this morphology has rarely been observed or reported. Instead, whisker-like Li deposits are commonly observed in commercial carbonate-based electrolytes and even solid-state batteries (Figure 5.1b), due to the heterogeneous nature of SEI layers, ion concentration and local current density[123]. These Li whiskers interweave parallel to the separator (rather than perpendicular); only a perpendicular whisker can potentially penetrate the separator and cause a cell short. Moreover, chunky Li deposits with large granular size (Figure 5.1c) have been observed in many of recently developed advanced electrolytes. Based on these findings, it is misleading to continuously ascribe the major problem associated with Li metal anodes to dendritic growth and its resultant internal short circuit/thermal runaway. Lu and colleagues have also refuted the dendrite-penetration-related failure mechanism by SEM analysis of an Li anode cross-section after 100 cycles [100]. Undoubtedly, the Li dendrites, or more precisely Li whiskers, play a critical role in affecting Li metal battery performance. However, it is likely via other avenues, including increasing surface area and causing large volume expansion, rather than directly causing a short circuit.

We believe that the primary issue with Li metal stems from the low CE, which directly reduces the battery cycle life. As cycling proceeds, both fresh Li metal and electrolyte are consumed continuously forming inactive Li (provided that the cycle CE is <100%). Thus, cycle life and stability in a Li metal cells are directly proportional to the amount of excess Li and electrolyte [124]. However, the CE of Li metal in conventional carbonate electrolytes is <90%, indicating that most Li metal cells fail via consumption of active Li or depletion of electrolyte (rather than short circuiting caused by Li whiskers). Even for advanced electrolytes that enable highly efficient Li plating/stripping with CE ~ 99%, the 1% inefficiency remains problematic. To achieve a desired cycle life, excess amounts of fresh Li and electrolyte are needed, rendering it difficult to further improve the cell-level energy density. Thus, it is becoming inescapable to improve the CE of Li metal to extend the cycle life of the Li metal batteries.

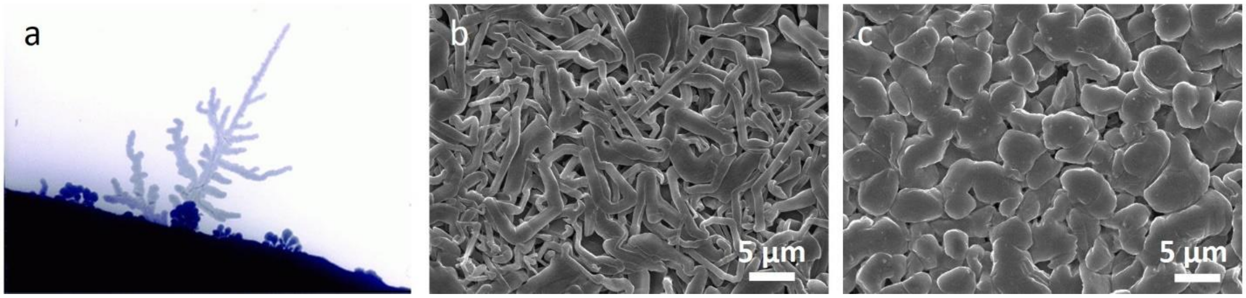

Figure 5. 1 The morphologies of electrochemically deposited Li under different conditions. (a) the famous optical microscope image representing Li dendrites; (b) whisker-like Li deposited in commercial carbonate electrolyte (1M $LiPF_6$ in EC/EMC, 3:7 with 2% of VC, 0.5 mA/cm^2, 1 mAh/cm^2); (c) chunky Li with a large granular size formed in high concentration ether-based electrolyte (4M LiFSI in DME, 0.5 mA/cm^2, 1 mAh/cm^2)

5.2 Inactive Li Formation Causes Low Coulombic efficiency: SEI Li^+ or Unreacted metallic Li?

Low Li-metal CE stems from the loss of active Li as it forms the SEI and unreacted metallic Li, which together comprise inactive Li (also known as “dead” Li). SEI formation is a result of the (electro)chemical reaction between highly reactive Li metal and the electrolyte, whereas unreacted metallic Li is isolated from the electronically conductive network during stripping by the insulating SEI, thus becoming inactive [28,125,126].

The importance of the SEI has been reviewed exhaustively [16,41,103]; however, quantitative characterization of SEI properties remains elusive, including: chemical compositions, nanostructure, and mechanical properties. This is partly due to the brittle and heterogeneous nature of the SEI. It is generally believed that dramatic volume changes yield fractures in the SEI during Li stripping/plating.[15] This fracturing results in continuous SEI formation that consumes both the active Li and electrolyte. This process is further accelerated by growth of porous Li whiskers. With this in mind, many researchers attribute the continuous formation of SEI as the primary reason for capacity loss and low CE, without further quantitative verification [48]. However, it was recently reported that this picture is not correct following quantification of both the SEI Li^+ and unreacted metallic Li after stripping via the recently developed Titration Gas Chromatography (TGC) [127]. Importantly, TCG results reveal that the capacity loss of Li metal anodes is primarily dominated by unreacted metallic Li that is trapped by the insulating SEI. The overall SEI Li^+ amount in the inactive Li remains almost identical and at a relatively low amount under different testing conditions. This suggests that the main loss of CE in Li metal batteries does not come from SEI formation but rather from the unreacted metallic Li. The capacity loss from forming SEI has been over-blamed for decades. Although the amount is low, we still want to emphasize that the SEI cannot been overlooked since its chemical and mechanical properties directly dictate the surface properties of the EDLi, directly affecting the dynamic Li plating and stripping process. Much work is still needed to correlate the SEI properties to the electrochemical behavior and performance of Li metal anodes.

5.3 Strategies for improving Coulombic efficiency

Many strategies have been proposed to improve CE, including: electrolyte engineering [112,128,129], use of a 3D host [130,131], separator modification [132,133], and artificial SEI engineering [113,134], for example, atomic/molecular layer deposition has been proved an effective approach to enhance the CE and decrease the formation of "dead" Li [135–137]. Among these strategies, the most effective and promising is developing new electrolytes that enable both high efficiency Li-metal and stable high-voltage cathode operation. Dense Li deposition with a CE > 99% is readily obtained [18,19,21,22], however, a 99.97% CE is required for a commercially viable Li metal anode that must undergo 1000 cycles [2].

To close the gap of <1% CE loss per cycle further, we must fully understand the growth and failure mechanism of Li metal in both liquid and solid-state electrolytes by employing state-of-the-art characterization tools. For example, operando optical microscopy [27] and in-situ transmission electron microscopy (TEM) [36] were combined to probe the dynamic growth of Li dendrites on a wide range of length and time scales. In particular, Cryo-EM eliminates detrimental beam damage on fragile Li metal and affords nanostructure visualization. Unexpectedly, amorphous Li has been detected at the early stage of Li deposition [25]. Aside from microscopy, other techniques are also needed to quantitatively probe the structure and amount of Li metal/SEI, such as TGC [127]. Significant advances in characterization are helping researchers get unprecedentedly close to truly understanding the Li metal failure mechanism and rationally overcoming the previously stated obstacles for Li metal.

Recently, Meng and colleagues [127] used cryo-TEM to observe the nanostructure of inactive Li, revealing that unreacted metallic Li is trapped by the SEI. Further, it was shown that the unreacted metallic Li amount is closely correlated with the Li-deposit microstructure. A large quantity of unreacted metallic Li is easily trapped in tortuous matrix of the whisker-like Li, resulting in a low CE. In contrast, a smaller quantity of unreacted metallic Li is present following stripping large chunky Li deposits with lower porosity. Consequently, we assert that whisker-like Li is an undesired microstructure that accelerates formation of inactive metallic Li as well as infinite volume expansion thereby yielding low CE (rather than assigning potential safety concerns to Li-dendrite formation). Therefore, we propose that chunky Li deposits are the preferred microstructure for maintaining a suitable electronic connection between deposited Li and the current collector in a limited volume space. In addition, this preferred morphology implies that significantly less unreacted metallic Li will be trapped in the SEI, thereby affording an improved CE. Thus, we anticipate that strategies to bias Li deposits to forming a columnar chunk morphology will be effective in further improving CE and confining the volume expansion. Figure 5.2 summarizes the cause and solutions for Li metal problems.

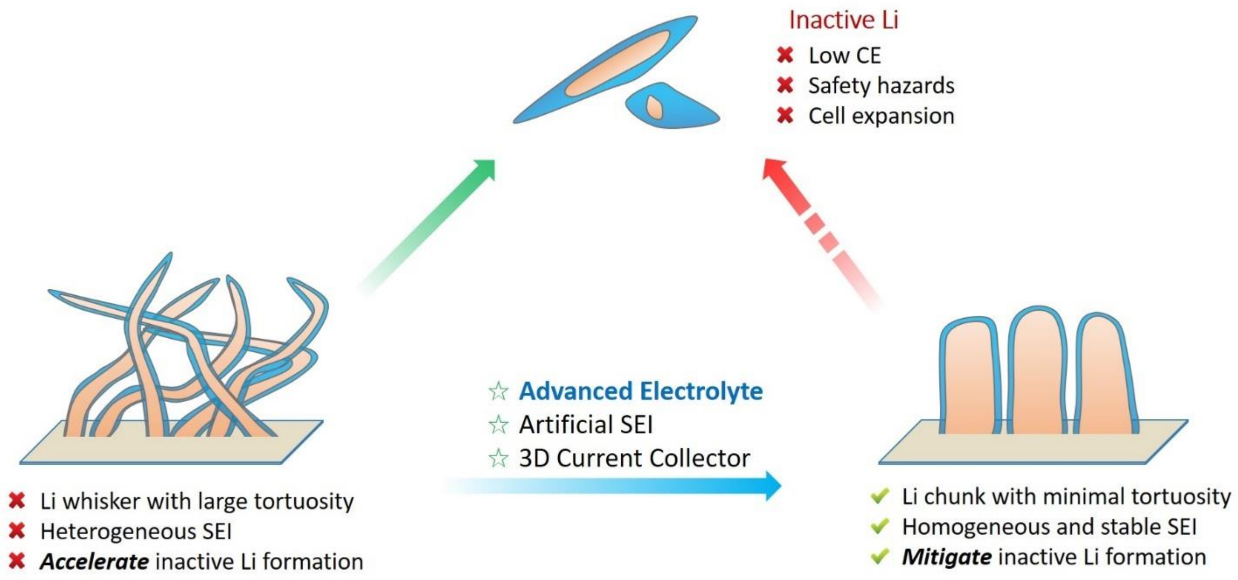

Figure 5. 2 The cause and solution for the Li metal problems. The continuous formation of inactive Li is the direct cause of low CE, safety hazards and cell expansion in Li metal batteries. Li whiskers with large tortuosity and heterogeneous SEI will facilitate the inactive Li formation and cause the series of problems; whereas if the deposited Li possesses a chunky morphology with minimal tortuosity and homogeneous SEI, the inactive Li formation will be significantly reduced, resulting in high CE. To do so, advanced electrolyte engineering will be primary method, with the assistance of artificial SEI and 3D current collector.

5.4 Concluding Remarks and Future Perspectives

We demonstrate that the major problem of Li metal is the low CE rather than the Li dendrites. Most Li metal cells fail due to the consumption of active Li or depletion of electrolytes, rather than the short circuit caused by the Li dendrite/whisker. The loss of CE is mostly dominated by the formation of unreacted metallic Li rather than the SEI, which is related to the microstructure of Li deposits.

In the future, research effort should be devoted on how to reduce the amount of unreacted metallic Li by tuning the nanostructure and microstructure of deposited Li during both the plating and stripping processes. An ideal Li deposit should have a columnar morphology; the SEI layer should be homogeneous in components and their distribution, possess proper mechanical strength and elasticity; the deposited Li volume should be close to the theoretic number. Advancing electrolytes will undoubtably be the most effective solution to generate these large Li chunks with minimum tortuosity. A combination of the 3D substrate which helps maintain good electronic conductive pathways and an artificial SEI with all the desired properties may also be required to enhance the structural connection for electrons and ion transfer through the SEI, which together could potentially realize the CE goal of more than 99.97%.

To engineeringly carry out these strategies, a thorough understanding of SEI properties is the key. Thanks to cryo-EMs, we are now able to correlate the nanostructure of Li metal with the electrochemical performance at different conditions. Operando/*in-situ* cryo-EM should be soon established to probe the dynamic processes of Li metal and its SEI during plating and stripping. Although the SEI amount is low, it plays an important role on altering and affecting the Li behavior, by which ways we should figure out in the future. Some interesting questions are remained, for example, what is the ideal structure of SEI and how to achieve it? How do Li ions diffuse through the SEI? Will the Li refill the as-formed SEI shells in subsequent cycles or not? How to achieve ideal columnar Li deposits? Answering these questions are of vital importance towards rationally eliminating the 1% of CE loss to ultimately make the Li metal batteries commercially available.

Lastly, we advocate the field to follow standardized testing protocols for more effective knowledge transfer. As we mentioned before, the cycle life and cycling stability in a Li metal cell are directly proportional to the excess amount of Li and of the electrolyte. Many reported cycling data are based on a large excess of electrolyte and effectively an infinite excess amount of Li metal in coin cells; these methodologies do not accurately reflect the true performances of the reported strategies. Battery research and development has reached a point that scientific research advances are evaluated and assessed by how rapidly and reproducibly they can be deployed in a commercially relevant design. This extremely demanding trend itself is a double-edged sword as it might constrain the creativity of the scientists, but if successful it will accelerate the realization of next generation batteries. When developing strategies of improving the CE in Li metal anode, we advocate researchers rise up to the tough technical challenges, apply and report strict standards, including high mass loading of active cathode materials (≥ 4 mAh/cm^2), proper current density (> 0.5 mA/cm^2), lean electrolyte (≤ 3 g/Ah), and a limited excess amount of Li metal (<50 µm thickness), to evaluate if these strategies are truly effective for a practical rechargeable Li metal battery.

Chapter 5, in full, is a reprint of the material “Key Issues Hindering a Practical Lithium Metal Battery” as it appears in the Trends in Chemistry, **Chengcheng Fang**, Xuefeng Wang, Ying Shirley Meng, 2019, 1, 152-158. The dissertation author was the primary investigator and author of this paper. The author wrote the paper.

References

[1] M. Winter, B. Barnett, K. Xu, Before Li Ion Batteries, Chem. Rev. 118 (2018) 11433–11456. doi:10.1021/acs.chemrev.8b00422.

[2] P. Albertus, S. Babinec, S. Litzelman, A. Newman, Status and challenges in enabling the lithium metal electrode for high-energy and low-cost rechargeable batteries, Nat. Energy. 3 (2018) 16–21. doi:10.1038/s41560-017-0047-2.

[3] J. Liu, Z. Bao, Y. Cui, E.J. Dufek, J.B. Goodenough, P. Khalifah, Q. Li, B. Yann Liaw, P. Liu, A. Manthiram, Y. Shirley Meng, V.R. Subramanian, M.F. Toney, V. V Viswanathan, M. Stanley Whittingham, J. Xiao, W. Xu, J. Yang, X.-Q. Yang, J.-G. Zhang, Pathways for practical high-energy long-cycling lithium metal batteries, Nat. Energy. 4 (2019) 180–186. doi:10.1038/s41560-019-0338-x.

[4] J.B. Goodenough, K.-S. Park, The Li-Ion Rechargeable Battery: A Perspective, J. Am. Chem. Soc. 135 (2013) 1167–1176. doi:10.1021/ja3091438.

[5] C. Niu, H. Pan, W. Xu, J. Xiao, J.-G. Zhang, L. Luo, C. Wang, D. Mei, J. Meng, X. Wang, Z. Liu, L. Mai, J. Liu, Self-smoothing anode for achieving high-energy lithium metal batteries under realistic conditions, Nat. Nanotechnol. 14 (2019) 594–601. doi:10.1038/s41565-019-0427-9.

[6] B. Qiu, M. Zhang, Y. Xia, Z. Liu, Y.S. Meng, Understanding and Controlling Anionic Electrochemical Activity in High-Capacity Oxides for Next Generation Li-Ion Batteries, Chem. Mater. 29 (2017) 908–915. doi:10.1021/acs.chemmater.6b04815.

[7] J.B. Goodenough, Y. Kim, Challenges for Rechargeable Li Batteries †, Chem. Mater. 22 (2010) 587–603. doi:10.1021/cm901452z.

[8] M.S. Whittingham, Electrical energy storage and intercalation chemistry, Science (80-.). 192 (1976) 1126–1127. doi:10.1246/cl.2012.972.

[9] J.M. Tarascon, M. Armand, Issues and challenges facing rechargeable lithium batteries, Nature. 414 (2001) 359–367.

[10] S. Megahed, Bruno Scrosati, Lithium ion rechargeable batteries, J. Power Sources. 51 (1994) 79–104. doi:10.1109/WESCON.1993.488436.

[11] J. Lu, T. Wu, K. Amine, State-of-the-art characterization techniques for advanced lithium-ion batteries, Nat. Energy. 2 (2017) 17011. doi:10.1038/nenergy.2017.11.

[12] K.N. Wood, M. Noked, N.P. Dasgupta, Lithium metal anodes: toward an improved understanding of coupled morphological, electrochemical, and mechanical behavior, ACS Energy Lett. 2 (2017) 664–672. doi:10.1021/acsenergylett.6b00650.

[13] Y. Fan, X. Chen, D. Legut, Q. Zhang, Modeling and theoretical design of next-generation lithium metal batteries, Energy Storage Mater. 16 (2019) 169–193.

doi:10.1016/j.ensm.2018.05.007.

[14] X.B. Cheng, R. Zhang, C.Z. Zhao, Q. Zhang, Toward safe lithium metal anode in rechargeable batteries: a review, Chem. Rev. 117 (2017) 10403–10473. doi:10.1021/acs.chemrev.7b00115.

[15] D. Lin, Y. Liu, Y. Cui, Reviving the lithium metal anode for high-energy batteries, Nat. Nanotechnol. 12 (2017) 194–206. doi:10.1038/NNANO.2017.16.

[16] J. Zheng, J.A. Lochala, A. Kwok, Z.D. Deng, J. Xiao, Research progress towards understanding the unique interfaces between concentrated electrolytes and electrodes for energy storage applications, Adv. Sci. 4 (2017) 1–19. doi:10.1002/advs.201700032.

[17] J. Qian, W.A. Henderson, W. Xu, P. Bhattacharya, M. Engelhard, O. Borodin, J.-G. Zhang, High rate and stable cycling of lithium metal anode, Nat. Commun. 6 (2015) 6362. doi:10.1038/ncomms7362.

[18] X. Fan, L. Chen, X. Ji, T. Deng, S. Hou, J. Chen, J. Zheng, F. Wang, J. Jiang, K. Xu, C. Wang, Highly Fluorinated Interphases Enable High-Voltage Li-Metal Batteries, Chem. 4 (2018) 174–185. doi:10.1016/j.chempr.2017.10.017.

[19] J. Wang, Y. Yamada, K. Sodeyama, E. Watanabe, K. Takada, Y. Tateyama, A. Yamada, Fire-extinguishing organic electrolytes for safe batteries, Nat. Energy. 3 (2018) 22–29. doi:10.1038/s41560-017-0033-8.

[20] J. Wang, Y. Yamada, K. Sodeyama, C.H. Chiang, Y. Tateyama, A. Yamada, Superconcentrated electrolytes for a high-voltage lithium-ion battery, Nat. Commun. 7 (2016) 1–9. doi:10.1038/ncomms12032.

[21] Z. Zeng, V. Murugesan, K.S. Han, X. Jiang, Y. Cao, L. Xiao, X. Ai, H. Yang, J.G. Zhang, M.L. Sushko, J. Liu, Non-flammable electrolytes with high salt-to-solvent ratios for Li-ion and Li-metal batteries, Nat. Energy. 3 (2018) 674–681. doi:10.1038/s41560-018-0196-y.

[22] S. Chen, J. Zheng, D. Mei, K.S. Han, M.H. Engelhard, W. Zhao, W. Xu, J. Liu, J.G. Zhang, High-Voltage Lithium-Metal Batteries Enabled by Localized High-Concentration Electrolytes, Adv. Mater. 1706102 (2018) 1–7. doi:10.1002/adma.201706102.

[23] X. Ren, S. Chen, H. Lee, J. Liu, X. Ren, S. Chen, H. Lee, D. Mei, M.H. Engelhard, S.D. Burton, W. Zhao, J. Zheng, Q. Li, M.S. Ding, M. Schroeder, Localized high-concentration sulfone electrolytes for high-efficiency lithium-metal batteries, Chem. 4 (2018) 1877–1892. doi:10.1016/j.chempr.2018.05.002.

[24] Y. Li, Y. Li, A. Pei, K. Yan, Y. Sun, C.-L. Wu, L.-M. Joubert, R. Chin, A.L. Koh, Y. Yu, J. Perrino, B. Butz, S. Chu, Y. Cui, Atomic structure of sensitive battery materials and interfaces revealed by cryo-electron microscopy, Science, 1585 (2017).506-510. doi: 10.1126/science.aal1585.

[25] X. Wang, M. Zhang, J. Alvarado, S. Wang, M. Sina, B. Lu, J. Bouwer, W. Xu, J. Xiao, J.-

G. Zhang, J. Liu, Y.S. Meng, New insights on the structure of electrochemically deposited lithium metal and its solid electrolyte interphases via cryogenic TEM, Nano Lett. 17 (2017) 7606–7612. doi:10.1021/acs.nanolett.7b03606.

[26] M.J. Zachman, Z. Tu, S. Choudhury, L.A. Archer, L.F. Kourkoutis, Cryo-STEM mapping of solid–liquid interfaces and dendrites in lithium-metal batteries, Nature. 560 (2018) 345–349. doi:10.1038/s41586-018-0397-3.

[27] K.N. Wood, E. Kazyak, A.F. Chadwick, K.-H. Chen, J.-G. Zhang, K. Thornton, N.P. Dasgupta, Dendrites and Pits: Untangling the Complex Behavior of Lithium Metal Anodes through Operando Video Microscopy, ACS Cent. Sci. 2 (2016) 790–801. doi:10.1021/acscentsci.6b00260.

[28] K.-H. Chen, K.N. Wood, E. Kazyak, W.S. Lepage, A.L. Davis, A.J. Sanchez, N.P. Dasgupta, Dead lithium: mass transport effects on voltage, capacity, and failure of lithium metal anodes, J. Mater. Chem. A. 5 (2017) 11671–11681. doi:10.1039/c7ta00371d.

[29] P. Bai, J. Li, F.R. Brushett, M.Z. Bazant, Transition of lithium growth mechanisms in liquid electrolytes, Energy Environ. Sci. Energy Environ. Sci. 9 (2016) 3221–3229. doi:10.1039/c6ee01674j.

[30] M. Dollé, L. Sannier, B. Beaudoin, M. Trentin, J.M. Tarascon, Live scanning electron microscope observations of dendritic growth in lithium/polymer cells, Electrochem. Solid-State Lett. 5 (2002) A286–A289. doi:10.1149/1.1519970.

[31] Y.S. Cohen, Y. Cohen, D. Aurbach, Micromorphological Studies of Lithium Electrodes in Alkyl Carbonate Solutions Using in Situ Atomic Force Microscopy, J. Phys. Chem. B. 104 (2000) 12282–12291. doi:10.1021/jp002526b.

[32] H. Ghassemi, M. Au, N. Chen, P.A. Heiden, R.S. Yassar, Real-time observation of lithium fibers growth inside a nanoscale lithium-ion battery, Appl. Phys. Lett. 99 (2011) 123113. doi:10.1063/1.3643035.

[33] Z. Zeng, W.I. Liang, H.G. Liao, H.L. Xin, Y.H. Chu, H. Zheng, Visualization of electrode-electrolyte interfaces in LiPF6/EC/DEC electrolyte for lithium ion batteries via in situ TEM, Nano Lett. 14 (2014) 1745–1750. doi:10.1021/nl403922u.

[34] F.M. Ross, Opportunities and challenges in liquid cell electron microscopy, Science (80-.). 350 (2015) aaa9886. doi:10.1126/science.aaa9886.

[35] A.J. Leenheer, K.L. Jungjohann, K.R. Zavadil, J.P. Sullivan, C.T. Harris, Lithium electrodeposition dynamics in aprotic electrolyte observed in situ via transmission electron Microscopy, ACS Nano. 9 (2015) 4379–4389. doi:10.1021/acsnano.5b00876.

[36] X.H. Liu, Y. Liu, A. Kushima, S. Zhang, T. Zhu, J. Li, J.Y. Huang, In situ TEM experiments of electrochemical lithiation and delithiation of individual nanostructures, Adv. Energy Mater. 2 (2012) 722–741. doi:10.1002/aenm.201200024.

[37] A. Kushima, K.P. So, C. Su, P. Bai, N. Kuriyama, T. Maebashi, Y. Fujiwara, M.Z. Bazant, J. Li, Liquid cell transmission electron microscopy observation of lithium metal growth and dissolution: Root growth, dead lithium and lithium flotsams, Nano Energy. 32 (2017) 271–279. doi:10.1016/j.nanoen.2016.12.001.

[38] K.J. Harry, D.T. Hallinan, D.Y. Parkinson, A.A. Macdowell, N.P. Balsara, Detection of subsurface structures underneath dendrites formed on cycled lithium metal electrodes, Nat. Mater. 13 (2013). doi:10.1038/NMAT3793.

[39] C.S. David Eastwood, P.R. Shearing, P.D. Lee, D.S. Eastwood, ab M. Paul Bayley, H. Jung Chang, O.O. Taiwo, J. Vila-Comamala, D.J. L Brett, C. Rau, afg J. Philip Withers, ab R. Paul Shearing, C.P. Grey cd, Three-dimensional characterization of electrodeposited lithium microstructures using synchrotron X-ray phase contrast imaging, Chem. Commun. 51 (2015) 239–436. doi:10.1039/c4cc03187c.

[40] S. Chandrashekar, N.M. Trease, H.J. Chang, L.-S. Du, C.P. Grey, A. Jerschow, 7Li MRI of Li batteries reveals location of microstructural lithium, Nat. Mater. 11 (2012). doi:10.1038/NMAT3246.

[41] E. Peled, S. Menkin, Review-SEI: Past, Present and Future, J. Electrochem. Soc. 164 (2017) 1703–1719. doi:10.1149/2.1441707jes.

[42] J. Zheng, J.A. Lochala, A. Kwok, Z.D. Deng, J. Xiao, Research Progress towards Understanding the Unique Interfaces between Concentrated Electrolytes and Electrodes for Energy Storage Applications, Adv. Sci. 4 (2017) 1–19. doi:10.1002/advs.201700032.

[43] C. Xu, B. Sun, T. Gustafsson, K. Edström, D. Brandell, M. Hahlin, Interface layer formation in solid polymer electrolyte lithium batteries: an XPS study, J. Mater. Chem. A. 2 (2014) 7256–7264. doi:10.1039/C4TA00214H.

[44] E. Peled, D. Golodnitsky, G. Ardel, Advanced model for solid electrolyte interphase electrodes in liquid and polymer electrolytes, J. Electrochem. Soc. 144 (1997). doi:10.1149/1.1837858.

[45] H.J. Chang, N.M. Trease, A.J. Ilott, D. Zeng, L.S. Du, A. Jerschow, C.P. Grey, Investigating Li Microstructure Formation on Li Anodes for Lithium Batteries by in Situ 6Li/7Li NMR and SEM, J. Phys. Chem. C. 119 (2015) 16443–16451. doi:10.1021/acs.jpcc.5b03396.

[46] R. Bhattacharyya, B. Key, H. Chen, A.S. Best, A.F. Hollenkamp, C.P. Grey, In situ NMR observation of the formation of metallic lithium microstructures in lithium batteries, Nat. Mater. 9 (2010). doi:10.1038/NMAT2764.

[47] C. Wan, S. Xu, M.Y. Hu, R. Cao, J. Qian, Z. Qin, J. Liu, K.T. Mueller, J.G. Zhang, J.Z. Hu, Multinuclear NMR Study of the Solid Electrolyte Interface Formed in Lithium Metal Batteries, ACS Appl. Mater. Interfaces. 9 (2017) 14741–14748. doi:10.1021/acsami.6b15383.

[48] S. Li, M. Jiang, Y. Xie, H. Xu, J. Jia, J. Li, Developing high-performance lithium metal

anode in liquid electrolytes: challenges and progress, Adv. Mater. 30 (2018) 1706375. doi:10.1002/adma.201706375.

[49] J. Steiger, D. Kramer, R. Mönig, Microscopic observations of the formation, growth and shrinkage of lithium moss during electrodeposition and dissolution, Electrochim. Acta. 136 (2014) 529–536. doi:10.1016/j.electacta.2014.05.120.

[50] J.B. Goodenough, Y. Kim, Challenges for Rechargeable Li Batteries, Chem. Mater. 22 (2010) 587. doi:10.1021/cm901452z.

[51] J.-M. Tarascon, M. Armand, Issues and challenges facing rechargeable lithium batteries, Nature. 414 (2001) 359–367. doi:10.1038/35104644.

[52] H. Yu, H. Zhou, High-Energy Cathode Materials (Li2MnO3-LiMO2) for Lithium-Ion Batteries, J Phys Chem Lett. 4 (2013) 1268–1280. doi:10.1021/jz400032v.

[53] G. Assat, J.M. Tarascon, Fundamental understanding and practical challenges of anionic redox activity in Li-ion batteries, Nat. Energy. 3 (2018) 373–386. doi:10.1038/s41560-018-0097-0.

[54] K. Luo, M.R. Roberts, N. Niccológuerrini, N. Tapia-Ruiz, R. Hao, F. Massel, D.M. Pickup, S. Ramos, Y.-S. Liu, J. Guo, A. V Chadwick, L.C. Duda, P.G. Bruce, Anion Redox Chemistry in the Cobalt Free 3d Transition Metal Oxide Intercalation Electrode Li[Li 0.2 Ni 0.2 Mn 0.6]O 2 Oxidation of O 2− on charging is associated with the generation, J. Am. Chem. Soc. 138 (2016) 11211–11218. doi:10.1021/jacs.6b05111.

[55] M. Sathiya, G. Rousse, K. Ramesha, C.P. Laisa, H. Vezin, M.T. Sougrati, M.-L. Doublet, D. Foix, D. Gonbeau, W. Walker, A.S. Prakash, M. Ben Hassine, L. Dupont, J.-M. Tarascon, Reversible anionic redox chemistry in high-capacity layered-oxide electrodes, Nat. Mater. 12 (2013). doi:10.1038/NMAT3699.

[56] C.R. Fell, D. Qian, K.J. Carroll, M. Chi, J.L. Jones, Y.S. Meng, Correlation between oxygen vacancy, microstrain, and cation distribution in lithium-excess layered oxides during the first electrochemical cycle, Chem. Mater. 25 (2013) 1621–1629. doi:10.1021/cm4000119.

[57] B. Xu, C.R. Fell, M. Chi, Y.S. Meng, Identifying surface structural changes in layered Li-excess nickel manganese oxides in high voltage lithium ion batteries: A joint experimental and theoretical study, Energy Environ. Sci. 4 (2011) 2223–2233. doi:10.1039/c1ee01131f.

[58] K. Luo, M.R. Roberts, R. Hao, N. Guerrini, D.M. Pickup, Y.-S. Liu, K. Edström, J. Guo, A. V Chadwick, L.C. Duda, P.G. Bruce, Charge-compensation in 3*d*-transition-metal-oxide intercalation cathodes through the generation of localized electron holes on oxygen, Nat. Chem. |. 8 (2016). doi:10.1038/NCHEM.2471.

[59] A.R. Armstrong, A.R. Armstrong, M. Holzapfel, M. Holzapfel, S.H. Kang, P. Nova, P. Nova, S.-H. Kang, M.M. Thackeray, M.M. Thackeray, P.G. Bruce, P.G. Bruce, A. Robert Armstrong, Michael Holzapfel, Petr Novak, Christopher S. Johnson, Sun-Ho Kang, Michael M. Thackeray, and Peter G. Bruce, J. Am. Chem. Soc. 128 (2006) 8694–8698.

doi:10.1021/ja062027.

[60] D. Qian, B. Xu, M. Chi, Y.S. Meng, Uncovering the roles of oxygen vacancies in cation migration in lithium excess layered oxides., Phys. Chem. Chem. Phys. 16 (2014) 14665–8. doi:10.1039/c4cp01799d.

[61] B. Qiu, M. Zhang, L. Wu, J. Wang, Y. Xia, D. Qian, H. Liu, S. Hy, Y. Chen, K. An, Y. Zhu, Z. Liu, Y.S. Meng, Gas–solid interfacial modification of oxygen activity in layered oxide cathodes for lithium-ion batteries, Nat. Commun. 7 (2016) 12108. doi:10.1038/ncomms12108.

[62] H. Liu, J. Huang, D. Qian, S. Hy, C. Fang, J. Luo, Y.S. Meng, Communication—Enhancing the Electrochemical Performance of Lithium-Excess Layered Oxide Li 1.13 Ni 0.3 Mn 0.57 O 2 via a Facile Nanoscale Surface Modification, J. Electrochem. Soc. 163 (2016) A971–A973. doi:10.1149/2.0821606jes.

[63] G.R. Li, X. Feng, Y. Ding, S.H. Ye, X.P. Gao, AlF3-coated Li(Li0.17Ni0.25Mn0.58)O2 as cathode material for Li-ion batteries, Electrochi. (2012) 308–315.

[64] S. Hy, H. Liu, D. Qian, M. Zhang, B.J. Hwang, Y.S. Meng, Performance and Design Considerations For The lithium Excess Layered Oxide Positive Electrode Materials For Lithium Ion Batteries, Energy Environ. Sci. 9 (2016) 1931. doi:10.1039/C5EE03573B.

[65] Z.Q. Deng, A. Manthiram, Influence of cationic substitutions on the oxygen loss and reversible capacity of lithium-rich layered oxide cathodes, J. Phys. Chem. C. 115 (2011) 7097–7103. doi:10.1021/jp200375d.

[66] C.-C. Wang, A. Manthiram, Influence of cationic substitutions on the first charge and reversible capacities of lithium-rich layered oxide cathodes, J. Mater. Chem. A. 1 (2013) 10209–10217. doi:10.1039/c3ta11703k.

[67] D.H. Seo, J. Lee, A. Urban, R. Malik, S. Kang, G. Ceder, The structural and chemical origin of the oxygen redox activity in layered and cation-disordered Li-excess cathode materials, Nat. Chem. 8 (2016) 692–697. doi:10.1038/nchem.2524.

[68] C.C. Wang, A. Manthiram, Influence of cationic substitutions on the first charge and reversible capacities of lithium-rich layered oxide cathodes, J. Mater. Chem. A. 1 (2013) 10209–10217. doi:10.1039/c3ta11703k.

[69] P. Xiao, Z.Q. Deng, A. Manthiram, G. Henkelman, Calculations of oxygen stability in lithium-rich layered cathodes, J. Phys. Chem. C. 116 (2012) 23201–23204. doi:10.1021/jp3058788.

[70] Y. Gao, X. Wang, J. Ma, Z. Wang, L. Chen, Selecting substituent elements for Li-rich Mn-based cathode materials by Density Functional Theory (DFT) calculations, Chem. Mater. 27 (2015) 3456–3461. doi:10.1021/acs.chemmater.5b00875.

[71] F. Kong, R.C. Longo, M.-S. Park, J. Yoon, D.-H. Yeon, J.-H. Park, W.-H. Wang, S. Kc, S.-

G. Doo, K. Cho, Ab initio study of doping effects on LiMnO2 and Li2MnO3 cathode materials for Li-ion batteries, J. Mater. Chem. A. 3 (2015) 8489–8500. doi:10.1039/C5TA01445J.

[72] Y. Gao, J. Ma, X. Wang, X. Lu, Y. Bai, Z. Wang, L. Chen, Improved electron/Li-ion transport and oxygen stability of Mo-doped Li2MnO3, J. Mater. Chem. A. 2 (2014) 4811. doi:10.1039/c3ta15236g.

[73] J. Li, C. Zhan, J. Lu, Y. Yuan, R. Shahbazian-Yassar, X. Qiu, K. Amine, Improve First-Cycle Efficiency and Rate Performance of Layered-Layered Li $_{1.2}$ Mn $_{0.6}$ Ni $_{0.2}$ O $_{2}$ Using Oxygen Stabilizing Dopant, ACS Appl. Mater. Interfaces. 7 (2015) 16040–16045. doi:10.1021/acsami.5b04343.

[74] J. Liu, S. Wang, Z. Ding, R. Zhou, Q. Xia, J. Zhang, L. Chen, W. Wei, P. Wang, The Effect of Boron Doping on Structure and Electrochemical Performance of Lithium-Rich Layered Oxide Materials, ACS Appl. Mater. Interfaces. 8 (2016) 18008–18017. doi:10.1021/acsami.6b03056.

[75] A.I. Liechtenstein, V.I. Anisimov, J. Zaanen, Density-functional theory and strong interactions: Orbital ordering in Mott-Hubbard insulators, Phys. Rev. B. 52 (1995). doi:10.1103/PhysRevB.52.R5467.

[76] H. Liu, D. Qian, M.G. Verde, M. Zhang, L. Baggetto, K. An, Y. Chen, K.J. Carroll, D. Lau, M. Chi, G.M. Veith, Y.S. Meng, Understanding the Role of NH4F and Al2O3 Surface Co-modification on Lithium-Excess Layered Oxide Li1.2Ni0.2Mn0.6O2, ACS Appl. Mater. Interfaces. 7 (2015) 19189–19200. doi:10.1021/acsami.5b04932.

[77] L. Wang, T. Maxisch, G. Ceder, Oxidation energies of transition metal oxides within the GGA+ U framework, Phys. Rev. B. 73 (2006) 195107. doi:10.1103/PhysRevB.73.195107.

[78] E. McCalla, A.M. Abakumov, M. Saubanère, D. Foix, E.J. Berg, G. Rousse, M.-L. Doublet, D. Gonbeau, P. Novák, G. Van Tendeloo, R. Dominko, J.-M. Tarascon, Visualization of O-O peroxo-like dimers in high-capacity layered oxides for Li-ion batteries., Science. 350 (2015) 1516–21. doi:10.1126/science.aac8260.

[79] D.-H. Seo, J. Lee, A. Urban, R. Malik, S. Kang, G. Ceder, The structural and chemical origin of the oxygen redox activity in layered and cation-disordered Li-excess cathode materials, Nat. Chem. 8 (2016) 692–697. doi:10.1038/NCHEM.2524.

[80] M. Saubanere, E. McCalla, J.-M. Tarascon, M.-L. Doublet, The intriguing question of anionic redox in high-energy density cathodes for Li-ion batteries, Energy Environ. Sci. (2016) 984–991. doi:10.1039/C5EE03048J.

[81] M. Sathiya, G. Rousse, K. Ramesha, C.P. Laisa, H. Vezin, M.T. Sougrati, M.-L. Doublet, D. Foix, D. Gonbeau, W. Walker, a S. Prakash, M. Ben Hassine, L. Dupont, J.-M. Tarascon, Reversible anionic redox chemistry in high-capacity layered-oxide electrodes., Nat. Mater. 12 (2013). doi:10.1038/nmat3699.

[82] Y. Zang, C.-X. Ding, X.-C. Wang, Z.-Y. Wen, C.-H. Chen, Molybdenum-doped lithium-rich layered-structured cathode material Li1.2Ni0.2Mn0.6O2 with high specific capacity and improved rate performance, Electrochim. Acta. 168 (2015) 234–239. doi:10.1016/j.electacta.2015.03.223.

[83] X. Deng, S.Y. Quek, M.M. Biener, J. Biener, D.H. Kang, R. Schalek, E. Kaxiras, C.M. Firend, Selective Thermal Reduction of nanostructures on Au (111), Surf. Sci. 602 (2007) 1166–1174. https://e-reports-ext.llnl.gov/pdf/355774.pdf (accessed April 6, 2017).

[84] S. Verdier, L. El Ouatani, R. Dedryvère, F. Bonhomme, P. Biensan, D. Gonbeau, XPS Study on Al2O3- and AlPO4-Coated LiCoO2 Cathode Material for High-Capacity Li Ion Batteries, J. Electrochem. Soc. 154 (2007) A1088. doi:10.1149/1.2789299.

[85] J. Ma, Y.-N. Zhou, Y. Gao, Q. Kong, Z. Wang, X.-Q. Yang, L. Chen, Molybdenum Substitution for Improving the Charge Compensation and Activity of Li_2 MnO_3, Chem. - A Eur. J. 20 (2014) 8723–8730. doi:10.1002/chem.201402727.

[86] M. Iftekhar, N.E. Drewett, A.R. Armstrong, D. Hesp, F. Braga, S. Ahmed, L.J. Hardwick, Characterization of Aluminum Doped Lithium-Manganese Rich Composites for Higher Rate Lithium-Ion Cathodes, J. Electrochem. Soc. 161 (2014) A2109–A2116. doi:10.1149/2.0441414jes.

[87] P.K. Nayak, J. Grinblat, M. Levi, E. Levi, S. Kim, J.W. Choi, D. Aurbach, Al Doping for Mitigating the Capacity Fading and Voltage Decay of Layered Li and Mn-Rich Cathodes for Li-Ion Batteries, Adv. Energy Mater. 6 (2016) 1502398. doi:10.1002/aenm.201502398.

[88] M.B. Kanoun, S. Goumri-Said, U. Schwingenschlogl, A. Manchon, Magnetism in Sc-doped ZnO with zinc vacancies: A hybrid density functional and GGA+U approaches, Chem. Phys. Lett. 532 (2012) 96–99. doi:10.1016/j.cplett.2012.02.055.

[89] B.J. Morgan, G.W. Watson, A DFT+U description of oxygen vacancies at the TiO2 rutile (110) surface, Surf. Sci. 601 (2007) 5034–5041. doi:10.1016/j.susc.2007.08.025.

[90] D.O. Scanlon, A. Walsh, B.J. Morgan, G.W. Watson, An ab initio Study of Reduction of V2O5 through the Formation of Oxygen Vacancies and Li Intercalation, J. Phys. Chem. C. 112 (2008) 9903–9911. doi:10.1021/jp711334f.

[91] Y. Hinuma, Y.S. Meng, K. Kang, G. Ceder, Phase Transitions in the LiNi0.5Mn0.5O2 System with Temperature, Chem. Mater. 19 (2007) 1790–1800. doi:10.1021/cm062903i.

[92] V.L. Chevrier, S.P. Ong, R. Armiento, M.K.Y. Chan, G. Ceder, Hybrid density functional calculations of redox potentials and formation energies of transition metal compounds, Phys. Rev. B. 82 (2010) 075122. doi:10.1103/PhysRevB.82.075122.

[93] J. Feng, S. Shian, B. Xiao, D.R. Clarke, First-principles calculations of the high-temperature phase transformation in yttrium tantalate, Phys. Rev. B. 90 (2014) 1–13. doi:10.1103/PhysRevB.90.094102.

[94] G.Y. Huang, C.Y. Wang, J.T. Wang, Detailed check of the LDA+U and GGA+U corrected method for defect calculations in wurtzite ZnO, Comput. Phys. Commun. 183 (2012) 1749–1752. doi:10.1016/j.cpc.2012.03.017.

[95] H. Kamisaka, T. Hitosugi, K. Yamashita, First-principle calculations of dopant-oxygen vacancy complexes in transparent conducting TiO2 systems., Hyomen Kagaku. 31 (2010) 343–351. doi:10.1380/jsssj.31.343.

[96] M. Khan, J.N. Xu, N. Chen, W.B. Cao, Electronic and optical properties of pure and Mo doped anatase TiO2 using GGA and GGA plus U calculations, Phys. B-Condensed Matter. 407 (2012) 3610–3616. doi:10.1016/j.physb.2012.05.037.

[97] P.-A. Lin, H.-T. Jeng, C.-S. Hsue, Electronic structure and orbital ordering of SrRu1−xTixO3: GGA+U Investigations, Phys. Rev. B. 77 (2008) 085118. doi:10.1103/PhysRevB.77.085118.

[98] W. Tang, E. Sanville, G. Henkelman, A grid-based Bader analysis algorithm without lattice bias, J. Phys. Condens. Matter. 21 (2009) 84204–7. doi:10.1088/0953-8984/21/8/084204.

[99] I. Yoshimatsu, T. Hirai, J. Yamaki, Lithium electrode morphology during cycling in lithium cells, 1988. doi:10.1149/1.2095351.

[100] D. Lu, Y. Shao, T. Lozano, W.D. Bennett, G.L. Graff, B. Polzin, J. Zhang, M.H. Engelhard, N.T. Saenz, W.A. Henderson, P. Bhattacharya, J. Liu, J. Xiao, Failure mechanism for fast-charged lithium metal batteries with liquid electrolytes, Adv. Energy Mater. 5 (2015) 1400993. doi:10.1002/aenm.201400993.

[101] B.L. Mehdi, J. Qian, E. Nasybulin, C. Park, D.A. Welch, ∥ R Faller, ∥ H Mehta, W.A. Henderson, W. Xu, C.M. Wang, J.E. Evans, ⊥ J Liu, J.-G. Zhang, K.T. Mueller, N.D. Browning, Observation and quantification of nanoscale processes in lithium batteries by operando electrochemical (S)TEM, Nano Lett. 15 (2015) 2168–2173. doi:10.1021/acs.nanolett.5b00175.

[102] C. Xu, B. Sun, T. Orn Gustafsson, K. Edst, D. Brandell, M. Hahlin, Interface layer formation in solid polymer electrolyte lithium batteries: an XPS study, J. Mater. Chem. A. 2 (2014) 7256–7264. doi:10.1039/c4ta00214h.

[103] X.B. Cheng, R. Zhang, C.Z. Zhao, F. Wei, J.G. Zhang, Q. Zhang, A review of solid electrolyte interphases on lithium metal anode, Adv. Sci. 3 (2015) 1–20. doi:10.1002/advs.201500213.

[104] D. Aurbach, I. Weissman, On the possibility of LiH formation on Li surfaces in wet electrolyte solutions, Electrochem. Commun. 1 (1999) 324–331. doi:10.1016/S1388-2481(99)00064-8.

[105] Y.Y. Hu, Z. Liu, K.W. Nam, O.J. Borkiewicz, J. Cheng, X. Hua, M.T. Dunstan, X. Yu, K.M. Wiaderek, L.S. Du, K.W. Chapman, P.J. Chupas, X.Q. Yang, C.P. Grey, Origin of additional capacities in metal oxide lithium-ion battery electrodes, Nat. Mater. 12 (2013)

1130–1136. doi:10.1038/nmat3784.

[106] S.M. Wood, C. Fang, E.J. Dufek, S.C. Nagpure, S. V. Sazhin, B. Liaw, Y.S. Meng, Predicting Calendar Aging in Lithium Metal Secondary Batteries: The Impacts of Solid Electrolyte Interphase Composition and Stability, Adv. Energy Mater. 8 (2018) 1–6. doi:10.1002/aenm.201801427.

[107] A. Drenik, D. Alegre, S. Brezinsek, A. De Castro, U. Kruezi, M. Oberkofler, M. Panjan, G. Primc, T. Reichbauer, M. Resnik, V. Rohde, M. Seibt, P.A. Schneider, T. Wauters, R. Zaplotnik, the A.-U. and Euro.M. teams, J. contributors, Evaluation of the plasma hydrogen isotope content by residual gas analysis at JET and AUG, Phys. Scr. T170 (2017) 014021. doi:10.1088/1402-4896/aa878b.

[108] K. Xu, Nonaqueous Liquid Electrolytes for Lithium-Based Rechargeable Batteries, Chem. Rev. 104 (2004) 4303–4417. doi:10.1021/cr030203g.

[109] W. Xu, J. Wang, F. Ding, X. Chen, E. Nasybulin, Y. Zhang, J.-G. Zhang, Lithium metal anodes for rechargeable batteries, Energy Environ. Sci. 7 (2014) 513–537. doi:10.1039/C3EE40795K.

[110] J. Zheng, P. Yan, D.H. Mei, M.H. Engelhard, S.S. Cartmell, B.J. Polzin, C.M. Wang, J.G. Zhang, W. Xu, Highly stable operation of lithium metal batteries enabled by the formation of a transient high-concentration electrolyte layer, Adv. Energy Mater. 6 (2016) 1–10. doi:10.1002/aenm.201502151.

[111] J. Alvarado, M.A. Schroeder, M. Zhang, O. Borodin, E. Gobrogge, M. Olguin, M.S. Ding, M. Gobet, S. Greenbaum, Y.S. Meng, K. Xu, A carbonate-free, sulfone-based electrolyte for high-voltage Li-ion batteries, Mater. Today. 21 (2018) 341–353. doi:10.1016/j.mattod.2018.02.005.

[112] F. Ding, W. Xu, G.L. Graff, J. Zhang, M.L. Sushko, X. Chen, Y. Shao, M.H. Engelhard, Z. Nie, J. Xiao, X. Liu, P. V Sushko, J. Liu, J.-G. Zhang, Dendrite-free lithium deposition via self-healing electrostatic shield mechanism, J. Am. Chem. Soc. 135 (2013) 43. doi:10.1021/ja312241y.

[113] N.W. Li, Y.X. Yin, C.P. Yang, Y.G. Guo, An artificial solid electrolyte interphase layer for stable lithium metal anodes, Adv. Mater. 28 (2016) 1853–1858. doi:10.1002/adma.201504526.

[114] H. Liu, X. Yue, X. Xing, Q. Yan, J. Huang, V. Petrova, H. Zhou, P. Liu, A scalable 3D lithium metal anode, Energy Storage Mater. 16 (2019) 505–511. doi:10.1016/j.ensm.2018.09.021.

[115] J. Alvarado, M.A. Schroeder, T.P. Pollard, X. Wang, J.Z. Lee, M. Zhang, T. Wynn, M. Ding, O. Borodin, Y.S. Meng, K. Xu, Bisalt ether electrolytes: A pathway towards lithium metal batteries with Ni-rich cathodes, Energy Environ. Sci. 12 (2019) 780–794. doi:10.1039/c8ee02601g.

[116] B.D. Adams, J. Zheng, X. Ren, W. Xu, J.G. Zhang, Accurate Determination of Coulombic Efficiency for Lithium Metal Anodes and Lithium Metal Batteries, Adv. Energy Mater. 1702097 (2017) 1–11. doi:10.1002/aenm.201702097.

[117] H. Lee, X. Ren, C. Niu, L. Yu, M.H. Engelhard, I. Cho, M.H. Ryou, H.S. Jin, H.T. Kim, J. Liu, W. Xu, J.G. Zhang, Suppressing lithium dendrite growth by metallic coating on a separator, Adv. Funct. Mater. 27 (2017) 1704391. doi:10.1002/adfm.201704391.

[118] J. Saint, M. Morcrette, D. Larcher, J.M. Tarascon, Exploring the Li-Ga room temperature phase diagram and the electrochemical performances of the LixGay alloys vs. Li, Solid State Ionics. 176 (2005) 189–197. doi:10.1016/j.ssi.2004.05.021.

[119] X. Yin, W. Tang, I.D. Jung, K.C. Phua, S. Adams, S.W. Lee, G.W. Zheng, Insights into morphological evolution and cycling behaviour of lithium metal anode under mechanical pressure, Nano Energy. 50 (2018) 659–664. doi:10.1016/j.nanoen.2018.06.003.

[120] H. Lee, S. Chen, X. Ren, A. Martinez, V. Shutthanandan, M. Vijayakumar, K.S. Han, Q. Li, J. Liu, W. Xu, J.G. Zhang, Electrode Edge Effects and the Failure Mechanism of Lithium-Metal Batteries, ChemSusChem. 11 (2018) 3821–3828. doi:10.1002/cssc.201801445.

[121] T. Nishida, K. Nishikawa, M. Rosso, Y. Fukunaka, Optical observation of Li dendrite growth in ionic liquid, Electrochim. Acta. 100 (2013) 333–341. doi:10.1016/j.electacta.2012.12.131.

[122] K. Nishikawa, T. Mori, T. Nishida, Y. Fukunaka, M. Rosso, T. Homma, In Situ Observation of Dendrite Growth of Electrodeposited Li Metal, J. Electrochem. Soc. 157 (2010) A1212. doi:10.1149/1.3486468.

[123] X.-B. Cheng, C.-Z. Zhao, Y.-X. Yao, H. Liu, Q. Zhang, Recent Advances in Energy Chemistry between Solid-State Electrolyte and Safe Lithium-Metal Anodes, Chem. 5 (2019) 74–96. doi:10.1016/J.CHEMPR.2018.12.002.

[124] S.C. Nagpure, T.R. Tanim, E.J. Dufek, V. V. Viswanathan, A.J. Crawford, S.M. Wood, J. Xiao, C.C. Dickerson, B. Liaw, Impacts of lean electrolyte on cycle life for rechargeable Li metal batteries, J. Power Sources. 407 (2018) 53–62. doi:10.1016/j.jpowsour.2018.10.060.

[125] M. Arakawa, S.-I. Tobishima, Y. Nemoto, M. Ichimura, J.-I. Yamaki, Lithium electrode cycleability and morphology dependence on current density, J. Power Sources. 43 (1993) 27–35. doi:10.1016/0378-7753(93)80099-B.

[126] A. Aryanfar, D.J. Brooks, A.J. Colussi, M.R. Hoffmann, Quantifying the dependence of dead lithium losses on the cycling period in lithium metal batteries, Phys. Chem. Chem. Phys. Phys. Chem. Chem. Phys. 16 (2014) 24965–24970. doi:10.1039/c4cp03590a.

[127] A.J. Schoenfeld, E.J. Carragee, Clearing the cervical spine in Plato’s cave, Spine J. 14 (2014) 2554–2556. doi:10.1016/j.spinee.2014.08.005.

[128] K. Xu, Electrolytes and interphases in Li-ion batteries and beyond, Chem. Rev. 114 (2014)

11503–11618. doi:10.1021/cr500003w.

[129] L. Suo, Y.-S. Hu, H. Li, M. Armand, L. Chen, A new class of Solvent-in-Salt electrolyte for high-energy rechargeable metallic lithium batteries, Nat. Commun. 4 (2013). doi:10.1038/ncomms2513.

[130] Q. Li, S. Zhu, Y. Lu, 3D Porous Cu Current Collector/Li-Metal Composite Anode for Stable Lithium-Metal Batteries, Adv. Funct. Mater. 27 (2017) 1606422. doi:10.1002/adfm.201606422.

[131] K. Fu, Y. Gong, J. Dai, A. Gong, X. Han, Y. Yao, C. Wang, Y. Wang, Y. Chen, C. Yan, Y. Li, E.D. Wachsman, L. Hu, Flexible, solid-state, ion-conducting membrane with 3D garnet nanofiber networks for lithium batteries, Proc. Natl. Acad. Sci. U. S. A. 113 (2016) 7094–7099. doi:10.1073/pnas.1600422113.

[132] M. Chi, L. Shi, Z. Wang, J. Zhu, X. Mao, Y. Zhao, M. Zhang, L. Sun, S. Yuan, Excellent rate capability and cycle life of Li metal batteries with ZrO 2 /POSS multilayer-assembled PE separators, Nano Energy. 28 (2016) 1–11. doi:10.1016/j.nanoen.2016.07.037.

[133] M.H. Ryou, Y.M. Lee, J.K. Park, J.W. Choi, Mussel-inspired polydopamine-treated polyethylene separators for high-power li-ion batteries, Adv Mater. 23 (2011) 3066–3070. doi:10.1002/adma.201100303.

[134] G. Zheng, S.W. Lee, Z. Liang, H.W. Lee, K. Yan, H. Yao, H. Wang, W. Li, S. Chu, Y. Cui, Interconnected hollow carbon nanospheres for stable lithium metal anodes, Nat. Nanotechnol. 9 (2014) 618–623. doi:10.1038/nnano.2014.152.

[135] M. Nisula, M. Karppinen, Atomic/Molecular Layer Deposition of Lithium Terephthalate Thin Films as High Rate Capability Li-Ion Battery Anodes, Nano Lett. 16 (2016) 31. doi:10.1021/acs.nanolett.5b04604.

[136] A.C. Kozen, C.F. Lin, A.J. Pearse, M.A. Schroeder, X. Han, L. Hu, S.B. Lee, G.W. Rubloff, M. Noked, Next-Generation Lithium Metal Anode Engineering via Atomic Layer Deposition, ACS Nano. 9 (2015) 5884–5892. doi:10.1021/acsnano.5b02166.

[137] L. Chen, J.G. Connell, A. Nie, Z. Huang, K.R. Zavadil, K.C. Klavetter, Y. Yuan, S. Sharifi-Asl, R. Shahbazian-Yassar, J.A. Libera, A.U. Mane, J.W. Elam, Lithium metal protected by atomic layer deposition metal oxide for high performance anodes, J. Mater. Chem. A. 5 (2017) 12297–12309. doi:10.1039/c7ta03116e.